# SUPERCRITICAL ADSORPTION OF $CO_2$ AND $CH_4$ ON ILLITE-SMECTITE CLAY MINERALS UNDER SUBSURFACE CONDITIONS


Thesis presented by

Junyoung Hwang

submitted to the

Department of Chemical Engineering

Imperial College London


in fulfillment of the requirements

for the degree of

Doctor of Philosophy

under the supervision of

Dr. Ronny Pini

March 29, 2021

## Statement of originality

I declare that the work presented in the thesis, *Supercritical Adsorption of $CO_2$ and $CH_4$ on Illite-smectite Clay Minerals under Subsurface Conditions*, is my own conducted under the supervision of Dr. Ronny Pini at the Department of Chemical Engineering, Imperial College London, and all else is appropriately referenced. Statements are provided for any work that has been previously published or submitted for publication.

## Copyright declaration

The copyright of this thesis rests with the author. Unless otherwise indicated, its contents are licensed under a Creative Commons Attribution-Non Commercial 4.0 International Licence (CC BY-NC).

Under this licence, you may copy and redistribute the material in any medium or format. You may also create and distribute modified versions of the work. This is on the condition that: you credit the author and do not use it, or any derivative works, for a commercial purpose. When reusing or sharing this work, ensure you make the licence terms clear to others by naming the licence and linking to the licence text. Where a work has been adapted, you should indicate that the work has been changed and describe those changes.

Please seek permission from the copyright holder for uses of this work that are not included in this licence or permitted under UK Copyright Law.

# Abstract

Clay minerals are abundant in sedimentary formations and are dominated by nanoscale pores that provide a large surface area for physical interactions with surrounding reservoir fluids. Among them, adsorption has direct relevance to many geo-energy applications, including geological $CO_2$ storage and enhanced gas recovery, because the injected $CO_2$ and recoverable reservoir fluids largely exist in a dense adsorbed phase. In this regard, experimental sorption data of $CO_2$ and hydrocarbons on clay minerals under subsurface conditions allow us to estimate the storage capacity for $CO_2$ and the amount of natural gas recoverable from enhanced production. In this thesis, we present a combined experimental and modeling approach used to systematically investigate the sorption of supercritical $CO_2$ and $CH_4$ on three illite-smectite clay minerals (dry and hydrated) over a wide range of temperatures (25 °C to 115 °C) and pressures (up to 300 bar). The presented workflow includes comprehensive characterization of the nanoscale pores of the clay minerals using multiple methods, including gas and vapor sorption, that sheds light on the differences in sorption uptake of supercritical $CO_2$ and $CH_4$ that originate from clay-specific pore size distributions. An adsorption model based on the lattice density functional theory (LDFT) was adopted to quantify such observations through simple parametrization of the clay nanopores. In particular, the model results showed that saturation of supercritical fluids inside nanopores is fluid- and temperature-dependent and quantified the $CO_2/CH_4$ interaction energies with clay surfaces that agreed well with the adsorption metrics obtained from the experimental measurements. The ability of the LDFT model to incorporate the clay nanopores was further exploited to investigate sorption on smectite clay minerals that expand upon hydration. The results successfully demonstrated that enhanced sorption of $CO_2$ and $CH_4$ on hydrated smectite is due to the expansion of smectite interlayers that introduces additional micropore space.

## Acknowledgments

My first acknowledgment must go to Dr. Ronny Pini who has been truly supportive from the beginning to the end of my Ph.D. journey. I appreciate him for being patient with me and showing support at times when I showed sporadic interests that deviated from my main research project. I am thankful I had the opportunity to grow to be an independent researcher under his supervision.

I want to thank the Department of Chemical Engineering for the Departmental Ph.D. Scholarship, which allowed me to freely explore my research interests. I would also like to express my gratitude to Dr. Bradley Ladewig for his kind assistance in starting my Ph.D. program at Imperial College and for eventually becoming my academic mentor for the program.

I also want to thank (in order of meeting them) Takeshi, Lisa, Rebecca, Caroline, Humera, Ali, Emily, Swapna, Nerine, and Anna-Maria for being such amazing colleagues and better friends. The last four years spent in the office and in the lab were made easier with the coffee breaks in the common room and the chit-chats in the office I had with all of you. I truly hope there will be an opportunity for a reunion in the future.

My pursuit of education would not have been possible without the support and sacrifice of my family. I would like to especially thank my mom, whose No. 1 priority has been me throughout the last decade. For that, I am forever grateful.

Lastly, I want to thank Jessica J. Hong for being the rock I could always rely on. She has been the world's greatest pep talker and my best friend since the time of submitting my graduate school applications, which feels like only yesterday. It has been a lot of fun going from a couple of clueless college kids to sort of knowing what we are doing, and I cannot wait to see us grow some more in the future together.

# List of publications

- **J. Hwang**, L. Joss, R. Pini. Measuring and modelling supercritical adsorption of $CO_2$ and $CH_4$ on montmorillonite source clay, *Microporous and Mesoporous Materials* 273 (2019) 107-121.

- **J. Hwang** and R. Pini. Supercritical $CO_2$ and $CH_4$ Uptake by Illite-Smectite Clay Minerals, *Environmental Science and Technology* 53 (2019) 11588-11596.

- H. Ansari, L. Joss, **J. Hwang**, J. P. M. Trusler, G. Maitland, R. Pini. Supercritical adsorption in micro-and meso-porous carbons and its utilisation for textural characterisation, *Microporous and Mesoporous Materials* 308 (2020).

- H. G. T. Nguyen, C. M. Sims, B. Toman, J. Horn, R. D. van Zee, M. Thommes, R. Ahmad, J. F. M. Denayer, G. V. Baron, E. Napolitano, M. Bielewski, E. Mangano, S. Brandani, D. P. Broom, M. J. Benham, A. Dailly, F. Dresibach, S. Edubilli, S. Gumma, J. Möllmer, M. Lange, M. Tian, T. J. Mays, T. Shigeoka, S. Yamakita, M. Hakuman, Y. Nakada, K. Nakai, **J. Hwang**, R. Pini, H. Jiang, A. D. Ebner, M. A. Nicholson, J. A. Ritter, J. Farrando-Pérez, C. Cuadrado-Collados, J. Silvestre-Albero, C. Tampaxis, T. Steriotis, S. D. Řimnáčová, M. Švábová, M. Vorokhta, H. Wang, E. Bovens, N. Heymans, G. De Weireld. A reference high-pressure $CH_4$ adsorption isotherm for Zeolite Y: results of an interlaboratory study, *Adsorption* 26 (2020), 1253-1266.

- Q. C. Wenning, C. Madonna, T. Kurotori, C. Petrini, **J. Hwang**, A. Zappone, S. Wiemer, D. Giardini, R. Pini. Chemo-mechanical coupling in fractured shale with water and hydrocarbon flow, *Geophysical Research Letters* 48 (2021).

- R. Pini, H. Ansari, **J. Hwang**. Measurement and interpretation of unary supercritical gas adsorption isotherms in micro-mesoporous solids, *Adsorption* (2021).

- **J. Hwang** and R. Pini. Enhanced Sorption of Supercritical $CO_2$ and $CH_4$ in the Hydrated Interlayer Pores of Smectite, *Langmuir* (2021).

# Table of Contents

**1 Introduction** **23**

1.1 Thesis structure . . . . . 25

**2 Background and literature review** **27**

2.1 Introduction . . . . . 27

2.2 Clay minerals . . . . . 27

2.2.1 Smectite . . . . . 29

2.2.2 Illite . . . . . 31

2.2.3 Illite-smectite mixed layer . . . . . 31

2.3 Adsorption phenomena . . . . . 31

2.3.1 Adsorption isotherms: absolute, excess, and net . . . . . 33

2.3.2 Adsorption on clay minerals . . . . . 36

**3 Experimental apparatus** **41**

3.1 Introduction . . . . . 41

3.2 Experimental setup . . . . . 41

3.2.1 MSB operating principles . . . . . 43

3.2.2 Helium gravimetry . . . . . 45

3.2.3 Data logging . . . . . 46

3.3 NIST interlaboratory study . . . . . 46

3.3.1 Interlaboratory comparison . . . . . 47

3.4 Concluding remarks . . . . . 50

**4 Adsorption model: lattice density functional theory 53**

4.1 Introduction . . . . . 53

4.2 Model equations . . . . . 54

4.2.1 Translation to physical units . . . . . 58

4.2.2 Parameter determination . . . . . 59

4.3 Reduction to conventional adsorption models . . . . . 61

4.4 Solution procedure . . . . . 61

4.5 Concluding remarks . . . . . 62

**5 Workflow development: Na-rich montmorillonite 65**

5.1 Introduction . . . . . 65

5.2 Materials . . . . . 66

5.3 Experimental methods . . . . . 66

5.3.1 Low-pressure gas physisorption . . . . . 66

5.3.2 High-pressure sorption experiments . . . . . 67

5.4 Modeling . . . . . 67

5.4.1 DR equation for micropore volume . . . . . 67

5.4.2 Application of BJH theory to slit pores . . . . . 68

5.4.3 Henry constant and enthalpy of adsorption . . . . . 69

5.5 Results . . . . . 70

5.5.1 $N_2$ physisorption isotherm . . . . . 70

5.5.2 Skeletal volume . . . . . 73

5.5.3 Supercritical adsorption of $CO_2$ and $CH_4$: experiments . . . . . 75

5.5.4 Supercritical adsorption of $CO_2$ and $CH_4$: modeling . . . . . 77

5.5.5 Henry constants and isosteric heat . . . . . 78

5.6 Discussion . . . . . 80

5.6.1 $CO_2$ and $CH_4$ adsorption on SWy-2: comparison with literature data . . . 81

5.6.2 Adsorbed phase in clay nanopores . . . . . 83

5.6.3 Modeling supercritical adsorption on geosorbents . . . . . 84

5.7 Concluding remarks . . . . . 87

**6 Supercritical sorption on illite and smectite clay minerals 89**

6.1 Introduction . . . . . 89

6.2 Materials and experimental methods . . . . . 90

6.2.1 Gas physisorption experiments . . . . . 90

6.2.2 High-pressure sorption experiments . . . . . 90

6.3 Results and discussion . . . . . 91

6.3.1 Textural properties of illite and smectite clay minerals . . . . . 91

6.3.2 Supercritical adsorption isotherms of $CO_2$ and $CH_4$ . . . . . 94

6.3.3 Supercritical adsorption model . . . . . 96

6.3.4 Adsorption energetics . . . . . 97

6.3.5 $CO_2$ and $CH_4$ in clay nanopores . . . . . 100

6.4 Concluding remarks . . . . . 102

**7 Supercritical sorption on hydrated clay minerals 103**

7.1 Introduction . . . . . 103

7.2 Materials and experimental methods . . . . . 105

7.2.1 Water sorption . . . . . 105

7.2.2 High-pressure adsorption experiments . . . . . 106

7.2.3 TGA . . . . . 107

7.2.4 XRD . . . . . 107

7.3 Results and discussion . . . . . 108
7.3.1 Water sorption isotherms . . . . . 108
7.3.2 Supercritical $CO_2$ and $CH_4$ adsorption . . . . . 114
7.4 Concluding remarks . . . . . 120

**8 Conclusion and future work** **123**

8.1 Concluding remarks . . . . . 123
8.2 Future work . . . . . 125
8.2.1 Workflow application to clay-rich rocks . . . . . 125
8.2.2 Binary adsorption of $CO_2$ and $CH_4$ . . . . . 126
8.2.3 Effect of various hydration states on supercritical sorption . . . . . 129
8.2.4 Direct observation of supercritical fluid confinement using neutron scattering techniques . . . . . 130

**A Surface area analysis** **155**

A.1 Brunauer-Emmett-Teller theory for surface area calculation . . . . . 155

**B Error analysis** **159**

B.1 Error propagation . . . . . 159
B.2 Error from linear regression . . . . . 160
B.2.1 Simple linear regression . . . . . 161
B.2.2 Weighted linear regression . . . . . 161

**C Pore discretization** **163**

C.1 Pore-size distribution . . . . . 163
C.2 Lattice pore discretization . . . . . 164

# List of Figures

2.1 Main building blocks of the layer structure of clay minerals: (a) a hexahedral network of interlinked $SiO_4$ tetrahedra forming a silica sheet and (b) a network of octahedra made up of oxygen and metal atoms. Graphics taken from Murray (2007) with modifications. . . . . 29

2.2 Clay mineral structure in different length scales showing the source of a wide range of porosity: (a) a layer, (b) a particle, (c) an aggregate of particles showing inter-particle spaces, (d) multiple aggregates showing interaggregate spaces, and (e) a 2:1 layer structure showing the interlayer spacing ($\Delta d$) and layer repeat distance ($d_{001}$ spacing). Graphics taken from Bergaya and Lagaly (2006) and Brigatti et al. (2006) with modifications. . . . . 30

2.3 Classification of various types of physisorption isotherms (Thommes et al., 2015). . 32

2.4 Excess adsorbed amounts of $CO_2$ and $CH_4$ on ZIF-8 as a function of pressure at 40 °C. The lines are to guide the eye. . . . . 33

2.5 Schematic representation of a density profile inside a pore. Graphic partially taken from (Parilla et al., 2016). . . . . 34

2.6 Absolute (squares), excess (circles), and net (triangles) adsorbed amounts of $CO_2$ on ZIF-8 as a function of pressure at 40 °C. The lines are to guide the eye. . . . . 36

2.7 (a) Excess sorption isotherms of $CO_2$ (closed symbols, 45 °C) and $CH_4$ (open symbols, 30 °C to 40 °C) on illite (Busch et al., 2008; Ji et al., 2012; Liu et al., 2013; Heller and Zoback, 2014; Jeon et al., 2014). (b) Excess sorption isotherms of $CO_2$ on montmorillonite (STx-1) at 35 °C and 50 °C (Rother et al., 2013). (c) Excess adsorption and desorption isotherms of $CO_2$ on montmorillonite (SCa-3) at 45 °C and 55 °C (Jeon et al., 2014). (d) Excess sorption isotherms of $CO_2$ on montmorillonite (STx-1b - squares, SWy-2 - circles) under dry (closed symbols) and moisture-equilibrated (open symbols) conditions at 45 °C (Busch et al., 2008). . . . . 37

3.1 Schematic diagram of the experimental setup for high-pressure adsorption experiments. The grey-filled valves indicate high-pressure valves. . . . . 42

3.2 Schematic diagram of the magnetic suspension balance at three different measuring positions. The pattern-filled parts indicate suspended parts at each measuring positions. . . . . 43

3.3 Normalized measured weight of the suspended metal parts including the sample holder plotted against the $CO_2$ bulk density at 60 °C (squares, the open top sample holder) and 80 °C (circles, the sample holder with a mesh lid). The closed symbols were measured by incrementally increasing the pressure and the open symbols were measured by decreasing the pressure. The negative value of the slope obtained from linear regression of the data points (dashed line) is equal to $V_{\mathrm{met}}$. . . . . 45

3.4 Measured values of (a) temperature (left axis) and pressure (right axis), and (b) corrected $MP_1$ ($MP_1 - ZP$, left axis) and corrected $MP_2$ ($MP_2 - ZP$, right axis) logged for approximately 13 h after pressurizing the measuring chamber with $CO_2$ up to 40 bar at 50 °C. . . . . 47

3.5 Excess adsorbed amounts of $CO_2$ (squares) at 20 °C up to 4.5 MPa and $CH_4$ (circles) at 25 °C up to 7.5 MPa measured with an empty basket. . . . . 48

3.6 Excess adsorbed amount of (a) $CO_2$ on first (squares) and second (circles) aliquots of ZSM-5 at 20 °C up to 4.5 MPa and (b) $CH_4$ on first (run 1 - squares; run 2 - circles) and second (run 1 - upward triangles; run 2 - downward triangles) aliquots of zeolite Y at 25 °C up to 7.5 MPa. The solid lines represent the reference isotherms obtained from Equation 3.6 and 3.7. The inset plots show the residuals ($n^{\mathrm{ex}}_{\mathrm{ref}} - n^{\mathrm{ex}}_{\mathrm{meas}}$) against pressure with the upper and lower bounds shown in red dashed lines. . . . 48

3.7 (a) Bulk density of $CO_2$ and $CH_4$ against pressure measured from the adsorption experiments shown in Figure 3.6 compared to the values calculated from the equations of state (solid lines) using REFPROP (Lemmon et al., 2018). (b) Reduced fluid density of $CO_2$ (closed symbols, left $y$-axis) and $CH_4$ (open symbols, right $y$-axis) against pressure measured from the sorption experiments on SWy-2 as another example of validation through density measurements up to 25 MPa. . . . . 49

4.1 Graphical representation of fluid molecules occupying lattice sites in a one-dimensional pore space as adopted by the LDFT model. The red double-headed arrow indicates the interaction between the wall and adsorbate ($\epsilon_{sf}$) while the blue double-headed arrow indicates the interaction between neighboring adsorbates ($\epsilon_{ff}$). Graphic taken from (Pini et al., 2010) with modifications. . . . . 55

4.2 Lattice occupancy profiles of $CO_2$ at 50 °C inside pores with (a) 3, (b) 15, and (c) 50 layers each representing micropores, small mesopores, and large mesopores, respectively. The values of $\theta_b$ are 0.2 (squares), 0.5 (circles), and 0.8 (upward triangles). The values of $\epsilon_{sf}/k$ and $\epsilon_{ff}/k$ used are $-1100$ K and $-101.4$ K, respectively. The value of $\epsilon_{sf}$ was chosen arbitrarily. . . . . 57

4.3 Excess adsorption isotherms of (a) $CO_2$ and (b) $CH_4$ at 50 °C produced by the LDFT model for multiple pores of varying number of lattice layers with $v_{pore} = 1\,cm^3/g$. The value of $\epsilon_{sf}/k$ is $-1100$ K and the values of $\epsilon_{ff}/k$ for $CO_2$ and $CH_4$ are $-101.4$ K and $-63.5$ K, respectively. The value of $\rho_{max}$ is equal to $\rho_c \times 2.5$ where $n^{ex} = 0$. The dotted lines represent $\rho_c$ and $\rho_{max}$. The values of $\epsilon_{sf}$ and $\rho_{max}$ were chosen arbitrarily. 59

4.4 Excess adsorption isotherms of (a) $CO_2$ and (b) $CH_4$ at 35 °C, 50 °C and 65 °C produced by the LDFT model for a pore with 10 lattice layers with $v_{pore} = 1\,cm^3/g$. The same values of $\epsilon_{sf}/k$, $\epsilon_{ff}/k$, and $\rho_{max}$ are used as Figure 4.3. The values of $T/T_c$ are 1.01, 1.06, and 1.11 for $CO_2$, respectively, and 1.62, 1.70, and 1.77 for $CH_4$, respectively. . . . . 60

5.1 (a) $N_2$ physisorption isotherm taken at 77 K: experimental data (symbols) and LDFT model (solid line). The upward facing arrow indicates the adsorption (closed symbols) branch while the downward facing arrow indicates the desorption (open symbols) branch. The inset plot shows the adsorption points for which $P/P^o \leq 0.001$. (b) Contribution to the total amount of $N_2$ adsorption by pores of different sizes modeled by the LDFT: micropores ($J = 4$, solid line), small mesopores ($J = 7$, dashed line), and large mesopores ($J = 100$, dotted line). . . . . 72

5.2 Incremental (symbols) and discretized (bars) pore volume plotted against the average pore width. Discretized pore-size distribution used for the LDFT model is labeled with the respective pore volume percentage for each pore. The average pore widths are translated to lattice model pores with given numbers of layers ($J = 4, 7, 17, 34, 46, 65, 100$, and 180). . . . . 73

5.3 Measured weight of the suspended metal parts (including the sample holder) and the SWy-2 sample plotted against the He bulk density at 115 °C before (squares) and after (circles) the high-pressure $CO_2$ sorption experiments. The closed symbols were measured by incrementally increasing the pressure up to 130 bar and the open symbols were measured by decreasing the pressure. The negative values of the slope obtained from the linear regression of the data points (dashed lines) are equal to $V_0 = V_{\mathrm{met}} + V_{\mathrm{s}}$. . . . . 74

5.4 Net adsorption of $CO_2$ (closed symbols) and $CH_4$ (open symbols) on SWy-2 at 25 °C to 115 °C up to 250 bar. The dashed lines represent the slope equal to $-V_{\mathrm{s}}/m_{\mathrm{s}}$. The inset plot shows the net adsorbed amount below 1 mol/L (the solid lines are added to guide the eye). . . . . 75

5.5 Excess sorption of supercritical $CO_2$ (closed symbols) and $CH_4$ (open symbols) on SWy-2 at 25 °C to 115 °C up to 250 bar. The symbols represent experimental data while the solid lines represent the LDFT model results at each temperature. . . . . 76

5.6 (a) Excess adsorption plotted against pressure at 25 °C to 115 °C and (b) the same data plotted as $\ln(n^{\mathrm{ex}}/P)$ versus $n^{\mathrm{ex}}$. The symbols represent experimental data for $CO_2$ (closed symbols) and $CH_4$ (open symbols), while the solid lines are fits obtained upon application of the virial equation, Equation 5.8. . . . . 79

5.7 $\ln(K_H)$ plotted as a function of the inverse temperature, $1/T$, for $CO_2$ (squares) and $CH_4$ (circles) on SWy-2 in the temperature range of 25 °C to 115 °C. The symbols are obtained from fitting the virial equation to the experimental adsorption points, while the dashed lines are linear fits used to estimate the differential enthalpy of adsorption, $\Delta h_0$. The solid lines represent the Henry constant estimated using the LDFT model and corrected by fitted values of the pre-factor $\tilde{K}_H^0$. . . . . 80

5.8 (a) Adsorption data of $CO_2$ on montmorillonite samples at 45 °C and 50 °C including results from this study (closed squares) and literature data on SWy-2 (Busch et al., 2008; Schaef et al., 2014) or Na-saturated STx-1 (Rother et al., 2013). Data from the present study combine measurements on two distinct SWy-2 samples using different gravimetric instruments by Rubotherm (closed squares and circles, the error bars have been omitted for visual clarity). (b) Adsorption data of $CH_4$ on SWy-2 (Fan et al., 2014; Schaef et al., 2014), Ca-rich montomorrilonite (Liu et al., 2013) and on a montomorillonite-rich sample (Ji et al., 2012) at 50 °C and 60 °C. . . . . 81

5.9 Pore volume saturation factor, $c_{sat}$, as a function of $1/T$, as predicted from the LDFT model fitted to the experimental supercritical adsorption data. Symbols represent model results at the given experimental temperature for $CO_2$ (squares) and $CH_4$ (circles), and the dashed line show $c_{sat} = 1$ that is attained at complete saturation. The inset plot shows the same values of $c_{sat}$ plotted against $T_c/T$, where $T_c$ is the critical temperature. . . . . 84

5.10 Relative deviations between experiment and model (LDFT - closed squares; Langmuir model - open circles) as a function of the bulk density for the isotherms measured at 50 °C on SWy-2 with (a) $CO_2$ and (b) $CH_4$. (c) The corresponding experimental excess adsorption isotherms (symbols) are compared to predictions by the LDFT (solid lines) and Langmuir model (dashed lines - two scenarios). The filled symbols are the same data reported in Figure 5.5, while the empty symbols are measurements carried out in a different Rubotherm balance up to 650 bar. . . . 86

5.11 (a) Lattice excess adsorption isotherms computed for $CO_2$ at 50 °C in two pores, namely 4 (micropores) and 17 layers (mesopores). The corresponding lattice occupancy profiles in (b) 4 layer pore and (c) 17 layer pore. The dashed lines represent the values of $\theta_b$: 0.25, 0.5, and 0.75. . . . . 86

6.1 Adsorption (closed symbols) and desorption (open symbols) isotherms of (a) $N_2$ at 77 K and (b) Ar at 87 K on the clay minerals. The inset plots show the filling of the micropores for $P/P^o < 0.01$. . . . . 91

6.2 Adsorption isotherms of $CO_2$ at 273 K up to 760 Torr ($P/P^o \approx 0.03$, $P^0 = 26141$ Torr). 92

6.3 Normalized measured weight plotted against the He bulk density for ISCz-1 (open symbols) and IMt-2 (closed symbols). The measurements on SWy-2 are shown in Figure 5.3 in Chapter 5. The measurements for ISCz-1 show three different data sets as the experiment was interrupted, therefore, multiple sets were measured to test the possibility of sample loss. . . . . 93

6.4 Supercritical adsorption (black) and desorption (grey) isotherms of $CO_2$ (filled symbols) and $CH_4$ (open symbols) on (a) SWy-2, (b) ISCz-1, and (c) IMt-2 up to 300 bar at 25, 50, 80 and 115 °C (loading decreases with increasing temperature). The inset plot of (c) shows the desorption points of IMt-2 under 1 mol/L. The solid lines are the LDFT model fits. . . . . 95

6.5 Excess adsorption isotherms of $CO_2$ (closed symbols) and $CH_4$ (open symbols) plotted in the virial format for (b) ISCz-1 and (c) IMt-2. The dashed lines are linear fits obtained with the two-parameter virial equation, and describe the linear regions that are well visible in the experimental isotherms. . . . . 97

6.6 (a) $\ln(K_H)$ plotted against the inverse temperature, $1/T$, for $CO_2$ (closed symbols inside the light grey area) and $CH_4$ (open symbols inside the dark grey area). The lines (solid – SWy-2, dashed – ISCz-1, dotted – IMt-2) are linear fits to obtain the isosteric enthalpy of adsorption at zero coverage. (b) Isosteric enthalpy of adsorption of $CO_2$ (black lines) and $CH_4$ (grey lines) plotted against excess amount of adsorption. 99

6.7 (a) $CO_2$ adsorption isotherm at 50 °C on SWy-2 (solid line) with isotherms of individual pores (dashed lines) in color. The pore sizes of the individual isotherms are indicated by the color scale. (b) – (d) Lattice occupancy profiles corresponding to three density values highlighted in (a) – maximum amount of adsorption, $n^{ex}{}_{max}$, and points before and after $n^{ex}{}_{max}$ with the same amount of excess adsorption – for the lattice pores with 3 (1.2 nm, square), 6 (2.4 nm, circle), 19 (7.6 nm, upward triangle), and 31 (12.4 nm, downward triangle) layers. . . . . 100

6.8 Saturation factors of $CO_2$ (closed symbols) and $CH_4$ (open symbols) as a function of $T_c/T$. The inset plot shows the same values against $1/T$. The linear regression of the data shown in the plot can be described by the equation $c_{sat} = 1.07(T_c/T) - 0.07$. The value of $c_{sat}$ of ISCz-1 at 50 °C was omitted in linear regression for the reason discussed in the main text, and the intercept was corrected to equate the value of $c_{sat}$ to unity as $T_c/T$ approaches unity. . . . . 101

7.1 Water adsorption (closed symbols) and desorption (open symbols) isotherms on four source clay minerals at 293 K (a) up to 15.8 Torr (RH of 0.9) and (b) up to RH of 0.5 (only adsorption data are shown for visual clarity). . . . . 108

7.2 (a) TGA curves and (b) DTG curves that show two distinct regions of significant weight loss for all four clay minerals: one below 200 °C and another at approximately between 500 °C to 700 °C. . . . . 109

7.3 (a) Water adsorption isotherms of STx-1b and SWy-2 (closed symbols, left $y$-axis, indicated by arrows) from Figure 7.1a and $d_{001}$ spacing (open symbols, right $y$-axis, indicated by arrows) collected from the literature. For STx-1b, the squares are from Schaef et al. (2015) (50 °C and 90 bar), the circles are from Morodome and Kawamura (2009) (50 °C), and the upward triangles are from Sato et al. (1992). For SWy-2, the downward triangles are from Loring et al. (2014) (50 °C and 90 bar), the diamonds are from Morodome and Kawamura (2009) (50 °C), and left triangles are from Sato et al. (1992). (b) Unconstrained volumetric swelling obtained from the difference between the accessible pore volumes estimated from the adsorption isotherms of water and Ar. . . . . 113

7.4 (a) XRD patterns of the four clay minerals after being completely dried at 200 °C and (b) XRD patterns of dry and hydrated STx-1b. . . . . 114

7.5 (a) Desorption isotherms of STx-1b and SWy-2 and (b) unconstrained volumetric swelling obtained from the desorption isotherms of water and Ar. . . . . 115

7.6 Excess sorption isotherms of $CO_2$ (squares) and $CH_4$ (circles) on (a) STx-1b and (b) IMt-2 under dry (closed symbols) and hydrated (open symbols) conditions at 50 °C. The inset of (a) shows the difference in the excess amounts of sorption between dry and hydrated STx-1b ($\Delta n^{ex} = n^{ex}_{hyd} - n^{ex}_{dry}$) plotted against pressure. No distinction was made between adsorption and desorption points for dry clay minerals, and error bars were omitted for visual clarity. The values of uncertainty were below 0.029 mmol/g and 0.014 mmol/g for $CO_2$ and $CH_4$, respectively, on STx-1b and 0.014 mmol/g and 0.010 mmol/g, respectively on IMt-2. . . . . 116

7.7 Schematic representation of the STx-1b interlayer under (a) dry and (b) hydrated conditions. The atoms are color coded as such, blue is hydrogen, red is oxygen, silicon is light gray, aluminum is dark gray, black is carbon, and white and light blue is calcium. The schematic of the STx-1b layers was taken from the structure of Ca-montmorillonite (STx-1) obtained from Downs and Hall-Wallace (2003), documented by Viani et al. (2002), and visualized using VESTA (Momma and Izumi, 2011). The basal spacing ($d_{001}$ spacing) is the sum of the interlayer spacing and the T-O-T layer. . . . . 118

7.8 Discretized pore volume distributions of (a) dry and (b) hydrated STx-1b used as input parameters for the LDFT model. The extra bar in (b) represents the extra pore volume of 0.017 $cm^3$/g contributed by interlayer expansion. . . . . 119

8.1 $CO_2$ adsorption (closed symbols) and desorption (open symbols) isotherms on Opalinus Clay, STx-1b, SWy-2, ISCz-1, and IMt-2 at 50 °C. Error bars are omitted for visual clarity. . . . . 126

8.2 Schematic representation of the two-step gas expansion experiment in which a container with an unknown volume of $V_1$ is connected to the measuring chamber for the first step of the experiment (top). The second step of the experiment involves the same container filled with steel balls with a known volume of $V_{balls}$ (bottom). . 128

8.3 (a) Top and (b) side view of the design of a sample basket for holding extra adsorbent materials to induce greater change in the bulk phase composition. The sample basket was designed and machined by Mr. Gavin Barnes from the Department of Chemical Engineering Workshop. . . . . 129

A.1 $v(P^{o} - P)$ plotted against $P/P^{o}$ for (a) $N_2$, (b) Ar, (c) water adsorption, and (d) water desorption on STx-1b (squares), SWy-2 (circles), ISCz-1 (upward triangles), and IMt-2 (downward triangles). The closed symbols are the data points for which $v(P^{o} - P)$ increases monotonically as a function of $P/P^{o}$. The linearized form of the BET equation is plotted for (e) $N_2$, (f) Ar, (g) water adsorption, and (h) water desorption on the four clay minerals where the points within the linear range (closed symbols) are used to estimate $S_{BET}$. The dashed lines are linear regression fits. . . 157

C.1 (a) $N_2$ and (b) Ar adsorption isotherms (symbols) with NLDFT fits (solid lines) for four source clay minerals in this thesis. . . . . 163

C.2 Pore-size distributions of the four source clay minerals studied in this thesis up to 20 nm obtained from (a) $N_2$ and (b) Ar adsorption isotherms. The inset plots show the same distribution curves below 4 nm. . . . . 164

C.3 $CO_2$ adsorption isotherms (symbols) with GCMC fits (solid lines) of the four source clay minerals in this thesis. . . . . 164

C.4 Pore volume distributions (solid lines, left $y$-axis) obtained from the Ar and $CO_2$ adsorption isotherms shown up to 20 nm. The volumes of the discretized pores (in 5 nm increments) are shown in bars (right $y$-axis) and their respective volume percentages are labeled. The number of layers for the chosen lattice pores are as follows: 3 (1.2 nm), 4 (1.6 nm), 6 (2.4 nm), 19 (7.6 nm), 31 (12.4 nm), 44 (17.6 nm), and 60 (24 nm). . . . . 165

# List of Tables


2.1 Illite-smectite clay mineral content in geological formations (wt%) . . . . . 28

5.1 Structural properties of the source Na-montmorillonite clay used in this study (SWy-2). [(a)]Data obtained from $N_2$ physisorption analysis. [(b)]BET surface area obtained by $N_2$ physisorption. [(c)]Lower and upper estimate by Deeds and Van Olphen (1961a) refer to pycnometry measurements and crystallographic data, respectively; He-gravimetry was applied in this study. . . . . 71

5.2 LDFT model parameters for the description of $CO_2$, $CH_4$ and $N_2$ adsorption on SWy-2 at sub- and supercritical conditions. . . . . 72

5.3 Henry constants, first-order virial coefficient and adsorption selectivity for $CO_2$ and $CH_4$ on SWy-2. . . . . 79

5.4 Experimental details of literature study . . . . . 82

5.5 Langmuir model parameters . . . . . 85

6.1 Summary of the textural properties of SWy-2, ISCz-1, and IMt-2. . . . . 92

6.2 LDFT model parameters . . . . . 96

6.3 Comparison of the calculated adsorbed densities of $CO_2$ and $CH_4$ with their respective liquid densities. . . . . 97

6.4 Henry's constants, selectivity, and enthalpy of adsorption at zero coverage for $CO_2$ and $CH_4$ adsorption on SWy-2, ISCZ-1, and IMt-2. . . . . 98

7.1 Surface area of clay samples measured by $N_2$, Ar, and $H_2O$ in comparison with literature values[†] . . . . . 110

7.2 BET surface areas, $S_{\mathrm{BET,w}}$, calculated from water adsorption and desorption isotherms 111

7.3 Skeletal density of dry and hydrated STx-1b and IMt-2 and the amount of pre-adsorbed water obtained from the difference between the measured weight of hydrated and dry samples (degassed at 200 °C after each experiments) . . . . . 115

7.4 LDFT model parameters . . . . . 119

8.1 Summary of the textural properties of Opalinus Clay, ISCz-1, and IMt-2 . . . . . 125

A.1 BET parameters obtained from $N_2$, Ar, and water isotherms . . . . . 156

# Chapter 1

# Introduction

The physical interactions between clay minerals and supercritical fluids, particularly $CO_2$ and $CH_4$, have received increasing attention in the context of geo-energy technologies, such as the geological storage of $CO_2$ in sedimentary rock formations or the production of natural gas from unconventional shale play (Bourg et al., 2015; Rutter et al., 2017). Clay minerals are abundant in geological formations (approximately 30 wt% of all sedimentary rocks (Lynch, 1997)), appearing in a wide range of concentrations in sandstone reservoirs (up to 50 vol% (Han et al., 1986)) and in the caprock seals above them (typically consisting of thick layers of mudstones or shales with clay mass fractions in the range of 30 % to 80 % (Bourg et al., 2015)). They are also major constituents of organic-rich shale formations that are being exploited for hydrocarbon recovery (e.g. Barnett: 3 vol% to 40 vol%, Haynesville: 20 vol% to 40 vol%, and Eagleford: 6 vol% to 20 vol% (Sone and Zoback, 2013)). The presence of clays contributes largely to the sub-micron properties of these rocks, including the presence of nanoscale pores with width less than 100 nm, which produces a large surface area available for physical interactions with reservoir fluids. One significant physical interaction within clay nanopores is gas adsorption, which creates a dense adsorbed phase that increases gas storage capacity (Busch et al., 2008; Heller and Zoback, 2014) and affects the gas transport through the pore matrix (Song and Zhang, 2013). In a typical sandstone reservoir, sorption of $CO_2$ by clay minerals can increase $CO_2$ storage capacity by up to 20 % to 30 % relative to the capacity associated with residual trapping (Busch et al., 2016; Wan et al., 2018). Sorption of $CO_2$ on the mudstones that form the majority of caprocks has shown to enhance the sealing efficiency and retention potential from retarded diffusion of the gas (Wollenweber et al., 2010; Amann et al., 2011; Amann-Hildenbrand et al., 2013). The excess uptake

by adsorption in hydrocarbon shale reservoirs contributes to 20 % to 80 % of the total gas-in-place (Lu et al., 1995; Curtis, 2002; Montgomery et al., 2005; Ambrose et al., 2012). Therefore, adsorption on clays creates potential for (i) significant gas storage for reservoirs having large clay contents, (ii) enhanced gas production from clay-rich shale formations, and (iii) increased sealing efficiency by limiting diffusion through the seals above potential $CO_2$ sequestration sites. Consequently, reliable experimental data are key towards evaluating the sealing stability and capacity of potential storage sites upon introduction of supercritical $CO_2$ (Busch et al., 2010) or to devise injection policies that increase hydrocarbon production from unconventional reservoirs (Middleton et al., 2015).

The objective of this Ph.D. thesis is to better our understanding of the adsorption properties and behaviors of clay minerals for $CO_2$ and $CH_4$ under subsurface conditions. Chapter 2 and 5 discuss the lack of agreement (often showing opposing interpretations) among the data sets of supercritical adsorption of $CO_2$ and $CH_4$ on clay minerals reported in the literature. This observation of scattered data sets is partly due to the intrinsic difficulty of measuring adsorption at elevated pressure and temperature conditions, especially for relatively weakly adsorbing materials like clay minerals, and the lack of attention paid to the level of uncertainty associated with the adsorption measurements. Also, little focus has been given to the hydration state of clay minerals in the context of supercritical fluid uptake despite the significance of the effect of water on the adsorption capacities, especially for swelling clay minerals. As a matter of fact, the inconsistency in the level of dehydration achieved for the clay mineral samples may be partially responsible for the disparity observed in the literature data. Moreover, studies are often limited to one fluid ($CO_2$ or $CH_4$) and to one temperature (or to a fairly narrow range), which precludes any effort to extract thermodynamic adsorption parameters (e.g. selectivity, enthalpy of adsorption, etc.) that are needed to develop models with a sufficient degree of predictive capability. In this context, most studies aimed at reconciling experimental adsorption data on clay minerals have used empirical models, such as the Langmuir model, which cannot capture the effects arising from the textural complexity of clay minerals and clay-rich rocks, such as adsorption behaviors caused by pores of different types and sizes.

In this Ph.D. work, an experimental setup that includes a magnetic suspension balance has been used to measure a comprehensive set of adsorption and desorption isotherms of $CO_2$ and $CH_4$ gravimetrically at elevated pressure (up to 300 bar) and temperature (25 °C to 115 °C) on three types of clay minerals (both dry and hydrated): smectite, illite-smectite mixed layer, and illite. To establish a baseline for future studies on clays and clay-rich rocks, relatively homogeneous samples

of clay minerals sourced from the Clay Minerals Society have been used. Multiple characterization methods, including gas and vapor sorption, He gravimety, thermogravimetric analysis, and X-ray diffraction, were utilized to quantify many structural characteristics of these clay minerals (e.g. accessible surface area and pore volume, skeletal density, interlayer spacing, etc.). The physical properties are discussed in association with the adsorption properties of the clay minerals under supercritical conditions and with the insight provided by the lattice density functional theory (LDFT) on the pore-specific adsorption behaviors and filling capacities. Such features are key towards describing supercritical adsorption on clay minerals and clay-bearing rocks that are characterized by a wide range of micro- and mesoporosity.

## 1.1 Thesis structure

Chapter 2 presents the fundamentals of adsorption phenomena with emphasis on adsorption of supercritical fluids and a review of the current state of research on adsorption on clay minerals. The review of the literature includes a description of the microscopic structural properties of clay minerals that play a major role in their adsorption behaviors, as well as the existing sorption data on various clay minerals, which present the main knowledge gaps that are addressed in this thesis.

Chapter 3 introduces the experimental apparatus that has been commissioned and set up to gravimetrically measure adsorption and desorption of $CO_2$ and $CH_4$ on clay minerals under subsurface conditions. The specifications of the setup are detailed with emphasis on the setup's main experimental instrument, the magnetic suspension balance. The operating principles of the magnetic suspension balance are presented as well as the equations used to calculate the amount of adsorption from the measured weight data. The chapter also presents the calibration measurements conducted to calculate certain physical properties of the components inside the measuring chamber needed for data processing and analysis. Lastly, adsorption data measured to validate the accuracy of the data produced by the setup conducted as part of an interlaboratory study are presented.

Chapter 4 presents the details of the adsorption model based on the LDFT adopted to describe supercritical sorption of $CO_2$ and $CH_4$ in this thesis. The LDFT model, also commonly known as the Ono-Kondo lattice model, incorporates the structural properties of adsorbent materials, namely the pore volume and pore-size distribution, making it an apt model for modeling adsorption on clay minerals characterized by complex and wide ranges of micro- and mesoporosity. The chapter introduces the derivation of the LDFT model equations and the approximations of the model

parameters, some of which are used as fitting parameters to obtain a good agreement between the model results and experimental data. The physical significance of these parameters are discussed in Chapter 5 and 6.

Chapter 5 presents a workflow for measuring and modeling adsorption of supercritical $CO_2$ and $CH_4$ on clay minerals using Na-rich montmorillonite (smectite clay mineral). The chapter reports on the challenges of measuring accurate and reliable sorption data, including the major sources of error that arise from the determination of key structural features of clay minerals, namely their skeletal volume. The importance of accounting for the sources of error is highlighted by comparing the measured adsorption isotherms of Na-montmorillonite to a set of isotherms collected from the literature on montmorillonite samples. Moreover, the adsorption isotherms are modeled using the LDFT model taking into consideration the structural properties of the clay mineral determined from the analysis of low-pressure gas sorption experiments. The model results are discussed with emphasis on the physical significance of the fitted parameters, and compared to the fits obtained from the Langmuir adsorption model.

The workflow is further extended to other types of clay minerals, illite-smectite mixed layers and illite, in Chapter 6, in which the sorption capacities and behaviors of these different clay minerals are compared and discussed. The findings reported in Chapter 5 are corroborated by the inclusion of these clay minerals.

Chapter 7 discusses the effect of water on the sorption capacities of Ca-rich montmorillonite (smectite clay mineral) and illite for $CO_2$ and $CH_4$ to provide a more realistic picture of the interactions between supercritical $CO_2$ and $CH_4$ with clay minerals and clay-rich rocks that exist in various hydration states in subsurface environments. The chapter reports sorption measurements of $CO_2$ and $CH_4$ on dry and hydrated Ca-rich montmorillonite and illite. The sorption capacities of Ca-rich montmorillonite for both $CO_2$ and $CH_4$ increase upon hydration, which is ascribed to the entry of $CO_2$ and $CH_4$ molecules inside the expanded interlayers of Ca-rich montmorillonite inaccessible under dry conditions. The absence of an appreciable change in the sorption amounts on illite (non-expandable) confirms this interpretation. The chapter also emphasizes the significance of a systematic approach of quantifying the hydration states of clay minerals in high-pressure sorption experiments, achieved by independently measuring water sorption as a function of relative humidity.

Chapter 8 summarizes the main accomplishments and findings of this thesis and suggests directions for extending them with four research projects that can be pursued in the future.

# Chapter 2

# Background and literature review

## 2.1 Introduction

In this chapter, a general overview is provided on the microscopic morphology and structure of the clay minerals and background information on adsorption phenomena. A review of the literature is also presented on reported adsorption data on clay minerals with a focus on observations that are closely associated with and addressed by the work in this thesis.

## 2.2 Clay minerals

The formations of reservoir rocks and caprock seals, mostly comprised of shales and sandstones, are dominated by quartz and clay minerals (Cole et al., 2010). It is then apparent that the properties of these rocks, such as the porosity, permeability, and surface reactivity, are affected by their clay mineralogy (Lu et al., 1995; Worden and Morad, 2003; Ross and Bustin, 2009; Wollenweber et al., 2010), which tends to be dominated by illite and smectite clay minerals (Weaver, 1956). Despite the distinct physical properties between these two types of clay minerals, they are closely related in that smectite clay minerals transform into illite at higher burial depth, also resulting in the formation of illite-smectite mixed layers (Hower et al., 1976; Środoń, 2009; Busch et al., 2016; Wilson et al., 2016). This thesis focuses on these three types of clay minerals (hereafter collectively referred to as illite-smectite clay minerals) due to their dominating presence in subsurface rocks. Table 2.1 summarizes the mass fractions of illite-smectite clay minerals in shales and sandstones found around the globe.

Table 2.1: Illite-smectite clay mineral content in geological formations (wt%)

| Reference | Sample | I+S | Sum clay |
|---|---|---|---|
| Kuila and Prasad (2013) | Silver Hill Cambrian Shale | 89 | 90 |
| | Niobara Chalk D 3150 | 35 | 35 |
| | Niobara Chalk D 3161 | 20 | 20 |
| | Niobara Marl B-C 3060 | 24 | 24 |
| | Middle Bakken | 6 | 6 |
| | Pierre Shale | 36 | 44 |
| | Cox Argillite | 40 | 44 |
| | Woodford Shale | 17 | 17 |
| | North Sea Shale | 56 | 71 |
| | Mancos B Shale | 28 | 35 |
| Busch et al. (2008) | Muderong Shale | 35 | 66 |
| Lynch (1997) | Frio Shale | 79 | 99 |
| Kwon et al. (2001) | Wilcox Shale | 31 | 55 |
| Duan et al. (2016) | Nanchuan Shale | 16 | 24 |
| Busch et al. (2017) | Opalinus Clay | 48 | 75 |
| Wong et al. (1997) | Boise II Sandstone | - | 13 |
| | Bentheimer Sandstone | - | <10 |
| Shehata and Nasr-El-Din (2014) | Buff Berea Sandstone | 1 | 4 |
| | Grey Berea Sandstone | 2 | 8 |
| | Bandera Sandstone | 10 | 14 |
| | Parker Sandstone | 4 | 6 |
| Rutter and Mainprice (1978) | Tennessee Sandstone | - | 10 |
| Zang et al. (1996) | Flechtingen Sandstone | 15 | 15 |
| Armitage et al. (2013) | Mercia Mudstone | 25 | 29 |

I+S = total dioctahedral 2:1 layer clay: smectite, illite, and mixed-layer of illite and smectite.

The joint nomenclature committee of Association Internationale pour l'Etude des Argiles (AIPEA) and Clay Minerals Society (CMS) defined the term *clay mineral* as *"phyllosilicate minerals and minerals which impart plasticity to clay, and harden upon drying or firing"* (Guggenheim and Martin, 1995). This definition is quite broad in a sense that it does not restrict clay minerals to a specific type of mineral with a particular range of grain size. Within the scope of this thesis, the term *clay mineral* is restricted to a class of hydrous phyllosilicate ('phyllo' meaning leaf-like) minerals of colloidal size (1 nm to 1 µm) that are widely distributed in fine-grained fractions of rocks, soils, and sediments in the subsurface environments (Worden and Morad, 2003; Bergaya and Lagaly, 2006; Rouquerol et al., 2014). Despite the distinction between the terms *clay* and *clay minerals* (Bergaya and Lagaly, 2006), they are often used interchangeably for brevity as it is also the case in this thesis. Clay minerals are primarily characterized by their layer structure consisting of two main components as graphically represented in Figure 2.1: a sheet of tetrahedra and octahedra made of oxygen (or hydroxyl) ions. The center atoms of the tetrahedra unit composed of four closely packed oxygen ions are silicon atoms, although $Al^{3+}$ and $Fe^{3+}$ may also occupy the center to a lesser extent. These tetrahedra units share three basal oxygen atoms ($O_b$) with adjacent tetrahedra units

to form a tetrahedra sheet with a hexagonal mesh pattern (Brigatti et al., 2006). The octahedra unit consists of six closely packed anions (dominantly oxygen, but also include hydroxyl ions) with $Al^{3+}$ as the center atom making most clay minerals aluminosilicates, but $Mg^{2+}$, $Fe^{3+}$, and $Fe^{2+}$ may also serve as the center atom. The octahedra units share their edges to form a pseudo-hexagonal octahedral sheet. The tetrahedral and octahedral sheets can be stacked together in

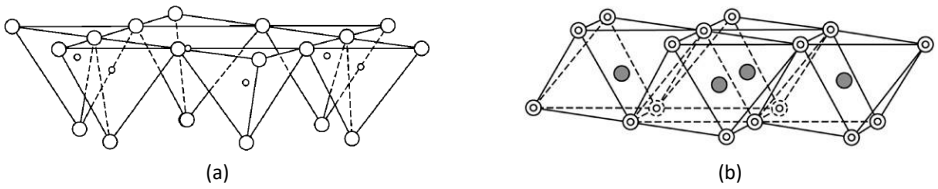



Figure 2.1: Main building blocks of the layer structure of clay minerals: (a) a hexahedral network of interlinked $SiO_4$ tetrahedra forming a silica sheet and (b) a network of octahedra made up of oxygen and metal atoms. Graphics taken from Murray (2007)[a] with modifications.

[a]Republished with permission of Elsevier Science & Technology Journals, from Applied Clay Mineralogy: Occurrences, Processing and Application of Kaolins, Bentonite, Palygorskite-sepiolite, and Common Clays, H. Murray, vol. 2, 1st edition, 2007; permission conveyed through Copyright Clearance Center, Inc.

different alternating sequences to form a layer. If each layer is composed of one octahedral sheet directly attached to one tetrahedral sheet (TO), the structure is defined as a 1:1 type. If each layer is composed of one octahedral sheet sandwiched between two tetrahedral sheets (TOT), the structure is defined as a 2:1 type. The illite-smectite clay minerals are of 2:1 type. The resulting layers are held together by secondary forces (e.g. van der Waals forces, hydrogen bonding, etc.) to create individual particles of clay minerals, the widths of which can range from 0.001 µm to 1 µm (Rouquerol et al., 2014). As shown in Figure 2.2, the spaces between particles (interparticle) and aggregates of particles (interaggregate) compose the majority of meso- (larger than 2 nm and less than 50 nm) and macropores (larger than 50 nm) of clay minerals. While the interparticle spaces also impart some microporosity to the clay mineral microstructure, the clay micropores (smaller than 2 nm) also come from the space between the layers, known as interlayer spacing (often denoted by $\Delta d$) (Brigatti et al., 2006).

### 2.2.1 Smectite

Smectite is a group of expanding or swelling clay minerals (e.g. montmorillonite, saponite, and hectorite). It is this swelling characteristic that makes smectite an important class of clay minerals to investigate for geological sequestration of $CO_2$ (De Jong et al., 2014; Michels et al., 2015;

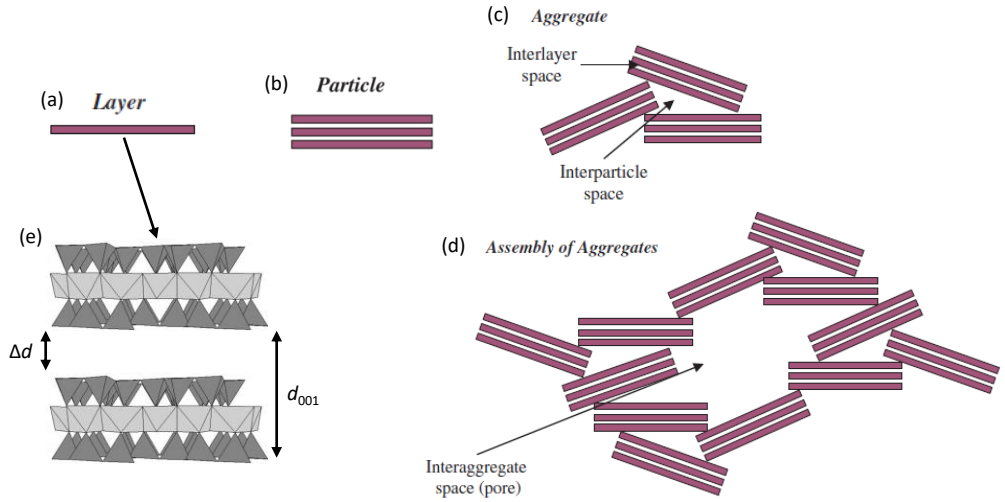



Figure 2.2: Clay mineral structure in different length scales showing the source of a wide range of porosity: (a) a layer, (b) a particle, (c) an aggregate of particles showing interparticle spaces, (d) multiple aggregates showing interaggregate spaces, and (e) a 2:1 layer structure showing the interlayer spacing ($\Delta d$) and layer repeat distance ($d_{001}$ spacing). Graphics taken from Bergaya and Lagaly (2006)[a] and Brigatti et al. (2006)[b] with modifications.

[a]Republished with permission of Elsevier Science & Technology Journals, from Handbook of Clay Science, F. Bergaya, G. Lagaly, vol. 1, 1st edition, 2006; permission conveyed through Copyright Clearance Center, Inc.

[b]Republished with permission of Elsevier Science & Technology Journals, from Handbook of Clay Science, M. Brigatti, E. Galan, B. Theng, vol. 1, 1st edition, 2006; permission conveyed through Copyright Clearance Center, Inc.

Bakhshian and Sahimi, 2017). Smectite clay minerals can undergo substitutions of the center ions in both the tetrahedral and octahedral sheet; $Si^{+4}$ is substituted by $Al^{+3}$ in the tetrahedral sheet and $Al^{+3}$ by divalent cations in the octahedral sheet. The excess negative charge caused by the substitution is compensated by interlayer cations that are exchangeable and hydrated, usually $Na^{+}$, $K^{+}$, $Ca^{2+}$, and $Mg^{2+}$ (Kloprogge et al., 1999). While the layer repeat distance of smectite is approximately 1 nm (Holtz and Kovacs, 1981; Rouquerol et al., 2014), the penetration of water molecules into the interlayer spaces causes the layer lattice to expand, resulting in a further increase in the interlayer distance. The degree of expansion between the layers depends on the nature of the interlayer cations and their hydration states (Wilson et al., 2014), and may occur in discrete steps for some smectic clay minerals via sequential formations of water layers in the interlayer space (Norrish, 1954). The number of water layers in smectic clay minerals is denoted by W: 0W for dehydrated smectite, 1W for smectite with one layer of water molecules, 2W for bilayer hydrated smectite, and so forth (Loring et al., 2012; Rother et al., 2013). The expanding nature of smectite clay minerals upon hydration has significant implications in their adsorption capacities as discussed in Chapter 7.

### 2.2.2 Illite

Illite is another group of clay minerals with the 2:1 layer structure, but is non-expandable unlike smectite clay minerals. The charge deficiencies in illite come from the substitution of $Si^{+4}$ by $Al^{+3}$ in the tetrahedral sheet, and $Al^{+3}$ by $Mg^{+2}$ or $Fe^{+2}$ in the octahedral sheet. The charge deficiency in illite is balanced dominantly by $K^{+}$ cations in the interlayer space. However, illite does not show swelling behavior due to the strong O-K-O bonds despite the presence of interlayer cations (Worden and Morad, 2003).

### 2.2.3 Illite-smectite mixed layer

During the illitization process of smectite clay minerals (proceeding with depth), the layers of the two clay minerals described above are randomly interstratified to form mixed layers of illite and smectite. As expected, gradual changes in the textural properties are observed as the mixed layer becomes more illite-rich through the illitization process (Hower et al., 1976; Środoń, 1999; Worden and Morad, 2003; Brigatti et al., 2006). Consequently, the structural properties, such as surface area or interlayer characteristics, of illite-smectite mixed layer resemble those of their pure end-member clay minerals. Chapter 6 and 7 discuss these properties in association with their adsorption properties.

Illite and illite-smectite mixed layers present particular significance to the application of enhanced gas recovery. The transformation of smectite into illite occurs approximately in the temperature range of 60 °C to 160 °C (Ijiri et al., 2018) (with surrounding $K^{+}$ cations present for the reaction), which coincides with the temperature condition that allows peak hydrocarbon generation (Pevear, 1999; Jiang, 2012). Furthermore, the amount of illite (or illite present in illite-smectite mixed layers) can be used to assess and predict the degree of potential hydrocarbon generation. Therefore, adsorption data of $CH_4$ on illite-smectite mixed layers and illite measured in this thesis in the temperature range of 25 °C to 115 °C present specific relevance to the application of unconventional hydrocarbon recovery.

## 2.3 Adsorption phenomena

Adsorption is generally defined as the enrichment of molecules, atoms, or ions in the vicinity of an interface (Thommes et al., 2015). In the scope of this thesis, the phenomenon is more narrowly

defined to occur in gas/solid systems where gas molecules are densified on the solid surface. In this system, the solid is called an adsorbent, while the gas molecules are defined as adsorptives (in the free phase) or adsorbates (in the adsorbed phase). Adsorption can be further classified as physical (physisorption) or chemical adsorption (chemisorption). Physisorption is characterized by weak van der Waals interactions while chemisorption is characterized by intermolecular covalent bonding between adsorbates and adsorbents (Gregg and Sing, 1982; Zhang et al., 2012; Thommes et al., 2015). Again, the phenomenon considered in the scope of this thesis is restricted to only physisorption.

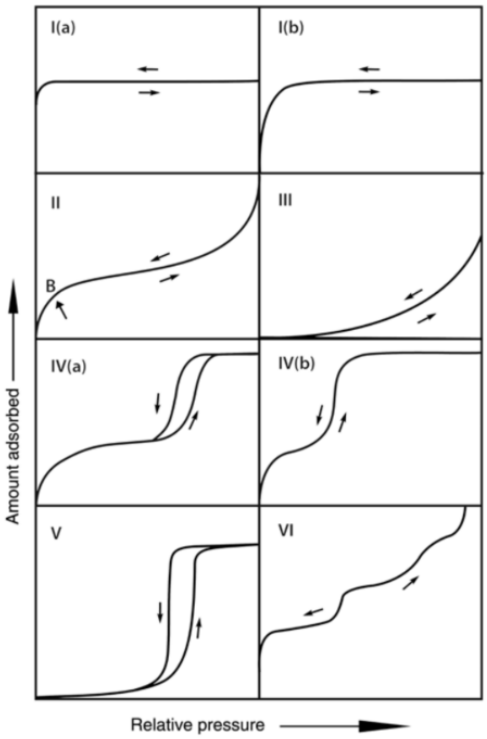



Figure 2.3: Classification of various types of physisorption isotherms (Thommes et al., 2015)[a].

[a]Reprinted from Pure and Applied Chemistry. M. Thommes, K. Kaneko, A. Neimark, J. Olivier, F. Rodriguez-Reinoso, J. Rouquerol, K. Sing, Copyright 2015

The amount of adsorbed gases, or fluids, is typically reported in a graphical form known as an adsorption isotherm at a fixed temperature. The independent axis of adsorption isotherms is usually reported in relative pressure ($P/P^{o}$) for adsorption in the subcritical region whereas the equilibrium pressure or bulk density is used for supercritical adsorption (Thommes et al., 2015). The dependent axis of adsorption isotherms is expressed in specific terms (normalized by the physical property of the adsorbent, such as mass, surface area, or volume) to allow ready comparison be-

tween adsorbed amounts of different materials (Zhang et al., 2012). In an effort to standardize various isotherm types, six types of physisorption isotherms were classified by an IUPAC report (Sing et al., 1985) based on the original definition by Brunauer (1943). Since then, new types of isotherms have been identified as shown in Figure 2.3. Each isotherm corresponds to adsorption isotherms on materials with varying porous properties (e.g. micro-, meso-, and macropores as described above), and the detailed descriptions of each isotherm can be readily found in the literature (Brunauer, 1943; Gregg and Sing, 1982; Ruthven, 1984; Rouquerol et al., 2014; Thommes et al., 2015).

### 2.3.1 Adsorption isotherms: absolute, excess, and net

The isotherms included in the IUPAC classification in Figure 2.3 all show the adsorbed amount as an increasing function of relative pressure, plateauing to a constant value for types I, IV, and V. However, adsorption isotherms of supercritical fluids reach a maximum adsorbed amount and decrease with increasing pressure as shown in Figure 2.4. This discrepancy between the IUPAC classification and experimental measurements at high pressure stems from the conceptual difference between various measures for the amount of gas adsorbed on a solid surface over a wide range of pressure (Aranovich and Donohue, 1997; Donohue and Aranovich, 1998). Figure 2.4 shows the

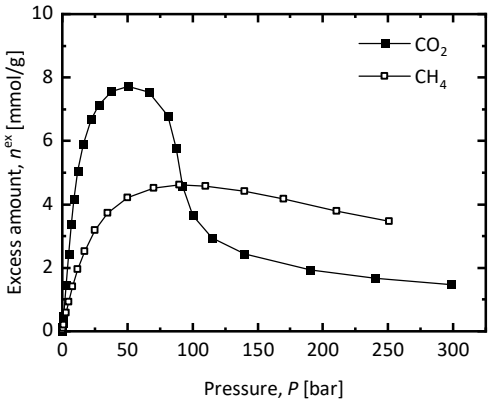



Figure 2.4: Excess adsorbed amounts of $CO_2$ and $CH_4$ on ZIF-8 as a function of pressure at 40 °C. The lines are to guide the eye.

*excess* adsorbed quantities of $CO_2$ and $CH_4$ on ZIF-8 (Basolite Z1200, Sigma-Aldrich) rather than the *absolute* amount of adsorption, as a function of gas equilibrium pressure up to 300 bar. As previously mentioned, the isotherms in Figure 2.4 are not monotonic functions of pressure, but decrease after reaching a maximum at approximately 50 bar and 90 bar for $CO_2$ and $CH_4$,

respectively.

Three definitions of adsorption are used: absolute, excess (or Gibbsian excess), and net. The local density profile of the adsorbate at the interfaces inside a pore can be represented graphically as shown in Figure 2.5. The adsorbate component is densified at the solid surface, but the density

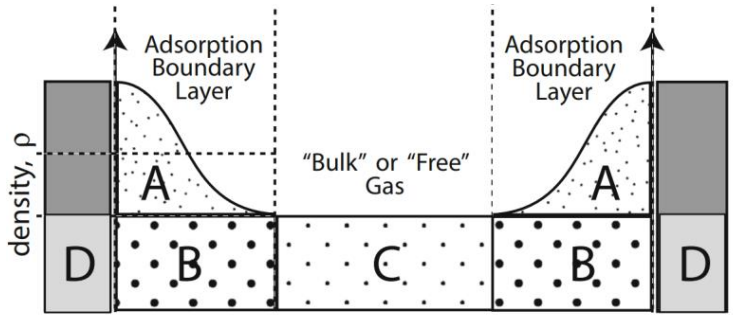



Figure 2.5: Schematic representation of a density profile inside a pore. Graphic partially taken from (Parilla et al., 2016)[a].

[a]Reprinted by permission from Springer Customer Service Centre GmbH: Springer Nature. Applied Physics A: Materials Science & Processing. P. Parilla, K. Gross, K. Hurst, T. Gennett, Copyright 2016

decreases gradually as the distance from the surface increases. At an unknown distance (equal to the thickness of the adsorbed layer, shown by the adsorption boundary layer in Figure 2.5), the density of the adsorbate becomes equal to that of the bulk phase, which is only a function of gas equilibrium pressure under isothermal conditions. The *absolute* amount adsorbed (in moles) in the adsorbed layer, $n^{\mathrm{a}}$ (A + B in Figure 2.5), along the axis perpendicular to the surface may be defined as:

$$n^{\mathrm{a}} = \int_0^{V_{\mathrm{a}}} \rho dV = n^{\mathrm{t}} - \rho_{\mathrm{b}} V_{\mathrm{b}} \tag{2.1}$$

where $V_{\mathrm{a}}$ is the volume occupied within the adsorption boundary layers, $\rho$ is the density (subscript $b$ represents that of the bulk phase), $V_{\mathrm{b}}$ is the volume occupied by the bulk phase, and $n^{\mathrm{t}}$ is the total amount of adsorbate component in the system (A + B + C in Figure 2.5). Equation 2.1 shows that absolute adsorption cannot be evaluated without knowing either $V_{\mathrm{b}}$ or the variation of $\rho$ within the pore (i.e. the adsorbed phase density, $\rho_{\mathrm{a}}$), which are difficult to obtain in practice. Therefore, the concept of *excess* adsorption is used to quantify the amount adsorbed (A in Figure 2.5) (Sircar, 1999). Consider a system volume to be composed of two volumes: a solid volume and a pore volume denoted by $V_{\mathrm{s}}$ and $V_{\mathrm{p}}$ ($= V_{\mathrm{a}} + V_{\mathrm{b}}$), respectively, partitioned by the Gibbs dividing surface.

The excess adsorbed amount (in moles) is defined as:

$$\begin{aligned} n^{\mathrm{ex}} &= n^{\mathrm{t}} - \rho_{\mathrm{b}} V_{\mathrm{p}} \\ &= n^{\mathrm{t}} - \rho_{\mathrm{b}} (V_{\mathrm{a}} + V_{\mathrm{b}}) \\ &= n^{\mathrm{a}} - \rho_{\mathrm{b}} V_{\mathrm{a}} \end{aligned} \tag{2.2}$$

The term $\rho_{\mathrm{b}} V_{\mathrm{a}}$ is negligible at low pressure ($\rho_{\mathrm{b}} \ll \rho_{\mathrm{a}}$) leading to $n^{\mathrm{a}} \approx n^{\mathrm{ex}}$, which is the case for subcritical adsorption. However, the difference between $n^{\mathrm{ex}}$ and $n^{\mathrm{a}}$ becomes significant as $\rho_{\mathrm{b}}$ increases as in the case of supercritical adsorption (Myers and Monson, 2002). The right-hand side of the first expression in Equation 2.2 contains quantities that can be experimentally measured.

The measurement of $V_{\mathrm{p}}$, however, introduces a certain level of uncertainty in identifying the Gibbs dividing surface and has been a source of contention (Do and Do, 2007; Gumma and Talu, 2010; Brandani et al., 2016). Thus, *net* adsorption is defined (in moles) as below (Gumma and Talu, 2010; Pini, 2014):

$$\begin{aligned} n^{\mathrm{net}} &= n^{\mathrm{t}} - \rho_{\mathrm{b}} (V_{\mathrm{s}} + V_{\mathrm{a}} + V_{\mathrm{b}}) \\ &= n^{\mathrm{a}} - \rho_{\mathrm{b}} (V_{\mathrm{s}} + V_{\mathrm{a}}) \\ &= n^{\mathrm{ex}} - \rho_{\mathrm{b}} V_{\mathrm{s}} \end{aligned} \tag{2.3}$$

This measure of adsorption can be represented as A − D in Figure 2.5 and does not require the Gibbs dividing surface to be estimated. Additionally, it refers to the additional amount of fluid in the system as compared to the amount of only bulk fluid in the system with no adsorbent inside, providing a useful insight into the evaluation of the absorbent's storage capability (Pini, 2014). In other words, positive values of net adsorption indicate that the mass of the fluid in the chamber with the adsorbent is greater than that of the same fluid compressed in an empty container, whereas negative values of net adsorption indicate that simple compression of the fluid leads to higher storage.

Figure 2.6 shows absolute, excess, and net adsorption isotherms of $CO_2$ on ZIF-8 at 40 °C. Because $V_{\mathrm{b}} \leq V_{\mathrm{p}} \leq V$, it follows that $n^{\mathrm{net}} \leq n^{\mathrm{ex}} \leq n^{\mathrm{a}}$. As discussed, the excess and net adsorbed amounts are measurable quantities, but absolute quantities adsorbed must be estimated. For example, the absolute adsorption isotherm in Figure 2.6 has been estimated under the assumption that $V_{\mathrm{a}} \approx V_{\mathrm{p}}$. While this assumption may be valid for strictly microporous materials, such as ZIF-8, it is questionable for adsorption on materials with both micro- and mesoporosity, such as clay minerals.

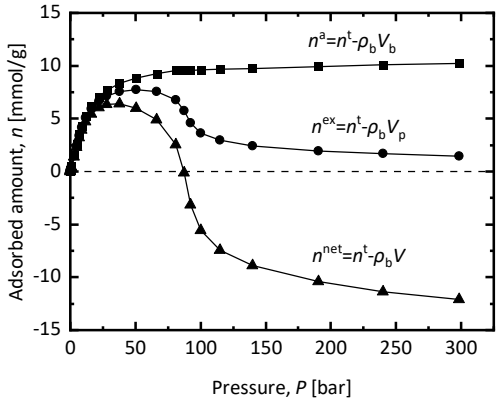



Figure 2.6: Absolute (squares), excess (circles), and net (triangles) adsorbed amounts of $CO_2$ on ZIF-8 as a function of pressure at 40 °C. The lines are to guide the eye.

Therefore, the interpretation and discussion of adsorption isotherms are limited to excess and net isotherms in this thesis, and any data analysis requiring the framework of absolute adsorption is made for pressures where it can be reasonably assumed that $n^{\mathrm{ex}} \approx n^{\mathrm{a}}$.

### 2.3.2 Adsorption on clay minerals

The same type of clay minerals (e.g. smectite, illite, etc.) may exhibit varying physical properties depending on multiple factors, including the sample origin, structural defects, nature of the interlayer cations, and method of sample preparation. For example, the specific surface area of powdered kaolinite (a 1:1 type non-swelling clay mineral) can range from $10\,\mathrm{m^2/g}$ to $40\,\mathrm{m^2/g}$ depending on its origin (English v. French) (Cases et al., 1986). Moreover, Rutherford et al. (1997) showed that the contribution made by micropores to the surface area and pore volume of montmorillonite can vary from 34 % to 87 % and 14 % to 66 %, respectively, depending on the nature of the exchanged cations. Thus, the clay minerals studied in this thesis are identified with their abbreviated IDs (e.g. SWy-2 for Na-rich montmorillonite) to indicate their places of origin and the nature of interlayer cations.

Experimental data of supercritical adsorption of $CO_2$ and $CH_4$ on clay minerals are relatively scarce compared to those on geological formations of which clay minerals are a major content. In most cases, $CO_2$ and $CH_4$ adsorption experiments have been conducted on coal, sandstone, and shales, and their gas sorption capacities have been correlated mostly to the organic content of these rocks (Krooss et al., 2002; Nuttall et al., 2005). Recent studies suggest that other factors, such as clay mineralogy, play a significant role in adsorption at supercritical conditions (Giesting et al.,

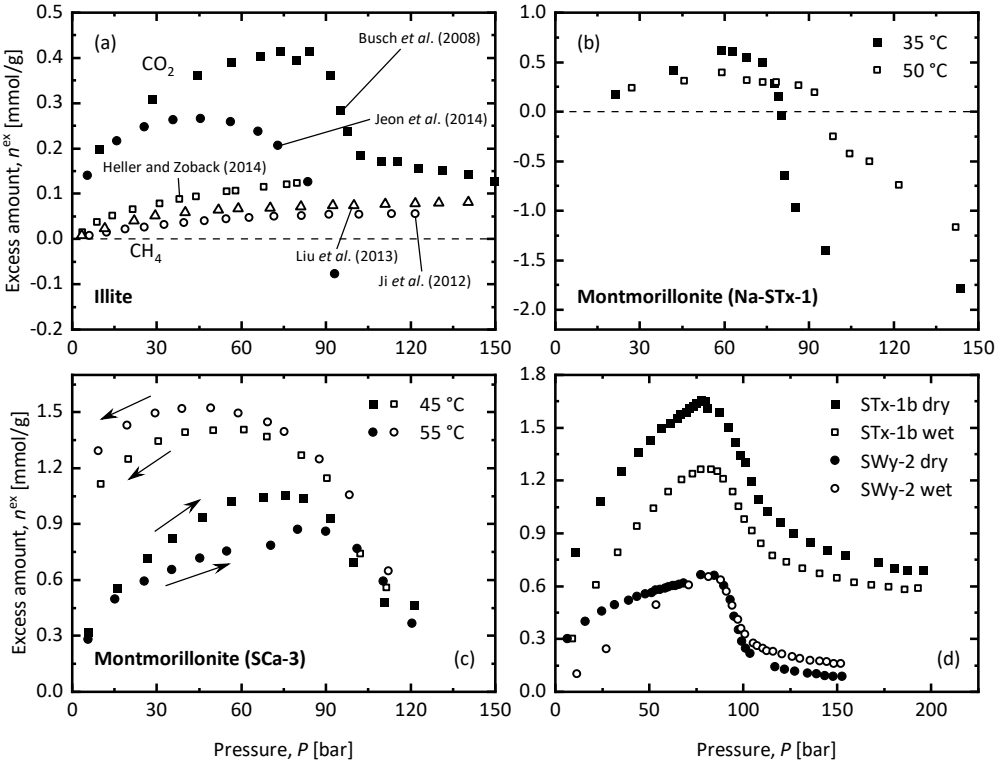



Figure 2.7: (a) Excess sorption isotherms of $CO_2$ (closed symbols, 45 °C) and $CH_4$ (open symbols, 30 °C to 40 °C) on illite (Busch et al., 2008; Ji et al., 2012; Liu et al., 2013; Heller and Zoback, 2014; Jeon et al., 2014). (b) Excess sorption isotherms of $CO_2$ on montmorillonite (STx-1) at 35 °C and 50 °C (Rother et al., 2013). (c) Excess adsorption and desorption isotherms of $CO_2$ on montmorillonite (SCa-3) at 45 °C and 55 °C (Jeon et al., 2014). (d) Excess sorption isotherms of $CO_2$ on montmorillonite (STx-1b - squares, SWy-2 - circles) under dry (closed symbols) and moisture-equilibrated (open symbols) conditions at 45 °C (Busch et al., 2008).

2012a; Ji et al., 2012; Zhong et al., 2016). For instance, Lu et al. (1995) found that shale samples with less than 1 % of organic content still adsorbed significant amounts of $CH_4$, and concluded that illite may be the main adsorbing mineral constituent of Devonian shales. In addition, Ross and Bustin (2009) found that the micropore structure of organic-lean shales is controlled by the clay fraction. Figure 2.7 provides a summary of the literature on high-pressure $CO_2$ and $CH_4$ excess adsorption data on various clay minerals. The summary is by no means a comprehensive review of the reported data in the literature, but rather focuses on a few observations that this thesis aims to address.

### Disagreement among literature data

Figure 2.7a shows the excess $CO_2$ (45 °C) and $CH_4$ (30 °C to 40 °C) isotherms on illite clay minerals (Busch et al., 2008; Ji et al., 2012; Liu et al., 2013; Heller and Zoback, 2014; Jeon et al., 2014).

While such temperature variation should not have a large effect on the experimental results, the interlaboratory comparison shows a significant disagreement for both $CO_2$ and $CH_4$. The comparison between the work by Busch et al. (2008) and Jeon et al. (2014) reveals that approximately 40 bar difference exists between the excess maxima locations, and the maximum amount of excess adsorption by Busch et al. (2008) is ∼0.41 mmol/g, which is appreciably greater than that reported by Jeon et al. (2014) (∼0.27 mmol/g) although the pure illite samples have been both sourced from the Clay Minerals Society (IMt-2). Similarly, the $CH_4$ isotherms in Figure 2.7a show a great level of disparity, which may be attributed to the different properties of illite clay minerals that arise from the varying sources of origin as previously discussed. The observation of scattered data sets is not only limited to illite, but also seen for other types of clay minerals (Busch et al., 2008; Ji et al., 2012; Liu et al., 2013; Rother et al., 2013; Fan et al., 2014; Jeon et al., 2014) as further addressed in Chapter 5.

**Negative excess adsorption**

The isotherms shown in Figure 2.7b show negative amounts of $CO_2$ excess adsorption for Na-saturated montmorillonite (STx-1), a phenomenon also seen for $CO_2$/illite in Figure 2.7a (Jeon et al., 2014) and other adsorbent materials (Rother et al., 2012). While Equation 2.2 does not restrict excess adsorption to be positive, possible explanations and arguments for/against the phenomenon are summarized here. Rother et al. (2013) attributes negative excess to interfacial fluid depletion caused by strong spatial confinement that limits multilayer adsorption. This interpretation is supported by molecular dynamics simulations of Lennard-Jones fluids that show interfacial fluid depletion at high bulk density for adsorbents with weak solid-fluid interaction energies (Oleinikova et al., 2006; Oleinikova and Brovchenko, 2008). However, Do et al. (2010) argued against the possibility of negative excess isotherms by pointing out a few assumptions made with the standard practice of using He to measure the void volume that may not be strictly true: 1) He is assumed to be non-adsorbing, 2) He and adsorbate access the same pores, and 3) void volume does not change with loading. The significant impact of the He measurements has been reported by Malbrunot et al. (1997), whose work showed that negative excess isotherms can be corrected by conducting He measurements at high temperature (to minimize the possibility of adsorption). Do et al. (2010) showed that incorrect estimation of the accessible volume even by 2 % can make a significant change in the values of excess adsorption. Therefore, it must be reminded that small uncertainties may lead to significantly erroneous interpretations and the errors caused

by He measurements must be taken into consideration for the calculation of excess adsorption under supercritical conditions.

### Sorption hysteresis

The term *adsorption* denotes a process, in which the amount of adsorbed phase on the solid surface increases, experimentally measured by increasing the pressure. Its counterpart process, *desorption*, is a process of decreasing the amount of adsorbed phase, experimentally measured by decreasing the pressure (Thommes et al., 2015). In this thesis, these two terms are often collectively referred to as *sorption*. When these two opposite sorption isotherm curves do not coincide, an open hysteresis loop is observed between them as in the cases of type IV(a) and V isotherms shown in Figure 2.3. These hysteresis loops are generally a representation of capillary condensation in mesopores, for which adsorption (condensation) and desorption (evaporation) mechanisms vary, and depend on the structural network of pores (Sing et al., 1985; Sangwichien and Aranovich, 2002; Thommes et al., 2015). While condensation and evaporation do not occur under supercritical conditions, hysteresis loops have also been observed for sorption of supercritical fluids (Jeon et al., 2014) as shown in Figure 2.7c for montmorillonite (SCa-3). These hysteresis loops have been attributed to structural changes undergone by the pores, such as swelling of layers in the case of clay minerals, during high-pressure adsorption. However, this interpretation is incomplete as hysteresis loops have also been seen for non-swelling clay minerals (Jeon et al., 2014). We address the presence (or lack thereof) of hysteresis loops under supercritical conditions in Chapter 6.

### Clay minerals with moisture content

Clay minerals exist with moisture content in their microstructures in natural environments, and it is apparent that the presence of water affects their sorption capacities. Figure 2.7d shows adsorption amounts of $CO_2$ on two montmorillonite samples (STx-1b and SWy-2), which both show decreased adsorbed amounts in the presence of water (Busch et al., 2008). Ross and Bustin (2009) made similar observations for adsorption of $CH_4$ on SWy-2 and IMt-2. However, recent studies experimentally demonstrated intercalation of $CO_2$ and $CH_4$ into the interlayers of swelling clay minerals under hydrated conditions (Giesting et al., 2012a; Ilton et al., 2012; Bowers et al., 2018), suggesting an increase in the sorption amount, in conflict with the former results. The work presented in Chapter 7 investigated the effect of water on the sorption capacities of clay minerals to address this disagreement in the literature.

# Chapter 3

# Experimental apparatus

## 3.1 Introduction

The initial stage of the Ph.D. program was devoted to setting up and testing a system capable of measuring adsorption at elevated pressure and temperature conditions. In this chapter, the details of the experimental setup, the working principles of the magnetic suspension balance, and the calibration measurements required to analyze collected data are discussed. The results obtained from partaking in the interlaboratory study (Nguyen et al., 2020) organized by the National Institute of Standards and Technology (NIST) are also discussed to demonstrate the measurement accuracy of the experimental setup.

## 3.2 Experimental setup

The experimental setup used to measure adsorption (increasing pressure) and desorption (decreasing pressure) of supercritical fluids is shown in Figure 3.1. The main element of the setup is the magnetic suspension balance (abbreviated as MSB hereafter, IsoSORP HPII) from Rubotherm (Bochum, Germany). The MSB is capable of measuring and recording weight data from vacuum to 350 bar up to 150 °C with a resolution of 10 µg. The measuring chamber was put under vacuum using a vacuum pump (RZ 2.5, Vacuubrand, Wertheim, Germany) for degassing and obtaining a reference state for weight measurements (see Section 3.2.1). The adsorbate fluids introduced to the measuring chamber were compressed and maintained using a syringe pump (Model 500D, Teledyne ISCO, California, USA) and a single-stage gas booster (DLE-75-1, Maximator, Nordhausen,

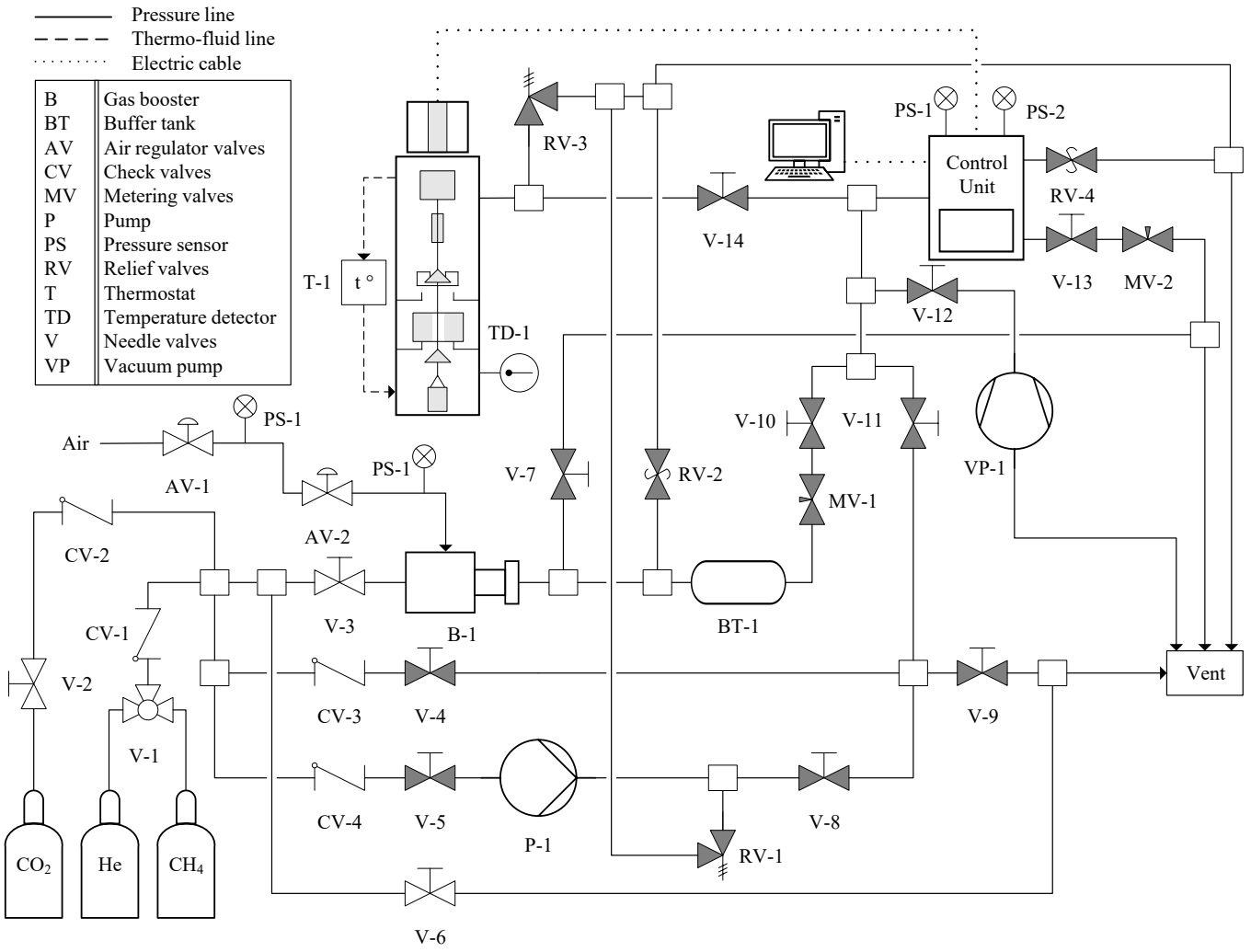



Figure 3.1: Schematic diagram of the experimental setup for high-pressure adsorption experiments. The grey-filled valves indicate high-pressure valves.

Germany) up to 300 bar. The gas booster used an inlet of dry air at 7 bar. The pressure of the system was measured by two pressure sensors (Keller PAA-33X, Winterhur, Switzerland) located inside the control unit (see Figure 3.1): one measures up to 40 bar and the other measures up to 700 bar both with 0.01 % full-scale accuracy. The MSB was enclosed with over 20 N · m torque and sealed with a gold-plated copper o-ring. The temperature inside the measuring chamber was controlled (±0.01 °C) using a liquid thermostat (Julabo F25, Seelbach, Germany) and measured by a resistance temperature detector located below the sample holder. The sample holder originally was a simple open top cylindrical basket, but it was later replaced with a new sample holder with a mesh lid to avoid the possibility of sample elutriation. To further avoid sample elutriation upon introduction of pressurized fluids, the fluids were first stored in a buffer tank (BT-1 in Figure 3.1) and gently introduced into the measuring chamber using a micro-dosing (metering) valve (MV-1 in Figure 3.1). The metering and needle valves were sourced from SITEC-Sieber Engineering AG (Zurich, Switzerland).

### 3.2.1 MSB operating principles

Figure 3.2 shows the main working components inside the measuring chamber and the three measuring positions of the MSB: zero point (ZP), first measuring point ($MP_1^*$), and second measuring point ($MP_2^*$). At ZP, the electromagnet engages with the permanent magnet. As the MSB moves

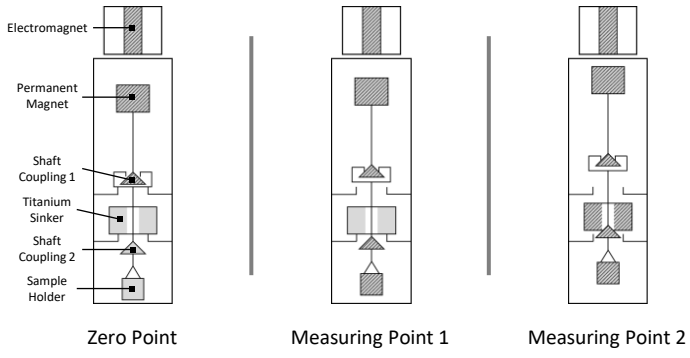



Figure 3.2: Schematic diagram of the magnetic suspension balance at three different measuring positions. The pattern-filled parts indicate suspended parts at each measuring positions.

to its next measuring position, $MP_1^*$, the sample holder is suspended by the first coupling system. At $MP_2^*$, the titanium sinker is suspended through the second coupling system. The difference between the two measuring positions and ZP can be considered as the calibrated weight values

measured at each measuring positions. The measured weight values at the two measuring positions discussed hereafter indicate these calibrated weight values and are denoted without asterisks (i.e. $\mathrm{MP}_1 = \mathrm{MP}_1^* - \mathrm{ZP}$ and $\mathrm{MP}_2 = \mathrm{MP}_2^* - \mathrm{ZP}$) and the weight values measured under vacuum are represented with a subscript 0. It then follows the apparent weight of the titanium sinker under a given experimental condition is equal to $m_{\mathrm{sk}} = \mathrm{MP}_2 - \mathrm{MP}_1$, while the mass of the titanium sinker is obtained in the same manner under vacuum $m_{\mathrm{sk},0} = \mathrm{MP}_{2,0} - \mathrm{MP}_{1,0}$.

The setup measures the quantity of excess adsorption. The excess adsorbed amount, $m^{\mathrm{ex}}$, is expressed using the following equation:

$$m^{\mathrm{ex}}(\rho, T) = \mathrm{MP}_1(\rho, T) - \mathrm{MP}_{1,0} + \rho_{\mathrm{b}} V_0 \tag{3.1}$$

where $\mathrm{MP}_1(\rho, T)$ and $\mathrm{MP}_{1,0}$ are the measured weights (sample and the suspended metal parts of the MSB) under the experimental condition and under vacuum, respectively; $\rho_{\mathrm{b}}$ is the adsorbate bulk density; and $V_0$ is the sum of the skeletal volume of the sample, $V_{\mathrm{s}}$, and that of the suspended metal parts, $V_{\mathrm{met}}$. It also follows that the value of $\mathrm{MP}_{1,0}$ is equal to the sum of the mass of the adsorbent sample, $m_{\mathrm{s}}$, and that of the suspended metal parts, $m_{\mathrm{met}}$. The term, $\rho_{\mathrm{b}} V_0$, in Equation 3.1 accounts for the buoyancy effect experienced by the sample and the suspended metal parts under the experimental condition. The value of $V_0$ is determined by using He as described in more detail in Section 3.2.2. The value of $V_{\mathrm{met}}$ can be obtained by introducing a fluid inside the measuring chamber without an adsorbent, in which case the right-hand side of Equation 3.1 becomes zero and $V_0$ becomes $V_{\mathrm{met}}$:

$$\mathrm{MP}_1(\rho, T) - \mathrm{MP}_{1,0} = -\rho_{\mathrm{b}} V_{\mathrm{met}} \tag{3.2}$$

The value of $V_{\mathrm{met}}$ is readily obtained from the negative value of the slope of the linear regression line fitted to $\mathrm{MP}_1(\rho, T) - \mathrm{MP}_{1,0}$ plotted against $\rho_{\mathrm{b}}$. In this thesis, $CO_2$ was introduced at incremental pressure conditions by both increasing and decreasing the pressure as shown in Figure 3.3. The value of $V_{\mathrm{met}}$ and $m_{\mathrm{met}}$ (equal to $\mathrm{MP}_{1,0}$ in Equation 3.2) of the original sample holder without a lid are $0.6666\,\mathrm{cm}^3$ and $5.2852\,\mathrm{g}$, respectively (the uncertainty values are not given as they are smaller than the decimal places in which these quantities are reported). The corresponding values of the sample holder with a lid are $1.4195\,\mathrm{cm}^3$ with an uncertainty value of $1 \times 10^{-4}\,\mathrm{cm}^3$ and $7.7045\,\mathrm{g}$ with an uncertainty value of $2 \times 10^{-5}\,\mathrm{g}$. With known values of $V_{\mathrm{met}}$ and $m_{\mathrm{met}}$, the skeletal density of adsorbents, $\rho_{\mathrm{sk}}$, can be readily determined from the skeletal volume of the sample, $V_{\mathrm{s}} = V_0 - V_{\mathrm{met}}$,

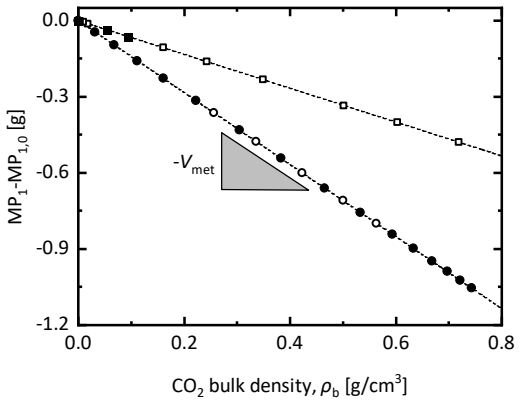



Figure 3.3: Normalized measured weight of the suspended metal parts including the sample holder plotted against the $CO_2$ bulk density at 60 °C (squares, the open top sample holder) and 80 °C (circles, the sample holder with a mesh lid). The closed symbols were measured by incrementally increasing the pressure and the open symbols were measured by decreasing the pressure. The negative value of the slope obtained from linear regression of the data points (dashed line) is equal to $V_{\mathrm{met}}$.

and the sample mass, $m_{\mathrm{s}}$. The value of $\rho_{\mathrm{b}}$ in Equation 3.1 and 3.2 is determined *in situ* through the buoyancy effect experienced by the titanium sinker with a known volume provided by the supplier $V_{\mathrm{sk}} = 4.363 \pm 0.002\,\mathrm{cm}^3$:

$$\rho_{\mathrm{b}} = \frac{m_{\mathrm{sk},0} - m_{\mathrm{sk}}}{V_{\mathrm{sk}}} = \frac{(\mathrm{MP}_{2,0} - \mathrm{MP}_{1,0}) - \big(\mathrm{MP}_2(\rho,T) - \mathrm{MP}_1(\rho,T)\big)}{V_{\mathrm{sk}}} \tag{3.3}$$

where $m_{\mathrm{sk},0}$ and $m_{\mathrm{sk}}$ are the mass of the titanium sinker under vacuum and under the experimental condition, respectively. The difference between the two represents the weight change of the sinker due to exerted buoyancy. Finally, the specific molar amount of excess adsorption, $n^{\mathrm{ex}}$, is reported in this study, which can be obtained from the following equation:

$$n^{\mathrm{ex}}(\rho,T) = \frac{\mathrm{MP}_1(\rho,T) - \mathrm{MP}_{1,0} + \rho_{\mathrm{b}} V_0}{M m_{\mathrm{s}}} \tag{3.4}$$

where $M$ is the adsorbate molar mass.

### 3.2.2 Helium gravimetry

The term $V_0$ in Equation 3.1 represents a key correction factor and, potentially, a major source of uncertainty especially when measuring supercritical adsorption on weakly adsorbing materials (Do et al., 2010; Brandani et al., 2016). As mentioned earlier, the value of $V_0$ is determined by introducing He into the measuring chamber under the assumption that it does not adsorb. The

lack of adsorption leads Equation 3.1 to become the following:

$$\mathrm{MP}_{1,\mathrm{He}}(\rho, T) = \mathrm{MP}_{1,0} - \rho_{\mathrm{He}} V_0 \tag{3.5}$$

The bulk density of He, $\rho_{\mathrm{He}}$, is again calculated using Equation 3.3. A linear fit to a plot of $\mathrm{MP}_{1,\mathrm{He}}$ against $\rho_{\mathrm{He}}$ results in a slope equal to the negative value of $V_0$ and an intercept equal to $\mathrm{MP}_{1,0}$ (equal to $m_{\mathrm{s}} + m_{\mathrm{met}}$). In this thesis, several pressure (or density) points were taken and the linear fits were applied using the method of weighted linear regression that takes into account the individual uncertainty values associated with each measured He point (see Appendix B). The He measurements were performed at high temperature (115 °C to 120 °C) to minimize the possibility of the small amounts of He adsorption reported previously (Malbrunot et al., 1997; Do and Do, 2007).

### 3.2.3 Data logging

The weight values at ZP, $\mathrm{MP}_1$, and $\mathrm{MP}_2$ were measured at each pressure point every 4 min to 5 min and logged (as well as the values of the temperature and pressure) by a proprietary software supplied by Rubotherm. The system was allowed to equilibrate for at least 60 min. The system was often allowed to run overnight (>12 h) in both adsorption and desorption mode to confirm that no significant amount of sorption takes place beyond the usual equilibration time. As an example of general validity, Figure 3.4 shows the measured values of pressure, temperature, $\mathrm{MP}_1$, and $\mathrm{MP}_2$ for $\mathrm{CO}_2$ adsorption on SWy-2 (Na-rich montmorillonite) at 50 °C over approximately 13 h. The average of the last five measurements was used to calculate the sorption amount at the given pressure and temperature conditions.

## 3.3 NIST interlaboratory study

The accuracy of the measurements produced by the experimental setup has been validated by participating in an interlaboratory study led by NIST. The study was initially performed to assess the comparability of high-pressure adsorption isotherms using reference materials, motivated by the poor reproducibility of isotherm measurements observed in the literature (Park et al., 2017; Han et al., 2019). The first interlaboratory study was conducted for $\mathrm{CO}_2$ adsorption on NIST reference material RM 8852 (ammonium ZSM-5 zeolite, hereafter referred to as ZSM-5, $\rho_{\mathrm{sk}} = 2.360\,\mathrm{g/cm^3}$)

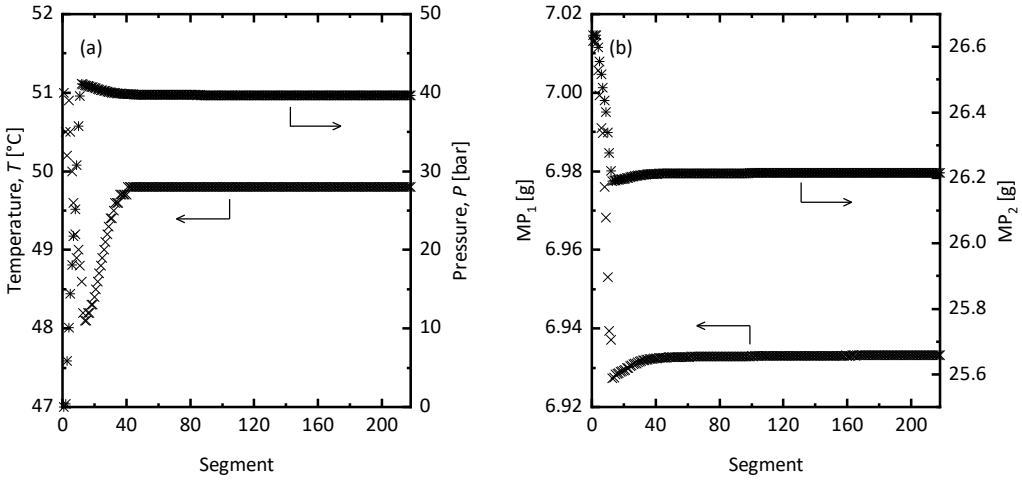



Figure 3.4: Measured values of (a) temperature (left axis) and pressure (right axis), and (b) corrected $MP_1$ ($MP_1 - ZP$, left axis) and corrected $MP_2$ ($MP_2 - ZP$, right axis) logged for approximately 13 h after pressurizing the measuring chamber with $CO_2$ up to 40 bar at 50 °C.

at 20 °C from 1 kPa up to 4.5 MPa (Nguyen et al., 2018). The second interlaboratory was conducted for $CH_4$ adsorption on another zeolite reference material at NIST RM 8850 (zeolite Y, $\rho_{sk} = 2.530\,g/cm^3$) at 25 °C up to 7.5 MPa (Nguyen et al., 2020). It was the second interlaboratory study that included the measurements produced by the setup described above. The agreement with the data sets submitted by other laboratories demonstrated the setup's capability of generating accurate sorption data.

### 3.3.1 Interlaboratory comparison

The interlaboratory study required the participants to produce $CO_2$ adsorption measurements that agree within the 95 % uncertainty interval of the reference isotherm derived from the first interlaboratory study. Such requirement allowed to validate the instrument's accuracy for sorption measurements of both $CO_2$ and $CH_4$. The reference isotherm was generated by fitting 13 data sets of $CO_2$ adsorption on ZSM-5 submitted by multiple laboratories to the following empirical equation:

$$n_{ref}^{ex}(P) = \frac{d_1}{\left(1 + \exp[\left(-\ln(P) + a_1\right)/b_1]\right)^{c_1}} \tag{3.6}$$

No physical significance is associated with Equation 3.6. The parameters for Equation 3.6 to describe $CO_2$ adsorption on ZSM-5 at 20 °C are $a_1 = -6.22$ (0.08), $b_1 = 1.97$ (0.01), $c_1 = 4.73$ (0.21), and $d_1 = 3.87$ (0.01), where the values in parentheses represent the standard error (Nguyen et al., 2018). The ZSM-5 sample, provided by NIST, was prepared as stipulated by the study

protocol (two aliquots degassed at 350 °C under continuous vacuum for 12 h). The excess adsorbed amounts of $CO_2$ were measured without the sample under the same experimental conditions to quantify the instrument error (hereafter referred to as a blank run). Figure 3.5 shows the amounts of excess adsorption for the blank run. The excess adsorbed amounts of $CO_2$ for the blank run do

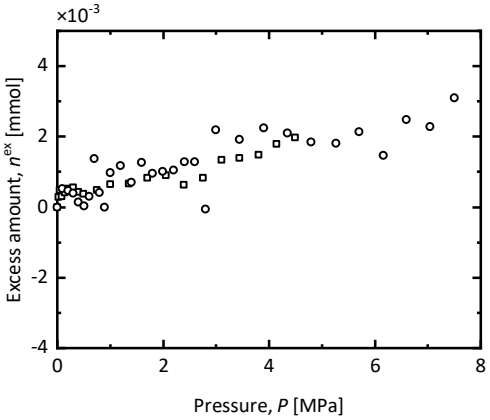



Figure 3.5: Excess adsorbed amounts of $CO_2$ (squares) at 20 °C up to 4.5 MPa and $CH_4$ (circles) at 25 °C up to 7.5 MPa measured with an empty basket.

not exceed 0.002 mmol, which is a negligible amount in comparison to the adsorption capacities of the adsorbents reported in this thesis. Figure 3.6a and its inset plot show that the measured amounts of excess adsorption of $CO_2$ on ZSM-5 are in excellent agreement with the reference isotherm with all the data points lying within the uncertainty interval (±0.075 mmol/g).

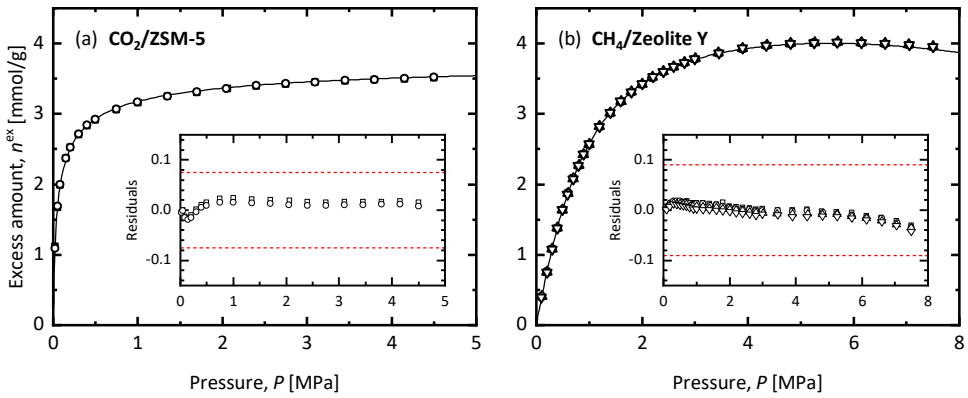



Figure 3.6: Excess adsorbed amount of (a) $CO_2$ on first (squares) and second (circles) aliquots of ZSM-5 at 20 °C up to 4.5 MPa and (b) $CH_4$ on first (run 1 - squares; run 2 - circles) and second (run 1 - upward triangles; run 2 - downward triangles) aliquots of zeolite Y at 25 °C up to 7.5 MPa. The solid lines represent the reference isotherms obtained from Equation 3.6 and 3.7. The inset plots show the residuals ($n^{ex}_{ref} - n^{ex}_{meas}$) against pressure with the upper and lower bounds shown in red dashed lines.

The $CH_4$ adsorption experiments on zeolite Y were conducted following the same sample prepa-

ration procedure as $CO_2$/ZSM-5. The blank run for $CH_4$ can be seen in Figure 3.5, which shows the maximum amount of excess adsorption is below 0.004 mmol. Such amount is again negligible to the adsorption capacities of the adsorbents reported in this thesis. Two sets of repeated $CH_4$ adsorption measurements were conducted on two aliquots of zeolite Y. The data sets submitted to NIST were used, with 20 data sets from other laboratories, to fit a reference isotherm using the following equation:

$$n_{\mathrm{ref}}^{\mathrm{ex}}(P) = \frac{a_2 P + b_2 P^2 + c_2 P^3}{\sqrt[d_2]{e + P^{d_2}}} \tag{3.7}$$

Again, no physical significance is associated with Equation 3.7. The parameters for Equation 3.7 to describe $CH_4$ adsorption on zeolite Y at 25 °C are $a_2 = 4.2040$ (0.0406), $b_2 = 0.0818$ (0.0100), $c_2 = -0.0132$ (0.0008), $d_2 = 1.4400$ (0.0146), and $e = 1.0700$ (0.0115), where the values in parentheses represent the uncertainty (Nguyen et al., 2020). Figure 3.6b and its inset show that all of the measured data points are within the uncertainty interval (±0.09 mmol/g) of the reference isotherm.

The values of $\rho_{\mathrm{b}}$ measured *in situ* by the balance from Equation 3.3 can be used as another validation of the instrument accuracy by comparing them to the values calculated using appropriate equations of state for each fluid (Span and Wagner (1996) for $CO_2$ and Setzmann and Wagner (1991) for $CH_4$) as shown in Figure 3.7. Figure 3.7 shows an excellent agreement between the

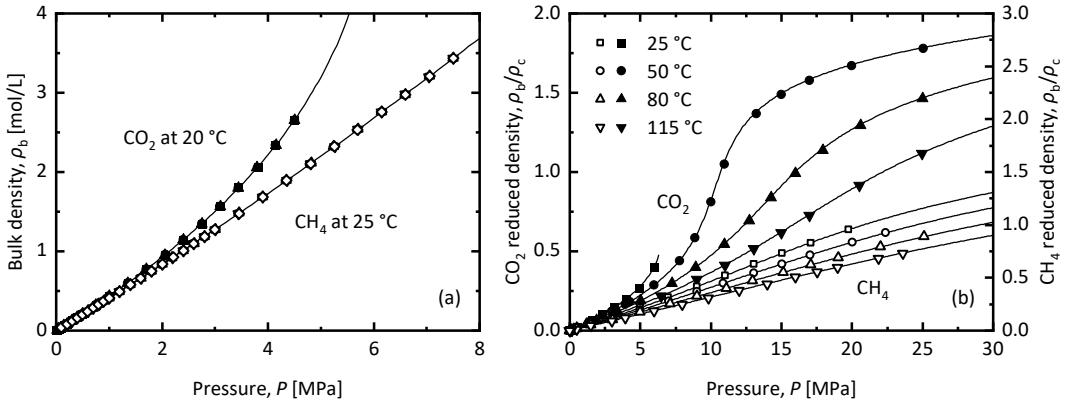



Figure 3.7: (a) Bulk density of $CO_2$ and $CH_4$ against pressure measured from the adsorption experiments shown in Figure 3.6 compared to the values calculated from the equations of state (solid lines) using REFPROP (Lemmon et al., 2018). (b) Reduced fluid density of $CO_2$ (closed symbols, left $y$-axis) and $CH_4$ (open symbols, right $y$-axis) against pressure measured from the sorption experiments on SWy-2 as another example of validation through density measurements up to 25 MPa.

measured and calculated values for both $CO_2$ and $CH_4$. The level of deviation observed from the measurements reported in this thesis was less than 0.5 % for $CO_2$ and 0.4 % for $CH_4$ on average

above 5 bar. Below 5 bar, the difference between the experimental and calculated densities was larger, as a result of uncertainties in the measured weights. However, the computed excess adsorbed amount is largely unaffected by this error, because the buoyancy correction term is negligible at these conditions.

## 3.4 Concluding remarks

A high-pressure system capable of measuring accurate sorption data has been commissioned and set up in the laboratory to measure excess sorption of supercritical $CO_2$ and $CH_4$ under elevated pressure and temperature conditions relevant to subsurface applications. A series of tests have been repeatedly and periodically conducted to ensure the system is reasonably leak-free and capable of producing consistent sorption data safely. In addition, the safety guidelines related to operating high pressure and flammable ($CH_4$) fluids have been documented thoroughly in the setup's standard operating protocol, which was followed for all measurements presented in succeeding chapters. The accuracy of the measurements produced by the setup has been demonstrated by comparing the sorption data on $CO_2$/ZSM-5 and $CH_4$/zeolite Y systems to the data sets measured by multiple laboratories through an interlaboratory study conducted by NIST. The data sets produced by the setup described in this chapter all fell within the uncertainty interval of the reference isotherms generated by fitting the data sets submitted by the study participants (Nguyen et al., 2018, 2020) with empirical equations. Validation of the measurement accuracy is especially important in light of the recent probe into the reproducibility of adsorption isotherms in the literature (Park et al., 2017; Han et al., 2019). Partaking in the NIST interlaboratory studies is part of the effort to present reproducible and reliable high-pressure sorption data following the criteria proposed by Sholl (2019), who suggested the steps below when presenting experimental data:

- Show error bars on the data.
- Tabulate the data in supporting information/supplementary materials.
- Show data from calibration and/or validation tests using standard materials.
- Report observational details of material synthesis and treatment.

In the following chapters, the sorption data are reported with error bars obtained from careful uncertainty analysis considering the propagation of experimental uncertainty associated with each

quantities needed to calculate the adsorbed amounts in Equation 3.4. As breifly discussed in this chapter, the uncertainty of $V_0$ is mainly responsible for the magnitude of the error bars of excess sorption data; therefore, the experimental details and validity of the He measurements to determine its value are discussed in great detail in Chapter 5. Lastly, the high-pressure $CO_2$ and $CH_4$ sorption data have been deposited to Imperial College London Data Repository and are also available in Supporting Information of the publications, in which the data have been previously published (Hwang et al., 2019; Hwang and Pini, 2019).

# Chapter 4

# Adsorption model: lattice density functional theory

## 4.1 Introduction

The experimental adsorption data in this thesis are described using a model based on the lattice density functional theory (LDFT), an application of the density functional theory based on statistical thermodynamics. In the LDFT model, each individual pore space is discretized into lattice sites that are either filled with a fluid molecule or vacant. The fluid molecules that occupy the lattice sites are governed by interaction energies that exist among neighboring molecules. The equations relating the local density of the lattice sites to the density of neighboring lattice sites have been derived by Ono and Kondo (1960) (consequently named Ono-Kondo lattice equations), and were later formalized by Aranovich and Donohue (1996) to describe confinement of supercritical fluids in three dimensional pores. Particular features of the LDFT model highlighted in this thesis are its i) consideration of the neighboring interactions that exist between fluid-fluid (adsorbate-adsorbate) and surface-fluid (adsorbent-adsorbate) molecules, and ii) incorporation of the porous information of the adsorbent materials in the form of discretized lattice pores. The latter is especially key towards understanding adsorption inside clay mineral nanopores, consisting of a wide range of micro- and mesopores. The semi-empirical models commonly employed in studies of adsorption on clay minerals, such as the Langmuir model (Ji et al., 2012; Liu et al., 2013) or the Dubinin-Radushkevich (DR) equation (Jeon et al., 2014), not only fail to account for this complex

porous structure, but also present limitations in their basic underlying assumptions when applied to subsurface systems studied in this thesis, e.g. the assumption of monolayer adsorption by the Langmuir model or the DR equation's invalidity to pressures above the gas saturation pressure (Aranovich and Donohue, 1995; Bi et al., 2016). On the other hand, molecular simulation tools, such as the grand canonical Monte Carlo (GCMC) simulations, represent much more rigorous and sophisticated methods that take into account the fluid-fluid and surface-fluid interaction potentials within clay nanopores, the size of which is freely chosen (Jin and Firoozabadi, 2013; Chen et al., 2016b). However, simulations of adsorption inside large pore systems are performed at the expense of longer computation time. Capable of modeling adsorption inside discretized pores of simple geometry by considering the adsorbate-adsorbate and adsorbent-adsorbate interactions, the LDFT model represents a significant departure from the conventional adsorption models while showing good agreement with the results of GCMC simulations (Hocker et al., 2003; Pang and Jin, 2019a,b). Furthermore, the broad applicability of the LDFT model is shown by its adoption to study various adsorption systems under a wide range of pressure and temperature conditions. While variations of the formalism by Aranovich and Donohue (1996) have been mainly used to model supercritical adsorption (Bénard and Chahine, 1997; Hocker et al., 2003; Gao et al., 2004; Ottiger et al., 2008b; Pini et al., 2010) of multiple adsorbate ($H_2$, $N_2$, $CO_2$, $CH_4$, etc.) and adsorbent (carbon, zeolite, coal, etc.) systems, its successful application to model adsorption in the subcritical region has also been demonstrated (Do and Do, 2002; Qajar et al., 2016); the resulting isotherms are characterized by multilayer adsorption accompanied by capillary condensation (Aranovich and Donohue, 2003). The simple and versatile nature of the model equations has been exploited to describe mixture (binary and ternary) adsorption (Ottiger et al., 2008b; Pini et al., 2010; Sudibandriyo et al., 2011) and to investigate the effect of pore geometry (Qajar et al., 2016; Ansari et al., 2020).

## 4.2 Model equations

In this section, the LDFT equations are derived for single-component adsorption on one-dimensional slit pores, the pore geometry most applicable to clay mineral pore structure. The derivation of the LDFT equations presented below has been taken mainly from Hocker et al. (2003), Ottiger et al. (2008b), and Pini et al. (2010). Consider a slit-like pore composed of two identical walls that are infinitely long and wide like shown in Figure 4.1. The distance between these two walls is defined as $w$ and can be divided into $J$ number of lattice layers. The number of lattice layers is simply expressed as the quotient of the size of the pore and the fluid molecule

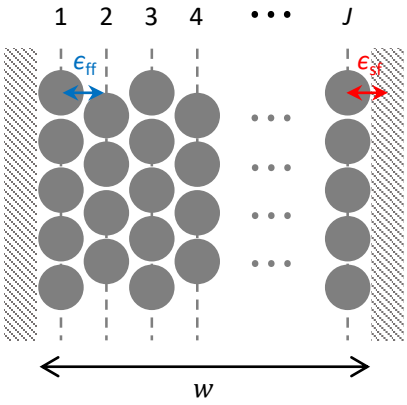



Figure 4.1: Graphical representation of fluid molecules occupying lattice sites in a one-dimensional pore space as adopted by the LDFT model. The red double-headed arrow indicates the interaction between the wall and adsorbate ($\epsilon_{sf}$) while the blue double-headed arrow indicates the interaction between neighboring adsorbates ($\epsilon_{ff}$). Graphic taken from (Pini et al., 2010)[a] with modifications.

[a]Reprinted by permission from Springer Customer Service GmbH: Springer Nature. Adsorption. R. Pini, S. Ottiger, G. Storti, M. Mazzotti, Copyright 2009

rounded to the nearest integer value. When fluid molecules are introduced in the pore space, each lattice site can either be filled with a fluid molecule or remain as a vacant site. A thermodynamic equilibrium state can then be assumed between the lattice and bulk sites and it is expressed as:

$$\mathrm{L_j} + \mathrm{B_v} \rightleftharpoons \mathrm{B_j} + \mathrm{L_v} \tag{4.1}$$

where $L$ and $B$ denote a lattice site and a bulk site, respectively, and the subscripts $j$ and $v$ denote occupied and vacant sites, respectively. In other words, the left-hand side of Equation 4.1 represents state I, where the lattice site is occupied by a fluid molecule and the bulk site is empty, and the right-hand side of Equation 4.1 represents state II, where the lattice site is empty and the fluid molecule occupies the bulk site. The following equation can be derived from the above equilibrium exchange:

$$\Delta H - T\Delta S = 0 \tag{4.2}$$

where $\Delta H$ and $\Delta S$ are the enthalpy and entropy change associated with the above equilibrium, respectively, and $T$ is the temperature. The micro-canonical formalism is applied to derive the following expression for $\Delta S$:

$$\Delta S = k \ln\left(\frac{W_{\mathrm{I}}}{W_{\mathrm{II}}}\right) \tag{4.3}$$

where $k$ is the Boltzmann's constant, and $W_{\mathrm{I}}$ and $W_{\mathrm{II}}$ are the number of configurations of the system in state I and II, respectively. Although it is difficult to define $W_{\mathrm{I}}$ and $W_{\mathrm{II}}$ separately, the ratio between the two can be estimated by defining the total number of configurations of the system, $W_{\mathrm{tot}}$. Moreover, the probability of having a molecule on the lattice site $j$ and the bulk site empty is assumed to be statistically independent of the probability of having a molecule on the bulk site while the lattice site $j$ is empty. The ratios are defined as:

$$\frac{W_{\mathrm{I}}}{W_{\mathrm{tot}}} = \theta_j(1-\theta_{\mathrm{b}}) \qquad \frac{W_{\mathrm{II}}}{W_{\mathrm{tot}}} = \theta_{\mathrm{b}}(1-\theta_j) \qquad \text{For site } j \tag{4.4}$$

where $\theta_j$ is the probability of having a fluid molecule on site $j$ and $\theta_{\mathrm{b}}$ is the probability of having a fluid molecule in the bulk. The probability in this context can be referred to as a degree of occupancy. The entropy term in Equation 4.2 can be defined by combining Equation 4.3 and 4.4:

$$\Delta S = k \ln\left(\frac{\theta_j(1-\theta_{\mathrm{b}})}{\theta_{\mathrm{b}}(1-\theta_j)}\right) \tag{4.5}$$

To obtain the enthalpy term, the total configurational energy is assumed to be given by the sum of simultaneous interactions among all pairs of molecules. For mathematical simplicity, (i) the pair interactions are restricted to those between nearest neighboring molecules only and (ii) only the molecules that are near the wall ($j = 1$ and $j = J$) interact with the surface. Then the enthalpy term in Equation 4.2 is defined as:

$$\Delta H = -\epsilon_{\mathrm{sf}} - \epsilon_{\mathrm{ff}}(z_2\theta_{j+1} + z_1\theta_j - z_0\theta_{\mathrm{b}}) \qquad \text{For} \quad j = 1 \tag{4.6}$$

$$\Delta H = -\epsilon_{\mathrm{ff}}(z_2\theta_{j-1} + z_2\theta_{j+1} + z_1\theta_j - z_0\theta_{\mathrm{b}}) \qquad \text{For} \quad 1 < j < J \tag{4.7}$$

$$\Delta H = -\epsilon_{\mathrm{sf}} - \epsilon_{\mathrm{ff}}(z_2\theta_{j-1} + z_1\theta_j - z_0\theta_{\mathrm{b}}) \qquad \text{For} \quad j = J \tag{4.8}$$

where $\epsilon_{\mathrm{sf}}$ and $\epsilon_{\mathrm{ff}}$ represent the surface-fluid interaction energy and fluid-fluid interaction energy, respectively, $z_0$ is the bulk coordination number, $z_1$ is the monolayer coordination number, and $z_2 = (z_0 - z_1)/2$ is the adjacent coordination layer number. The values of the coordination numbers represent the number of lattice cells in contact with the lattice cell under consideration in each respective phases; therefore, they depend on the chosen packing pattern of the molecules. The

final working equations for the lattice model are then defined as the following:

$$0 = \epsilon_{\mathrm{sf}} + \epsilon_{\mathrm{ff}}(z_2\theta_{j+1} + z_1\theta_j - z_0\theta_{\mathrm{b}}) + kT\ln\left(\frac{\theta_j(1-\theta_{\mathrm{b}})}{\theta_{\mathrm{b}}(1-\theta_j)}\right) \qquad \text{For} \quad j = 1 \tag{4.9}$$

$$0 = \epsilon_{\mathrm{ff}}(z_2\theta_{j-1} + z_2\theta_{j+1} + z_1\theta_j - z_0\theta_{\mathrm{b}}) + kT\ln\left(\frac{\theta_j(1-\theta_{\mathrm{b}})}{\theta_{\mathrm{b}}(1-\theta_j)}\right) \qquad \text{For} \quad 1 < j < J \tag{4.10}$$

$$0 = \epsilon_{\mathrm{sf}} + \epsilon_{\mathrm{ff}}(z_2\theta_{j-1} + z_1\theta_j - z_0\theta_{\mathrm{b}}) + kT\ln\left(\frac{\theta_j(1-\theta_{\mathrm{b}})}{\theta_{\mathrm{b}}(1-\theta_j)}\right) \qquad \text{For} \quad j = J \tag{4.11}$$

This set of non-linear equations can be solved simultaneously for $\theta_j$ for given values of $\theta_{\mathrm{b}}$, $\epsilon_{\mathrm{sf}}$, $\epsilon_{\mathrm{ff}}$, and $T$. Figure 4.2 shows the lattice occupancy profiles inside a pore space that can be obtained

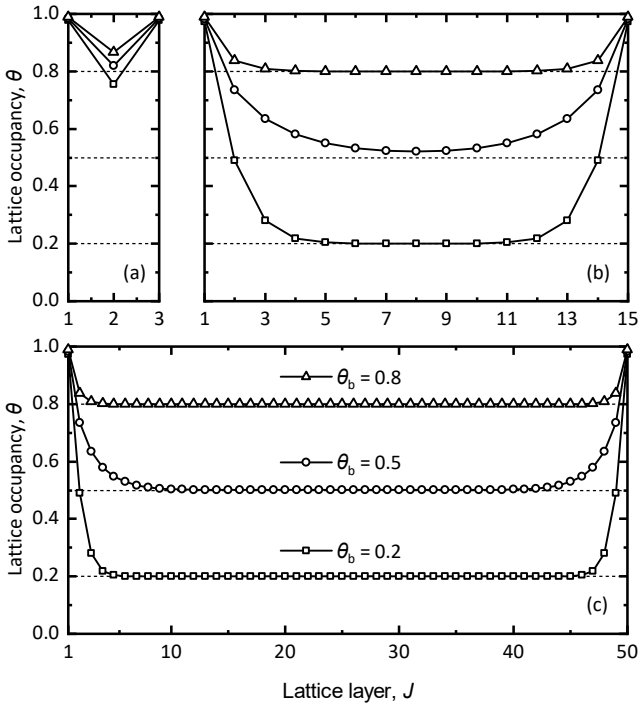



Figure 4.2: Lattice occupancy profiles of $CO_2$ at 50 °C inside pores with (a) 3, (b) 15, and (c) 50 layers each representing micropores, small mesopores, and large mesopores, respectively. The values of $\theta_{\mathrm{b}}$ are 0.2 (squares), 0.5 (circles), and 0.8 (upward triangles). The values of $\epsilon_{\mathrm{sf}}/k$ and $\epsilon_{\mathrm{ff}}/k$ used are −1100 K and −101.4 K, respectively. The value of $\epsilon_{\mathrm{sf}}$ was chosen arbitrarily.

upon solving the above set of non-linear equations. The distinct features of the lattice occupancy profiles shown for pores of varying sizes demonstrate that the LDFT model is capable of describing adsorption mechanisms that are pore-size dependent. The lattice occupancy profiles shown in Figure 4.2 can then be used to calculate the lattice excess adsorption, $\Gamma_{\mathrm{lat}}$, to produce a model

isotherm for a set of bulk occupancies, $\theta_b$:

$$\Gamma_{lat} = \sum_{j=1}^{J} \left(\theta_j - \theta_b\right) \tag{4.12}$$

### 4.2.1 Translation to physical units

Although the resulting isotherm of Equation 4.12 demonstrates the trend and shape of experimental isotherms, a direct comparison between them cannot be made without expressing the lattice model in physically meaningful units. Different correlations have been drawn to describe a real system using the LDFT model, but most studies have assumed a linear relationship between the lattice occupancy, $\theta$, and the fluid density, $\rho$ (or pressure). However, Hocker et al. (2003) derived an equation that relates the lattice occupancy to the fluid density based on three constraints. First, the lattice occupancy is zero at zero density. Second, the critical density of the fluid, $\rho_c$, corresponds to the lattice occupancy value of 0.5. This is a typical feature of Ising type lattice models based on the nearest-neighbor interactions and a fixed lattice spacing (Hill, 1987). Lastly, the maximum fluid density, $\rho_{max}$, must correspond to completely filled lattice occupancy (i.e. $\theta = 1$). Following these three boundary conditions, the following invertible function can be derived (Hocker et al., 2003):

$$\rho = \frac{\rho_{max}\rho_c\theta}{\rho_{max}(1-\theta) - \rho_c(1-2\theta)} \tag{4.13}$$

In this modeling approach, the pore-size distribution is discretized into $k$ number of pores of different sizes, each with a specific pore volume. The excess adsorption can be expressed as

$$n^{ex} = \sum_{k=1}^{K} \frac{v_{pore,k}}{J_k} \sum_{j=1}^{J_k} (\rho_j - \rho_b) \tag{4.14}$$

where $\rho_j$ is the density corresponding to the $j^{th}$ lattice site in a pore with $J_k$ lattice sites. The pore-size distribution of the adsorbent is discretized into $K$ number of pores of different sizes, each with a specific pore volume, $v_{pore,k}$, thus fulfilling the physical constraint:

$$v_{pore} = \sum_{k=1}^{K} v_{pore,k} \tag{4.15}$$

where $v_{pore}$ is the specific total pore volume of the adsorbent, which can be independently estimated from the analysis of low-pressure physisorption isotherms. The resulting molar excess adsorption in Equation 4.14 can be plotted against bulk density, which can also be expressed as pressure using

appropriate equations of state. Figure 4.3 shows the excess adsorption isotherms of $CO_2$ and $CH_4$ generated by the LDFT model at 50 °C. The isotherms of $CO_2$ and $CH_4$ produced by the LDFT

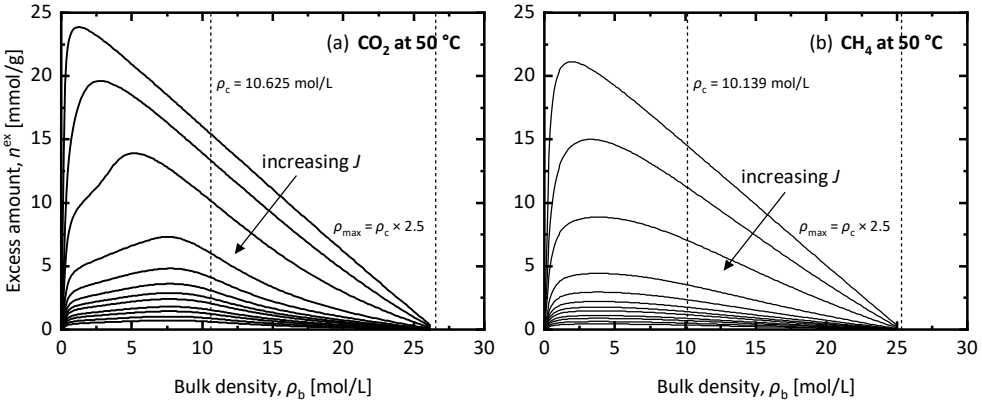



Figure 4.3: Excess adsorption isotherms of (a) $CO_2$ and (b) $CH_4$ at 50 °C produced by the LDFT model for multiple pores of varying number of lattice layers with $v_{\text{pore}} = 1\,\text{cm}^3/\text{g}$. The value of $\epsilon_{\text{sf}}/k$ is $-1100\,\text{K}$ and the values of $\epsilon_{\text{ff}}/k$ for $CO_2$ and $CH_4$ are $-101.4\,\text{K}$ and $-63.5\,\text{K}$, respectively. The value of $\rho_{\text{max}}$ is equal to $\rho_{\text{c}} \times 2.5$ where $n^{\text{ex}} = 0$. The dotted lines represent $\rho_{\text{c}}$ and $\rho_{\text{max}}$. The values of $\epsilon_{\text{sf}}$ and $\rho_{\text{max}}$ were chosen arbitrarily.

model show varying behaviors with increasing number of layers that are pore-size dependent. For instance, the isotherms of the smallest lattice pores ($J = 2$ and 3 representing pores with widths of 0.8 nm and 1.2 nm, respectively, in the case of $CO_2$ and $CH_4$) closely resemble those of microporous materials, such as zeolite 13X (Pini, 2014) or HKUST-1 (Moellmer et al., 2011), characterized by the steep increase in the adsorption amount in the low-density region. Interestingly, as the number of layers increases (into the mesopore region), distinguishable inflection points are observed in the $CO_2$ isotherms characteristic of near-critical conditions (Aranovich and Donohue, 1997; Pini et al., 2010) as $T/T_{\text{c}} = 1.06$ ($T_{\text{c}}$ is the fluid critical temperature) for $CO_2$ at 50 °C. The isotherms of $CH_4$, however, are little affected by the increasing number of layers due to the temperature being far from its critical condition at 50 °C ($T/T_{\text{c}} = 1.70$). The near-critical effect is better demonstrated in Figure 4.4 that shows the changing $CO_2$ and $CH_4$ isotherms as temperature moves further away from the critical point.

### 4.2.2 Parameter determination

The following parameters are required to solve the LDFT model: the fluid-fluid ($\epsilon_{\text{ff}}$) and surface-fluid ($\epsilon_{\text{sf}}$) interaction energies, the maximum fluid density ($\rho_{\text{max}}$, saturated lattice), and a suitable choice of pore-sizes. The number of lattice layers $J$ of a given slit pore is expressed as the ratio of

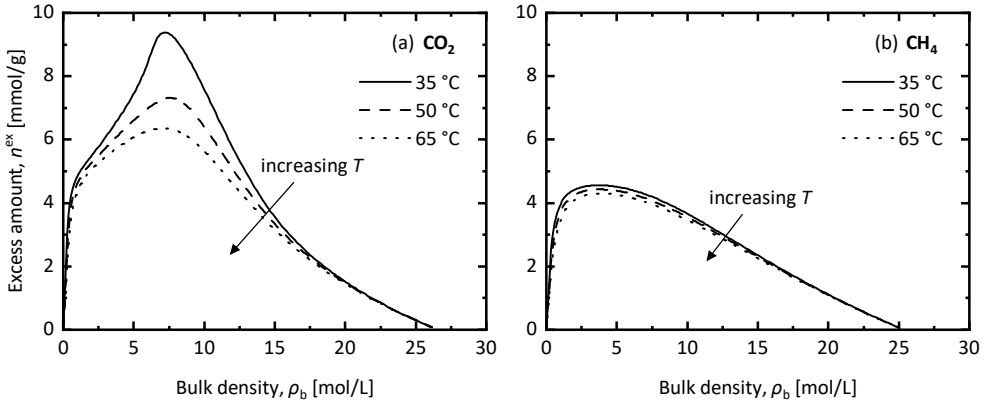



Figure 4.4: Excess adsorption isotherms of (a) $CO_2$ and (b) $CH_4$ at 35 °C, 50 °C and 65 °C produced by the LDFT model for a pore with 10 lattice layers with $v_{\text{pore}} = 1\,\text{cm}^3/\text{g}$. The same values of $\epsilon_{\text{sf}}/k$, $\epsilon_{\text{ff}}/k$, and $\rho_{\max}$ are used as Figure 4.3. The values of $T/T_{\text{c}}$ are 1.01, 1.06, and 1.11 for $CO_2$, respectively, and 1.62, 1.70, and 1.77 for $CH_4$, respectively.

the size of the pore (described by its width, $w$) and of the fluid molecule (described by the kinetic diameter) rounded to the nearest integer value. Because the lattice fluid is assumed to behave as a regular solution, $\epsilon_{\text{ff}}$ can be estimated from the critical temperature of the fluid (Hocker et al., 2003), i.e. $|\epsilon_{\text{ff}}| = 4kT_{\text{c}}/z_0$, where $z_0 = 12$ is the bulk coordination number of the closest hexagonal packing lattice pattern. The sizes of the lattice pores were determined from discretizing the pore-size distributions obtained from the analysis of low-pressure physisorption isotherms as demonstrated in Chapter 5 and Appendix C.

The remaining parameters, $\epsilon_{\text{sf}}$ and $\rho_{\max}$, were fitted to obtain the best agreement between the LDFT model results and experimental data. For the value of $\rho_{\max}$, bounds were given to constrain the values within physical limits. The upper limit was set by the number density of close-packed spheres, i.e. $\rho_{\max} = \sqrt{2}/(\sigma^3 N_{\text{A}})$, where $\sigma$ is the molecular kinetic diameter and $N_{\text{A}}$ is the Avogadro's number. For example, the value of $\sigma$ of $CO_2$ and $CH_4$ are 4.0 Å and 3.8 Å, respectively, given $\rho_{\max}$ of 36.7 mol/L and 42.8 mol/L, respectively. The lower limit of $\rho_{\max}$ was calculated from the reciprocal of the van der Waals co-volume, i.e. $b = P_{\text{c}}/(RT_{\text{c}})$ (Berberan-Santos et al., 2008), corresponding to 23.3 mol/L and 24.2 mol/L for $CO_2$ and $CH_4$, respectively. Due to the inability of a supercritical adsorbed phase to fill the entire pore space, the right-hand side of Equation 4.14 is multiplied by a temperature-dependent saturation factor, $c_{\text{sat}}$, which is defined as the ratio of the maximum volume occupied by the adsorbed fluid and the volume of the pore. Thus, the specific volume of the supercritical adsorbed phase at "saturation" is defined as $c_{\text{sat}} v_{\text{pore}}$. The physical interpretation of $c_{\text{sat}}$ is further discussed in Chapter 5 and 6.

## 4.3 Reduction to conventional adsorption models

The LDFT model can be reduced to a variety of adsorption isotherms (Aranovich and Donohue, 1997). The assumptions of monolayer adsorption (i.e. $\theta_j = \theta_b$ for $j \leq 2$) and no interactions among adsorbates (i.e. $\epsilon_{ff} = 0$) of the Langmuir model lead Equation 4.9 ($j = 1$) to be reduced to:

$$\theta_1 = \frac{\exp(-\epsilon_{sf}/kT)\theta_b}{1 + \big(\exp(-\epsilon_{sf}/kT) - 1\big)\theta_b} \tag{4.16}$$

where the term $\exp(-\epsilon_{sf}/kT)$ is defined as the dimensionless Henry constant, $\tilde{K}_H$. As the value of $(-\epsilon_{sf}/kT)$ is approximately 2 to 3 in this thesis, the value of $\tilde{K}_H \gg 1$. Therefore, Equation 4.16 can be written as:

$$\theta_1 \approx \frac{\tilde{K}_H\theta_b}{1 + \tilde{K}_H\theta_b} \tag{4.17}$$

which is analogous to the Langmuir model. It also follows that the LDFT model approaches the correct limiting behavior at low concentrations (i.e. $\theta_b$ approaching zero, and $\theta_1 \ll 1$), which is described by Henry's law:

$$\theta_1 = \tilde{K}_H\theta_b \tag{4.18}$$

From the relationship between $k$ and the gas constant, $R = kN_A$, it can be readily seen that:

$$\tilde{K}_H = \exp(-\epsilon_{sf}N_A/RT) = \exp(-\Delta u_0/RT) \tag{4.19}$$

where $\Delta u_0$ ($< 0$) is the change in internal energy of adsorption. Therefore, the surface-fluid interaction energy parameter, $\epsilon_{sf}$, provides another means to estimate the limiting differential enthalpy of adsorption from the following relation: $-\Delta h_0 = -\Delta u_0 + RT$ (Ruthven, 2000). The values of these adsorption metrics are compared to those extracted from the experimental isotherms as further discussed in Section 5.4.3 and 5.5.5.

## 4.4 Solution procedure

The set of non-linear equations of the LDFT model was solved using the function `lsqnonlin` in MATLAB. In this thesis, a hexagonal lattice packing pattern was used for supercritical fluids ($z_0 = 12$, $z_1 = 6$, and $z_2 = 3$). The maximum number of iterations and the termination tolerance were set to their default values (400 and $1 \times 10^{-6}$, respectively). The experimental data were used to fit the parameters of the LDFT model by minimizing the sum of the squared residuals, defined

as:

$$\Phi = \sum_{i=1}^{T} \sum_{j=1}^{N} \left( n_{\text{exp}}^{\text{ex}}(i,j) - n_{\text{calc}}^{\text{ex}}(i,j) \right)^2 \tag{4.20}$$

where $T$ is the total number of temperature conditions (isotherms), $N$ is the number of experimental points in the given isotherm, and $n_{\text{exp}}^{\text{ex}}$ and $n_{\text{calc}}^{\text{ex}}$ are the measured and calculated amounts of excess adsorption for each data point, respectively. The error minimization was done using the `fmincon` and `fminsearch` functions in MATLAB. These functions were allowed to run for a maximum of 200 iterations to find the error-minimizing parameters with the default value of termination tolerance equal to $1 \times 10^{-4}$. The set of fitted parameters are the surface-fluid interaction energy ($\epsilon_{\text{sf}}$, fluid-dependent), the maximum fluid density ($\rho_{\text{max}}$, fluid-dependent), and the saturation factor ($c_{\text{sat}}$, temperature-dependent).

## 4.5 Concluding remarks

The distinct features and advantages of the LDFT model have been presented in this chapter. In summary, the LDFT model has the following advantages:

- Has its concrete theoretical basis derived from statistical thermodynamics.
- Shows the correct limiting behavior as it reduces to Henry's Law at infinitely dilute concentrations, which is often not fulfilled for other commonly used adsorption models (e.g. DR equation (Aranovich and Donohue, 1995) or Freundlich equation (Ruthven, 2000)).
- Applies over a wide range of pressure and temperature conditions without being limited to certain adsorption mechanisms (e.g. monolayer v. multilayer adsorption).
- Provides estimates of the adsorbed phase properties inside pores of varying sizes.

In addition, the LDFT model also has a practical advantage of providing the results as excess adsorption, which allows direct comparison to the experimental isotherms, in contrast to the thermodynamic frameworks of conventional adsorption models that are based on absolute adsorption.

We conclude this chapter with reference to the following propositions made by Zuilhof et al. (2018) to improve the quality of presenting modeling work: i) clearly describe the approximations and limitations of the approach and ii) discuss the physical insights provided by the model and their relevance in understanding real world phenomena. The simplifying assumptions of the modeling

approach have been clearly stated in this chapter, such as the coarse-grained representation of pores as a finite set of discrete lattice sites and consideration of fluid-fluid interactions only between nearest neighbor molecules. We describe in this chapter the approximations of the input parameters, which is further reported in detail in the succeeding chapters. The parameters determined from the model are also assessed to ascertain that they are physically sensible and sound. For instance, theoretical limitations of fluid density were taken as upper and lower boundary conditions in estimating the value of the maximum adsorbate density. The model results are discussed in terms of their physical significance in the following chapters. Specifically, the saturation factor, $c_{\mathrm{sat}}$, is interpreted to account for the variability in the adsorbate packing density and its dependence on temperature is drawn in Chapter 5 and 6. Furthermore, the adsorption energetics are estimated from the surface-fluid interaction energies, $\epsilon_{\mathrm{sf}}$, which are validated by comparing to those obtained from the experimental isotherms.

# Chapter 5

# Workflow development: Na-rich montmorillonite

Reprinted (adapted) with permission from Junyoung Hwang, Lisa Joss, Ronny Pini. Measuring and modelling supercritical adsorption of $CO_2$ and $CH_4$ on montmorillonite source clay. *Microporous and Mesoporous Materials* 2019, 273, 107-121. Copyright 2018 Elsevier Inc.

## 5.1 Introduction

In this chapter, a workflow is presented that has been developed to comprehensively describe the adsorption characteristics and behaviors of clay minerals using a combined experimental and modeling approach. The modeling approach using the LDFT model takes into account the structural properties of clay minerals, namely the pore volume and pore-size distribution, determined from the conventional method of characterization using $N_2$ physisorption under cryogenic conditions. For this aim, the single-component adsorption and desorption of $CO_2$ and $CH_4$ have been measured in the temperature range of 25 °C to 115 °C up to 250 bar on dry Na-rich montmorillonite. The montmorillonite clay mineral has been chosen due to its relatively well-known properties and available high-pressure adsorption data in the literature compared to other types of clay minerals (Busch et al., 2008; Ji et al., 2012; Liu et al., 2013; Rother et al., 2013; Fan et al., 2014; Schaef et al., 2014). The results are presented and interpreted in terms of both net and excess adsorption isotherms, the uncertainties of which are carefully considered by identifying the main sources of

measurement uncertainty, such as the adsorbent skeletal volume. Key adsorption metrics, such as the Henry constants and enthalpy of adsorption, are extracted from the experimental measurements and compared to the results obtained from the LDFT model.

## 5.2 Materials

Na-rich montmorillonite (SWy-2) has been sourced from the Source Clays Repository of the Clay Minerals Society (Virginia, USA). The sample was ground manually to obtain particles smaller than 50 µm and aliquoted for low-pressure (Section 5.3.1) and high-pressure (Section 5.3.2) experiments. The pure gases used in this study were obtained from BOC (Surrey, UK) at purities of 99.9992 % for $N_2$, 99.995 % for $CO_2$, 99.5 % for $CH_4$, and 99.999 % for He.

## 5.3 Experimental methods

### 5.3.1 Low-pressure gas physisorption

The microscopic structural properties of SWy-2 were determined via low-pressure physisorption analysis, which was conducted using $N_2$ at 77 K in the pressure range of $8 \times 10^{-8}$ MPa to $1 \times 10^{-1}$ MPa measured using the 3Flex Surface Characterization Analyzer (Micromeritics, Georgia, USA). Prior to the experiment, the SWy-2 sample was degassed *ex situ* at 200 °C under vacuum for over 12 h and *in situ* at 120 °C for 4 h. The pore volume and the pore-size distribution of meso- and macropores (widths larger than 2 nm) were evaluated by the application of the Barrett-Joyner-Halenda (BJH) theory that accounts for the volume desorbed via both capillary evaporation (described by the Kelvin equation) and thinning of multilayers of adsorbed molecules in cylindrical pores (Barrett et al., 1951). To account for the characteristic geometry of pores formed by the arrangement of the platy clay particles, a modified version of this theory was applied in this study that assumes the formation of hemicylindrical menisci in slit pores (see Section 5.4.2) (Rouquerol et al., 2014). The obtained equations were applied to the desorption branch of the measured isotherm and by computing the thickness of adsorbed layers from the Harkins-Jura equation (Webb and Orr, 1997). The micropore volume (pore widths smaller than 2 nm) was quantified from the linearization of the Dubinin-Radushkevich (DR) equation (Dubinin and Radushkevich, 1947). The obtained estimate was compared to the total micropore

volume calculated by the Horvath-Kawazoe (HK) method for slit-like pore geometry (Horváth and Kawazoe, 1983) available through the Micromeritics software. Lastly, the specific surface area (SSA) of the sample was estimated using the linear form of the Brunauer-Emmett-Teller (BET) equation (see Appendix A) (Brunauer et al., 1938).

### 5.3.2 High-pressure sorption experiments

The high-pressure measurements were conducted in the pressure range of 0.2 bar to 250 bar at 25 °C, 50 °C, 80 °C and 115 °C using the experimental setup described in Chapter 3. The SWy-2 sample was degassed *ex situ* in an oven 200 °C for over 12 h and additionally *in situ* at 120 °C under vacuum for 4 h. The *in situ* degassing procedure was repeated between experiments that use different fluids (He, $CO_2$, and $CH_4$).

## 5.4 Modeling

The experimental adsorption data have been modeled using the LDFT described in Chapter 4. The pore volume and pore-size distribution of SWy-2 used as an input parameter for the LDFT model were obtained by applying the DR equation (Section 5.4.1) and BJH theory (Section 5.4.2), and the thermodynamic properties calculated from the LDFT model have been compared to the values determined by empirical methods described in Section 5.4.3.

### 5.4.1 DR equation for micropore volume

The DR equation describes the degree of micropore filling by the ratio between the adsorbed volume, $V_{\mathrm{a}}$, and micropore volume, $V_{\mathrm{micro}}$ using the following equation (Dubinin and Radushkevich, 1947; Kapoor et al., 1989):

$$\frac{V_{\mathrm{a}}}{V_{\mathrm{micro}}} = \exp\left[ -\left( \frac{RT}{\beta E} \ln \frac{P^{\mathrm{o}}}{P} \right)^2 \right] \tag{5.1}$$

where $P$ and $P^{\mathrm{o}}$ are the equilibrium and saturation pressures, respectively; $R$ is the universal gas constant; $T$ is the temperature; $\beta$ is the adsorbate affinity coefficient; and $E$ is the energy of

adsorption. The linear form of Equation 5.1 is the following:

$$\log(V_{\mathrm{a}}) = \log(V_{\mathrm{micro}}) - 2.303\left(\frac{RT}{\beta E}\right)^2 \log^2\left(\frac{P^{\mathrm{o}}}{P}\right) \tag{5.2}$$

The intercept of the linear region when $\log(V_{\mathrm{a}})$ is plotted against $\log^2(P^{\mathrm{o}}/P)$ can then be used to find the value of $V_{\mathrm{micro}}$. The molar liquid density of $N_2$ at 77 K and $10^5$ Pa equal to 28.8 mol/L was used to convert the measured volume (at $cm^3$/g STP).

### 5.4.2 Application of BJH theory to slit pores

The derivation of the BJH theory applied to slit pores is based on the formation of hemicylindrical menisci, which are formed between the two parallel walls of a slit pore and are characterized by a mean radius of curvature, or core width, $r_{\mathrm{k}}$ that can be related to the pore width, $w_{\mathrm{p}}$, by the following expression (Rouquerol et al., 2014):

$$w_{\mathrm{p}} = r_{\mathrm{k}} + 2t \tag{5.3}$$

where $t$ is the thickness of the adsorbed multilayer. The core volume, $V_{\mathrm{k}}$, removed due to capillary evaporation during the first desorption step is equal to the volume of the adsorbate ($N_2$ in this chapter), $V_{\mathrm{liq}}$, removed during the same step: $\Delta V_{\mathrm{k}}(1) = \Delta V_{\mathrm{liq}}(1)$. The core volume, $V_{\mathrm{k}}$, and the pore volume, $V_{\mathrm{p}}$, of the first group of slit pores can be related as:

$$V_{\mathrm{p}}(1) = \frac{\bar{w}_{\mathrm{p}}(1)}{\bar{r}_{\mathrm{k}}(1)} V_{\mathrm{k}}(1) \tag{5.4}$$

where $\bar{w}_{\mathrm{p}}(1)$ and $\bar{r}_{\mathrm{k}}(1)$ are the mean pore and core width of the first $P/P^{\mathrm{o}}$ increment, respectively. For any subsequent removal of $N_2$, the core volume is equal to the volume of nitrogen removed minus the volume removed due to thinning of the adsorbed multilayer: $\Delta V_{\mathrm{liq}} = \Delta V_{\mathrm{k}} + \Delta V_{\mathrm{wall}}$. Finally, the pore volume is defined as:

$$\Delta V_{\mathrm{p}} = \frac{\bar{w}_{\mathrm{p}}}{\bar{r}_{\mathrm{k}}}\left(\Delta V_{\mathrm{liq}} - \Delta V_{\mathrm{wall}}\right) \tag{5.5}$$

where $\Delta V_{\text{wall}}$ of desorption step $j$ is obtained from the following:

$$\Delta V_{\text{wall}} = \sum_{i=1}^{j-1} H \cdot L(\bar{w}_{\text{p},i} - 2t_j) - H \cdot L(\bar{w}_{\text{p},i} - 2t_{j-1}) \tag{5.6}$$

$$= \sum_{i=1}^{j-1} \frac{V_{\text{p},i}}{\bar{w}_{\text{p},i}} (2t_{j-1} - 2t_j) \tag{5.7}$$

where $H$ and $L$ are the height and length of the considered slit pore, respectively.

### 5.4.3 Henry constant and enthalpy of adsorption

The Henry constant is commonly regarded as one of the fundamental parameters that describes an adsorbate-adsorbent pair. Its accurate determination is required in the calculation of other relevant thermodynamic properties (e.g. enthalpy of adsorption) and provides a useful basis for assessing adsorption selectivity of a gas mixture. Accurate values of Henry constants are difficult to obtain from adsorption isotherms measured via a gravimetric technique due to the minuscule weight change produced by adsorption of gas at very low pressures (Myers, 2004b). The treatment of the adsorption isotherms with the virial equation represents a reliable approach to circumvent this challenge (Rouquerol et al., 2014). The virial equation can be written in the following form:

$$\ln(n^{\text{a}}/P) = K_0 + K_1 n^{\text{a}} + K_2 (n^{\text{a}})^2 + K_3 (n^{\text{a}})^3 + \cdots \tag{5.8}$$

where $n^{\text{a}}$ is the absolute amount adsorbed, $P$ is the pressure and $K_0$ to $K_3$ are the virial coefficients that are characteristic of the gas-solid system and temperature under consideration. We note that pressure has not been replaced by the fugacity in Equation 5.8, as the virial equation has been applied only up to moderate pressures in this thesis (i.e. up to ∼2 MPa to 5 MPa for $CO_2$ and ∼5 MPa to 8 MPa for $CH_4$ depending on the temperature). In this pressure regime, it is also safe to assume that $n^{\text{ex}} = n^{\text{a}}$. The Henry constant, $K_{\text{H}} = \exp(K_0)$, can be obtained from the zeroth-order virial coefficient, which can be conveniently estimated from the extrapolation to zero loadings of the linear portion of the virial isotherm when plotted as $\ln(n^{\text{a}}/P)$ versus $n^{\text{a}}$ (Ruthven, 1984).

The differential enthalpy of adsorption for a pure, perfect gas is defined by the following thermodynamic equation (Myers, 2002):

$$\Delta h = R \left[ \frac{\partial \ln(P)}{\partial (1/T)} \right]_n \tag{5.9}$$

In the limit of zero coverage, $n^{\text{ex}} = n^{\text{a}} = K_{\text{H}} P$ and the differential enthalpy of adsorption can thus

be directly found from the temperature dependence of the Henry constant:

$$\Delta h_0 = \lim_{P \to 0} \Delta h = -R \left[ \frac{\partial \ln(K_{\mathrm{H}})}{\partial (1/T)} \right]_n \tag{5.10}$$

If the zero-coverage enthalpy, $\Delta h_0$, is assumed to be independent of temperature (Ruthven, 1984), Equation 5.10 can be integrated to yield:

$$K_{\mathrm{H}} = K_{\mathrm{H}}^0 \exp(-\Delta h_0 / RT) \tag{5.11}$$

Accordingly, $\Delta h_0$ is the negative value of the slope of the linear fit obtained from plotting $\ln(K_{\mathrm{H}})$ against $1/T$ multiplied by the universal gas constant, $R$. The value of $\Delta h_0$ is negative due to the exothermic nature of adsorption, and it is common to refer to its absolute value as the isosteric heat (Myers, 2002).

## 5.5 Results

In this section, the results of the adsorption experiments of $N_2$, $CO_2$, and $CH_4$ on SWy-2 are presented together with the LDFT model fits to these isotherms (Sections 5.5.3 and 5.5.4). The construction of the experimental isotherms and the LDFT model relies heavily on the structural properties of SWy-2, such as its skeletal volume and pore-size distribution. These properties are discussed first (Section 5.5.1 and 5.5.2) and have been determined from the analysis of $N_2$ physisorption and He gravimetry experiments (results summarized in Table 5.1). Thermodynamic parameters (Henry constants and isosteric heat) that characterize the supercritical adsorption systems are presented in Section 5.5.5 using the virial equation of state and the van't Hoff equation.

### 5.5.1 $N_2$ physisorption isotherm

The $N_2$ adsorption isotherm acquired at 77 K up to $P/P^{\mathrm{o}} = 0.99$ is shown in Figure 5.1a. The isotherm is of type II with a hysteresis loop of type H3 according to the classification by Thommes et al. (2015). This hysteresis loop is indicative of slit-like pores of clay minerals formed by their non-rigid platy particles (Rouquerol et al., 2014). The increasing adsorbed amount as $P/P^{\mathrm{o}}$ reaches unity without a plateau indicates that SWy-2 contains both meso- and macropores (Kuila and

Table 5.1: Structural properties of the source Na-montmorillonite clay used in this study (SWy-2). [(a)]Data obtained from $N_2$ physisorption analysis. [(b)]BET surface area obtained by $N_2$ physisorption. [(c)]Lower and upper estimate by Deeds and Van Olphen (1961a) refer to pycnometry measurements and crystallographic data, respectively; He-gravimetry was applied in this study.

| Property | Value | Unit |
|---|---|---|
| **Specific pore volume**[(a)] | 0.0904 | $cm^3/g$ |
| Micropores – *DR method* | 0.0138 | $cm^3/g$ |
| Micropores – *HK method* | 0.0134 | $cm^3/g$ |
| Mesopores | 0.0720 | $cm^3/g$ |
| Macropores | 0.0099 | $cm^3/g$ |
| **Specific surface area**[(b)] | | |
| Van Olphen and Fripiat (1979) | $31.82 \pm 0.22$ | $m^2/g$ |
| Kuila and Prasad (2013) | $31.13 \pm 0.16$ | $m^2/g$ |
| Busch et al. (2008) | 28.0 | $m^2/g$ |
| This study | $32.02 \pm 0.19$ | $m^2/g$ |
| **Skeletal density**[(c)] | | |
| Deeds and Van Olphen (1961a) | $2.694 \pm 0.006$<br>$2.804 \pm 0.012$ | $g/cm^3$<br>$g/cm^3$ |
| This study | $2.709 \pm 0.006$ | $g/cm^3$ |

Prasad, 2013). In addition, the sharp increase in the adsorbed amount in the low-relative pressure range ($P/P^o < 0.01$) suggests that SWy-2 has a noticeable level of micropore filling as shown in the inset of Figure 5.1a. The micropore volume has been estimated using the linear form of the DR equation ($1.5 \times 10^{-4} < P/P^o < 0.05$), which gave a specific micropore volume of $0.0138\,cm^3/g$. This value agrees well with the micropore volume estimated by the HK method ($0.0134\,cm^3/g$). As discussed in Section 5.4.2, the pore volume and pore-size distribution of meso- and macropores of SWy-2 have been obtained by applying the BJH technique for slit-like pore geometry. The results are presented in Figure 5.2, in which each incremental pore volume associated with each interval reduction of $P/P^o$ is plotted against the average pore width, $w_p$. Figure 5.2 shows a major peak for small mesopores with a size between 2 nm to 3 nm, and an appreciable pore volume associated with larger meso- and macro-pores ($2\,nm < w_p < 80\,nm$). The latter amounts to $0.0766\,cm^3/g$; the sum of the micropore volume and the meso-/macro-pore volume is $v_{pore} = 0.0904\,cm^3/g$. The BET plot of the $N_2$ physisorption isotherm exhibited a linear region between $3.4 \times 10^{-2} < P/P^o < 0.23$. The obtained SSA of SWy-2 was $32.02 \pm 0.19\,m^2/g$, which shows a good agreement with the value reported by the Clay Minerals Society ($31.82 \pm 0.22\,m^2/g$) and estimates found in the literature, as shown in Table 5.1.

The LDFT model was applied to describe the $N_2$ adsorption isotherm as shown in Figure 5.1a. The modeling parameters were obtained by fitting the experimental desorption data to the LDFT model and are summarized in Table 5.2. As discussed in Chapter 4, the LDFT model simulates

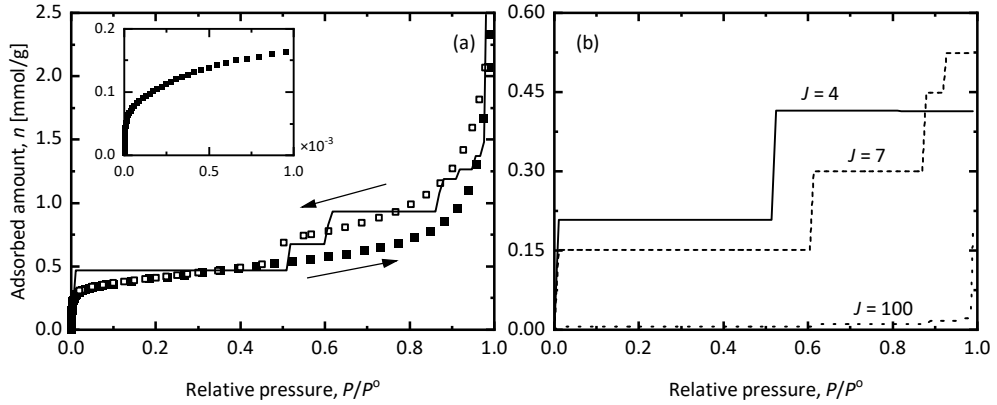



Figure 5.1: (a) $N_2$ physisorption isotherm taken at 77 K: experimental data (symbols) and LDFT model (solid line). The upward facing arrow indicates the adsorption (closed symbols) branch while the downward facing arrow indicates the desorption (open symbols) branch. The inset plot shows the adsorption points for which $P/P^o \leq 0.001$. (b) Contribution to the total amount of $N_2$ adsorption by pores of different sizes modeled by the LDFT: micropores ($J = 4$, solid line), small mesopores ($J = 7$, dashed line), and large mesopores ($J = 100$, dotted line).

Table 5.2: LDFT model parameters for the description of $CO_2$, $CH_4$ and $N_2$ adsorption on SWy-2 at sub- and supercritical conditions.

| Fluid | $\sigma$ | $\epsilon_{ff}/k$ | $\epsilon_{sf}/k$ | $\rho_{max}$ | $v_{pore}$ |
|---|---|---|---|---|---|
| | [Å] | [K] | [K] | [mol/L] | [$cm^3$/g] |
| $CO_2$ | 4.0 | -101.4 | -1151.8 | 26.8 | |
| $CH_4$ | 3.8 | -63.5 | -841.7 | 24.9 | 0.0904 |
| $N_2$ | 3.7 | -42.1 | -407.5 | 28.8 | |

adsorption inside pores of different sizes separately. To do so, the pore-size distribution and pore volumes of SWy-2 obtained from the BJH theory and the DR equation were discretized into pores with corresponding lattice pore widths each with its respective pore volume as shown in Figure 5.2. In particular, the micropores have been represented by a pore with 4 layers (i.e. $J = 4$); the characteristic peak ($2\,\text{nm} < w_p \leq 3\,\text{nm}$) in Figure 5.2 was associated to a mesopore with 7 layers, while mesopores in the range of $3\,\text{nm} < w_p \leq 10\,\text{nm}$ were grouped into a single pore with $J = 17$. The remaining mesopores and macropores were given a number of layers equal to the following: $J = 34$, 46, 65, 100, and 180. These model pores were equally applied to $N_2$, $CO_2$, and $CH_4$ because of their similar molecular diameters: 3.7 Å ($N_2$), 4.0 Å ($CO_2$), and 3.8 Å ($CH_4$) (Reid et al., 1987; Hirschfelder et al., 1954). It can be seen that the model captures the general shape of the $N_2$ isotherm; the characteristic stair-like shape of the model isotherm is the direct manifestation of the condensation process in a lattice structure characterized by a discrete number of layers. Nevertheless, the model predicts the occurrence of condensation below

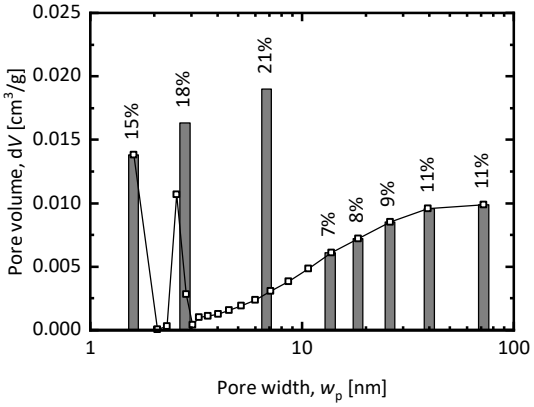



Figure 5.2: Incremental (symbols) and discretized (bars) pore volume plotted against the average pore width. Discretized pore-size distribution used for the LDFT model is labeled with the respective pore volume percentage for each pore. The average pore widths are translated to lattice model pores with given numbers of layers ($J = 4, 7, 17, 34, 46, 65, 100$, and 180).

the saturation pressure inside confined spaces, in agreement with other models that describe such fluid behaviors (e.g. the Kelvin equation). In particular, it can be seen in Figure 5.1b that the micropores are filled, or the maximum adsorbed amount is reached, at $P/P^{\mathrm{o}} \approx 0.4$, while larger pressures are needed to reach saturation in the mesopores ($P/P^{\mathrm{o}} \approx 0.9$). The mesopores also demonstrate a gradual increase towards the saturation pressure showing a shape that is analogous to type IV isotherm (Thommes et al., 2015). The macropores show almost no adsorption until $P/P^{\mathrm{o}}$ approaches the saturation pressure, where condensation results in a sharp increase in the adsorbed amount. The obtained estimate of $\Delta u_0^{\mathrm{LDFT}} = \epsilon_{\mathrm{sf}} N_{\mathrm{A}} = -3.4\,\mathrm{kJ/mol}$ is expectedly smaller than estimates for $N_2$ adsorption on zeolite 5A beads ($\Delta u_0 \approx -21\,\mathrm{kJ/mol}$) reported by Ruthven and Xu (1993), and much closer to the latent heat of vaporization of $N_2$ at 77 K, i.e. $-\Delta h_0^{\mathrm{LDFT}} = -\Delta u_0^{\mathrm{LDFT}} + RT = 4\,\mathrm{kJ/mol} \approx -\Delta h_{\mathrm{vap}} = 5.6\,\mathrm{kJ/mol}$ (Lemmon et al., 1998).

### 5.5.2 Skeletal volume

As discussed in Section 3.2.2, the skeletal volume and mass of SWy-2 are obtained from high-pressure He gravimetry. Figure 5.3 shows the values of $MP_1$ plotted against the He density for two sets of measurements: a set taken prior to the $CO_2$ measurements and another taken after the $CO_2$ measurements (prior to the $CH_4$ measurements). These two sets of He measurements showed a slight shift in the values of $MP_1$, which may be attributed to a small amount of $CO_2$ molecules that were not completely removed during the intermediate degassing step. Despite this shift, the slopes of the linear fits to these sets differed only by 0.3 %, which is within the uncertainty values of

each slope. Therefore, all of the experimental data from two sets of measurements were taken into account to determine the skeletal volume and sample weight of SWy-2 with a weight correction to the second set of measurements to account for the shift in $MP_1$.

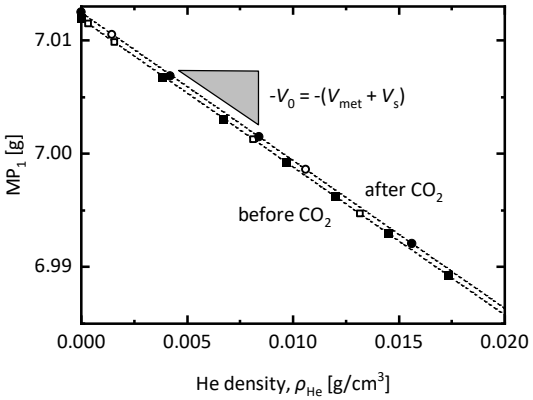



Figure 5.3: Measured weight of the suspended metal parts (including the sample holder) and the SWy-2 sample plotted against the He bulk density at 115 °C before (squares) and after (circles) the high-pressure $CO_2$ sorption experiments. The closed symbols were measured by incrementally increasing the pressure up to 130 bar and the open symbols were measured by decreasing the pressure. The negative values of the slope obtained from the linear regression of the data points (dashed lines) are equal to $V_0 = V_{\mathrm{met}} + V_{\mathrm{s}}$.

The resulting values of $V_0$ and $m_{\mathrm{s}}$ of SWy-2 are $1.304 \pm 0.001\,\mathrm{cm}^3$ and 1.727 g (negligible uncertainty), respectively. The value of $\rho_{\mathrm{sk}}$ of SWy-2 was then calculated to be $2.709 \pm 0.005\,\mathrm{g/cm}^3$ from the known value of $V_{\mathrm{met}}$ ($0.6666\,\mathrm{cm}^3$) obtained from the measurements with $CO_2$ and an empty sample holder (see Section 3.2.1). This value of $\rho_{\mathrm{sk}}$ compares well with the apparent density of $2.694\,\mathrm{g/cm}^3$ reported for sodium Wyoming bentonite determined via pycnometry with hydrocarbon liquids (Deeds and Van Olphen, 1961a). Notably, both values are well below the crystallography density of montmorillonite ($\sim$2.8 $\mathrm{g/cm}^3$ (Deeds and Van Olphen, 1961a)), suggesting that a fraction of the void space (possibly including the interlayer space) is inaccessible to He. This result is consistent with observations from cryogenic physisorption analysis (Section 5.5.1), where an *apparent* SSA ($\sim$30 $\mathrm{m}^2/\mathrm{g}$) was found that is significantly smaller than its counterpart obtained from crystallographic considerations ($\sim$800 $\mathrm{m}^2/\mathrm{g}$ (Mooney et al., 1952a)). The agreement between the value of $\rho_{\mathrm{sk}}$ obtained from the He measurements and that determined from independent pycnometric density measurements supports the reliability of the skeletal volume estimated via this method. This is key, because this parameter considerably affects the estimation of the excess adsorbed amount at elevated bulk densities. For example, an increase in the value of $V_0$ by 1 % in this study would increase the amount of $CO_2$ excess adsorption at 50 °C by 5 % at 40 bar and by 139 % at 250 bar. The importance and limitations of determining the correct value of $V_0$ using

He has been discussed in previous studies (De Weireld et al., 1999; Sircar, 2001; Dreisbach et al., 2002a). However, its effect on the measurement uncertainty at high pressure for weakly adsorbing materials and the associated error bars are rarely presented in the literature. The experimental approach adopted in this study that utilizes repeated sets of multiple He measurements within a wide range of pressure proved to be an apt method, as it introduces an acceptable uncertainty in the measured excess adsorbed amount.

### 5.5.3 Supercritical adsorption of $CO_2$ and $CH_4$: experiments

The adsorption of $CO_2$ and $CH_4$ was measured at 25 °C, 50 °C, 80 °C and 115 °C up to 250 bar. Figure 5.4 shows the measured net adsorption of $CO_2$ and $CH_4$ as a function of the bulk density at

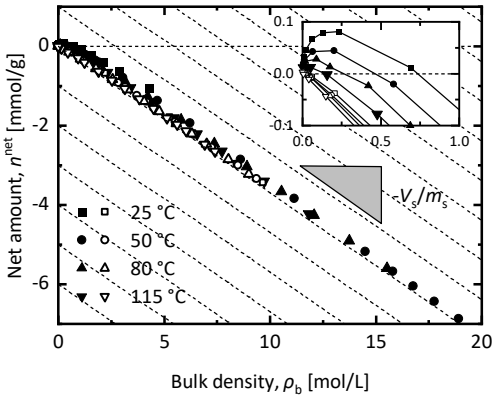



Figure 5.4: Net adsorption of $CO_2$ (closed symbols) and $CH_4$ (open symbols) on SWy-2 at 25 °C to 115 °C up to 250 bar. The dashed lines represent the slope equal to $-V_s/m_s$. The inset plot shows the net adsorbed amount below 1 mol/L (the solid lines are added to guide the eye).

each temperature investigated. The amount of net adsorption can be calculated from the following:

$$n^{\mathrm{net}}(\rho, T) = \frac{\mathrm{MP}_1(\rho, T) - \mathrm{MP}_{1,0} + \rho_{\mathrm{b}} V_{\mathrm{met}}}{M m_{\mathrm{s}}} \tag{5.12}$$

It can be seen that this measure of adsorption is negative for a large portion of the isotherm and that positive values are observed only up to small values of the bulk density (<0.7 mol/L for $CO_2$ and <0.03 mol/L for $CH_4$, as shown in the inset of the figure). Negative values of the net adsorbed amount are expected when the loss in storage volume introduced by the presence of the solid material is no longer compensated by the gain in storage capacity produced by gas adsorption. For dry SWy-2, this point is reached at low bulk density values relative to those observed for measurements with commercial adsorbent, such as zeolite 13X (10 mol/L to 11 mol/L) (Pini, 2014),

reflecting the modest adsorption capacity of clay minerals per unit mass. As shown in the inset of the figure, the crossing point moves to larger bulk density values as temperature is decreased, due to corresponding increase in adsorption. As an additional verification, dashed lines are also shown in the figure with a slope corresponding to the independently measured specific skeletal volume of the clay sample ($-V_s/m_s$). We observe that the experimental isotherms outline a linear region at large densities with a slope that is at least as large as the value computed from the skeletal volume, highlighting the small contribution introduced by the volume occupied by the adsorbed phase (the slope of the isotherm should approach the value $-(V_s + V_a)/m_s$ at saturation).

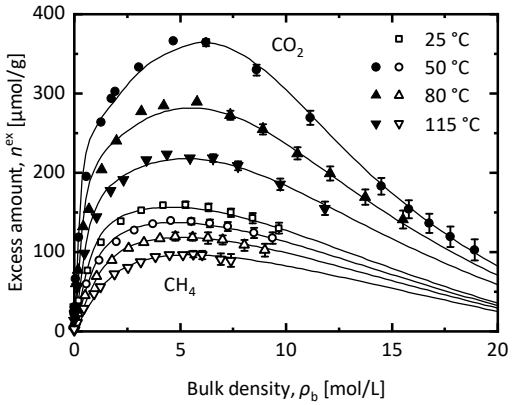



Figure 5.5: Excess sorption of supercritical $CO_2$ (closed symbols) and $CH_4$ (open symbols) on SWy-2 at 25 °C to 115 °C up to 250 bar. The symbols represent experimental data while the solid lines represent the LDFT model results at each temperature.

The experimental excess adsorption isotherms are shown in Figure 5.5, where the excess adsorbed amount is plotted against the bulk fluid density together with the LDFT model results. To confine the comparison between the experimental results and the LDFT model to supercritical adsorption, the adsorption data of $CO_2$ at 25 °C have been excluded from Figure 5.5. Moreover, no distinction is made in the figure among data measured in adsorption and desorption mode, due to the lack of observation of any hysteresis effect. Both $CO_2$ and $CH_4$ isotherms show the amount of excess adsorption increasing monotonically with pressure before reaching maximum values. After passing through the maximum points, the isotherms gradually decrease with increasing pressure. The maxima occur around $\rho_b = 5$ mol/L for $CO_2$ at all temperatures, which corresponds to a sharp increase in the bulk density; the sharper increase in the bulk density at 50 °C ($T/T_c = 1.06$) leads to a more pronounced maximum peak at the same temperature. Interestingly, the characteristic shape of the $CO_2$ isotherms at elevated densities ($\rho_b > 10$ mol/L) differs from the characteristic linear decrease observed with microporous solids (Pini, 2014) and is more reminiscent of the curved

behavior observed with mesoporous materials (Di Giovanni et al., 2001). Similar features are observed for the isotherms measured with $CH_4$; however, the effects are much weaker in this case, as the experimental temperatures of $CH_4$ in this study are farther from its critical temperature ($T/T_c = 1.5 - 2.0$).

### 5.5.4 Supercritical adsorption of $CO_2$ and $CH_4$: modeling

The LDFT model results are also shown in Figure 5.5, where it can be seen that this model captures the experimental observations very well over the entire pressure range and at each temperature (the values of the objective function are $\Phi = 1.13 \times 10^4\,\mu mol^2/g^2$ and $\Phi = 1.71 \times 10^3\,\mu mol^2/g^2$ for $CO_2$ and $CH_4$, respectively). The parameters used in the model are summarized in Table 5.2. Among them, the surface-fluid interaction energy ($\epsilon_{sf}$) and the density of the saturated lattice ($\rho_{max}$) were fitted to obtain the best agreement between the LDFT model and the experimental data. We note that for a given fluid, both parameters are independent of temperature. From the values of $\epsilon_{sf}$ for $CO_2$ ($\epsilon_{sf}/k = -1151.8\,K$) and $CH_4$ ($\epsilon_{sf}/k = -841.7\,K$), estimates for the zero coverage differential enthalpy of adsorption are obtained that take values of $\Delta h_0^{LDFT} \approx -12.5\,kJ/mol$ ($CO_2$) and $\Delta h_0^{LDFT} \approx -9.8\,kJ/mol$ ($CH_4$). These values are just above the latent heat of vaporization of the two gases (i.e. $\Delta h_{vap} = -10.3\,kJ/mol$ for $CO_2$ at $273.15\,K$ and $\Delta h_{vap} = -8.2\,kJ/mol$ for $CH_4$ at $112\,K$ (Lemmon et al., 1998)), in agreement with the common perception that for physisorption, $\Delta h_0/\Delta h_{vap} < 1.5 - 2$ (Ruthven, 2000). The fact that the values obtained here are at the lower end of the expected range is not surprising given that clays are weakly sorbing materials and that the parameter $\epsilon_{sf}$ describes solely the interactions between the surface and the first adsorbed layer. Notably, the stronger affinity observed in the adsorbed amounts towards $CO_2$ as compared to $CH_4$ is also reflected in the relative values of the surface-fluid interaction energy $\epsilon_{sf,CO_2}/\epsilon_{sf,CH_4} \approx 1.4$.

The resulting values of $\rho_{max}$ are $26.8\,mol/L$ for $CO_2$ ($\rho_{max}/\rho_c = 2.52$) and $24.8\,mol/L$ for $CH_4$ ($\rho_{max}/\rho_c = 2.45$). These estimates are closer to the inverse of the van der Waals co-volume than the number density of close-packed spheres. In particular, both values are comparable to results obtained on a mesoporous silica ($\rho_{max}/\rho_c = 2.5$) and significantly smaller than those obtained on microporous zeolite ($\rho_{max}/\rho_c = 3.45$) with $CO_2$ (Hocker et al., 2003), confirming that the degree of packing of the adsorbed molecules is strongly affected by the pore structure of the adsorbent material. The similarity of the values obtained for $CO_2$ and $CH_4$ supports this observation, because the two molecules share comparable kinetic diameters. We also note that a constant value of $\rho_{max}$ has been used for each fluid, which corresponds to a complete filling of the lattice, irrespective of

temperature. Accordingly, all isotherms in Figure 5.5 for a given fluid converge to a single value, corresponding to the point where the density of the adsorbed phase is equal to that of the bulk phase. This characteristic behavior of excess adsorption isotherms is also seen for other fluids adsorbing onto various porous materials, such as silica gel, HKUST-1, and activated carbon (Di Giovanni et al., 2001; Ustinov et al., 2002; Moellmer et al., 2011; Schell et al., 2012).

### 5.5.5 Henry constants and isosteric heat

The Henry constants, $K_{\mathrm{H}}$, of $CO_2$ and $CH_4$ on SWy-2 were obtained from the zeroth-order coefficient, $K_0 = \ln(K_{\mathrm{H}})$, of the virial equation (Equation 5.8), which was fitted to the excess adsorption data, as shown in Figure 5.6a. Only the zeroth and first-order virial coefficients were needed in the parameter estimation, as the coefficients of higher order all tended to zero. Also, the adsorption data considered for fitting were the points measured at bulk density values below 10 % of the liquid densities of $CO_2$ and $CH_4$ (21.1 mol/L and 26.0 mol/L, respectively) to keep the difference between absolute and excess adsorption sufficiently small ($n^{\mathrm{ex}} \approx n^{\mathrm{a}}$). These correspond to adsorption points below 50 bar for $CO_2$ and 80 bar for $CH_4$ as shown in Figure 5.6a. The advantage of using the virial treatment to obtain the Henry constant can be appreciated from the analysis of Figure 5.6b, where the same data are represented as $\ln(n^{\mathrm{ex}}/P)$ plotted against $n^{\mathrm{ex}}$. In the plot, a linear region appears well beyond the Henry's Law limit that can be conveniently used to estimate the Henry constants from the $y$-intercepts of the linear fit at $n^{\mathrm{ex}} = 0$ (Ruthven, 1984). In this thesis, however, the virial equation was used to fit the experimental data directly to reduce subjectivity of back-extrapolation. Moreover, to account for uncertainties in the measured adsorption values in determining the Henry constants, 1000 realizations of the parameter estimation have been carried out by randomly varying the experimental data within the estimated error bars. The standard deviation of the distribution of the zeroth virial coefficient was used to estimate the corresponding uncertainty value of the Henry constant. The obtained coefficients are summarized in Table 5.3 for both $CO_2$ and $CH_4$ as a function of temperature. The selectivity at the limit of zero pressure is also reported that has been calculated as the ratio of the Henry constants, i.e. $S = K_{\mathrm{H,CO_2}}/K_{\mathrm{H,CH_4}}$, with an average value $S \approx 5.5$ for the range of temperature investigated in this study. The stronger adsorption affinity towards $CO_2$ as compared to $CH_4$ for this clay is in agreement with the LDFT model results discussed above in terms of the surface-fluid interaction parameter, $\epsilon_{\mathrm{sf}}$.

When plotted as a function of the inverse of temperature (Figure 5.7), the obtained Henry constants follow a linear behavior suggesting that a correlation of the form of Equation 5.11 ap-

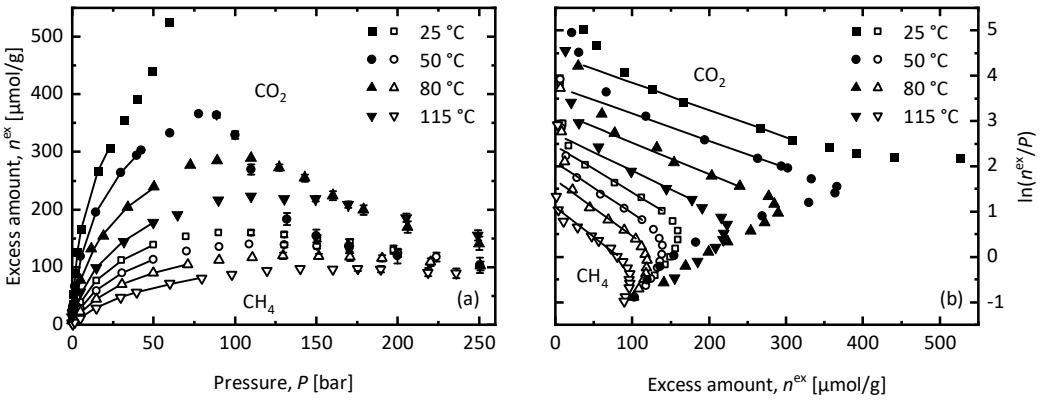



Figure 5.6: (a) Excess adsorption plotted against pressure at 25 °C to 115 °C and (b) the same data plotted as $\ln(n^{\mathrm{ex}}/P)$ versus $n^{\mathrm{ex}}$. The symbols represent experimental data for $CO_2$ (closed symbols) and $CH_4$ (open symbols), while the solid lines are fits obtained upon application of the virial equation, Equation 5.8.

Table 5.3: Henry constants, first-order virial coefficient and adsorption selectivity for $CO_2$ and $CH_4$ on SWy-2.

| T [°C] | $CO_2$ | | $CH_4$ | | Selectivity |
|---|---|---|---|---|---|
| | $K_{\mathrm{H}}$ | $K_1 \times 10^3$ | $K_{\mathrm{H}}$ | $K_1 \times 10^3$ | |
| | [µmol/g· bar] | [g/µmol] | [µmol/g· bar] | [g/µmol] | |
| 25 | $85.3 \pm 8.0$ | $6.02 \pm 0.29$ | $11.6 \pm 1.2$ | $10.3 \pm 0.8$ | $7.35 \pm 1.03$ |
| 50 | $43.3 \pm 1.1$ | $6.01 \pm 0.08$ | $8.05 \pm 0.5$ | $11.2 \pm 0.6$ | $5.38 \pm 0.36$ |
| 80 | $25.3 \pm 0.9$ | $7.01 \pm 0.15$ | $5.45 \pm 0.4$ | $12.4 \pm 0.8$ | $4.62 \pm 0.38$ |
| 115 | $15.1 \pm 0.7$ | $8.14 \pm 0.31$ | $3.00 \pm 0.1$ | $13.2 \pm 0.7$ | $5.03 \pm 0.29$ |

plies. The corresponding values of the zero coverage differential enthalpy of adsorption, $\Delta h_0$, are estimated from the slope of the straight line fitted to the experimental points. The obtained values for $CO_2$ and $CH_4$ on SWy-2 have been calculated to be $-18.4 \pm 0.6$ kJ/mol and $-14.2 \pm 0.7$ kJ/mol, respectively. The uncertainty values of $\Delta h_0$ have been obtained using the same method adopted to estimate the uncertainty values of the Henry constant. Notably, the ratio between these values is in excellent agreement with that predicted by the LDFT model, i.e. $\Delta h_{0,\mathrm{CO_2}}/\Delta h_{0,\mathrm{CH_4}} \approx \Delta h^{\mathrm{LDFT}}_{0,\mathrm{CO_2}}/\Delta h^{\mathrm{LDFT}}_{0,\mathrm{CH_4}} \approx 1.3$. Yet, the absolute values obtained from the experiments are approximately 1.5 times larger than their numerical counterparts, as shown by the solid lines plotted in Figure 5.7 that represent the LDFT model predictions. We also note that the latter have been corrected upon introducing a pre-factor $\tilde{K}^0_{\mathrm{H}}$ in Equation 4.19 ($\tilde{K}_{\mathrm{H}} = \tilde{K}^0_{\mathrm{H}} \exp(-\Delta u_0/RT)$), which would otherwise take a value of one. In this study, the pre-factor has been obtained by minimizing the difference between model prediction and experimental data in the $\ln(K_{\mathrm{H}})$ v. $1/T$ plot ($\tilde{K}^0_{\mathrm{H}} = 0.40$ µmol/g· bar for $CO_2$ and $\tilde{K}^0_{\mathrm{H}} = 0.19$ µmol/g· bar for $CH_4$). The corresponding values obtained from the linear fit to the experimental data are

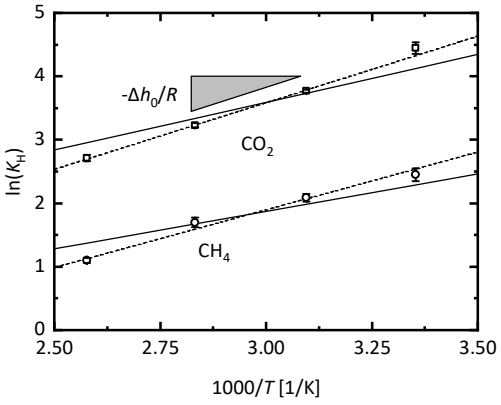



Figure 5.7: $\ln(K_{\mathrm{H}})$ plotted as a function of the inverse temperature, $1/T$, for $CO_2$ (squares) and $CH_4$ (circles) on SWy-2 in the temperature range of 25 °C to 115 °C. The symbols are obtained from fitting the virial equation to the experimental adsorption points, while the dashed lines are linear fits used to estimate the differential enthalpy of adsorption, $\Delta h_0$. The solid lines represent the Henry constant estimated using the LDFT model and corrected by fitted values of the pre-factor $\tilde{K}^0_{\mathrm{H}}$.

significantly lower, i.e. $K^0_{\mathrm{H}} = 0.050\,\mu\mathrm{mol/g\cdot bar}$ for $CO_2$ and $K^0_{\mathrm{H}} = 0.041\,\mu\mathrm{mol/g\cdot bar}$ for $CH_4$. Discrepancies of similar order have been reported between experimental and theoretical values of the pre-factor in Equation 5.11, including data for $CO_2$ and $N_2$ (Ruthven, 1984). We also argue that the required calibration of the LDFT model against the experimental values of the Henry constant reflects the lack of measurements in this study at sufficiently low bulk density values.

## 5.6 Discussion

As presented in Section 5.5.4, the LDFT model has successfully described the adsorption of $CO_2$ and $CH_4$ on SWy-2 under various experimental conditions. However, the benefits of the LDFT model need to be evaluated by considering the underlying assumptions of this approach; these include (i) the adoption of a specific structure and shape of the pores (a slit in this study); (ii) the discretization of the pore into an integer number of layers; (iii) the use of the same lattice spacing for different adsorbates. These limitations can be overcome through the use of approaches that are more rigorous (and computationally more intensive), such as Density Functional Theory (DFT) and grand canonical Monte Carlo (GCMC) simulations (Kurniawan et al., 2006). However, the ability to account for a distribution of pore sizes, which is achieved by applying the LDFT model, enables revealing adsorption behaviors that are pore-size specific and that become particularly evident at near-critical conditions. The LDFT model represents therefore a step forward compared to conventional approaches, such as semi-empirical isotherm equations that provide only

a macroscopic description of the adsorption equilibrium. These underlying features of the LDFT model and its comparison to the Langmuir model, the most commonly used empirical equation, are discussed in the following section.

### 5.6.1 $CO_2$ and $CH_4$ adsorption on SWy-2: comparison with literature data

The measurement of supercritical gas adsorption on clays is a technical and scientific challenge. The main reason for this is the intrinsic difficulty in performing the experiments and in their description, because the interactions between a supercritical gas and the clay are complex. The requirement of conducting the experiments at elevated pressures, together with the weakly sorbing nature of geomaterials sets very high demands on measurement accuracy, as demonstrated by a recent inter-laboratory comparison on carbonaceous shales, which has been only partly successful (Gasparik et al., 2014). In this context, source clays represent an excellent class of reference materials for comparing experimental data and to develop suitable protocols for supercritical adsorption experiments on geosorbents and their interpretation.

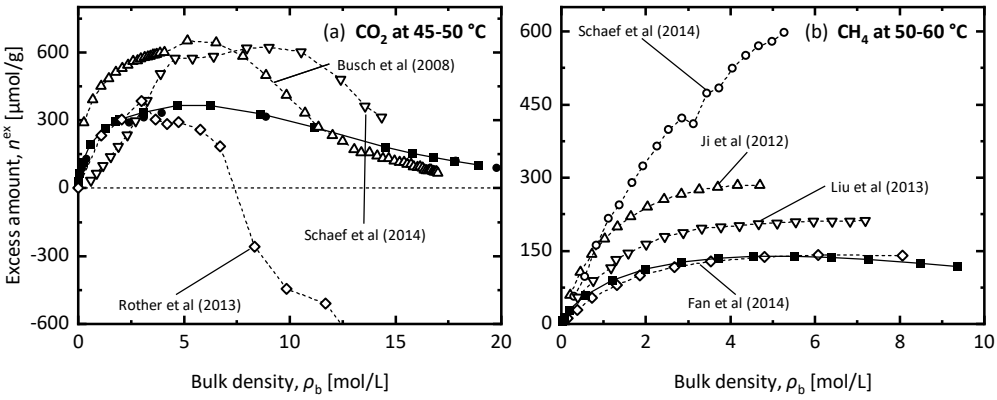



Figure 5.8: (a) Adsorption data of $CO_2$ on montmorillonite samples at 45 °C and 50 °C including results from this study (closed squares) and literature data on SWy-2 (Busch et al., 2008; Schaef et al., 2014) or Na-saturated STx-1 (Rother et al., 2013). Data from the present study combine measurements on two distinct SWy-2 samples using different gravimetric instruments by Rubotherm (closed squares and circles, the error bars have been omitted for visual clarity). (b) Adsorption data of $CH_4$ on SWy-2 (Fan et al., 2014; Schaef et al., 2014), Ca-rich montomorrilonite (Liu et al., 2013) and on a montomorillonite-rich sample (Ji et al., 2012) at 50 °C and 60 °C.

In Figure 5.8, the $CO_2$ and $CH_4$ adsorption isotherms obtained in this study are compared to adsorption isotherms reported in the literature, which were measured under similar conditions (see Table 5.4 for details). The samples studied by Liu et al. (2013) and Ji et al. (2012) are montmoril-

lonite and montmorillonite-dominated rocks (∼80 %wt.) sourced from Inner Mongolia and China, respectively, while all other samples have been sourced from the Source Clays Repository and used as-received Na-rich (Busch et al., 2008; Fan et al., 2014; Schaef et al., 2014) or by re-saturating the sample with Na ions (Rother et al., 2013).

Table 5.4: Experimental details of literature study

| Author | $T$ [°C] | Fluid | Cation | Source clay | Degas condition |
|---|---|---|---|---|---|
| Busch et al. (2008) | 45 | $CO_2$ | Na | SWy-2 | 105 °C/vacuum |
| Schaef et al. (2014) | 50 | $CO_2/CH_4$ | Na | SWy-2 | |
| Rother et al. (2013) | 50 | $CO_2$ | Na | STx-1 | |
| Fan et al. (2014) | 60 | $CH_4$ | Na | SWy-2 | 70 °C/vacuum |
| Ji et al. (2012) | 50 | $CH_4$ | | Montmorillonite† | 250 °C with He |
| Liu et al. (2013) | 60 | $CH_4$ | Ca | Montmorillonite‡ | |

† Montmorillonite dominated rock sourced from Sichuan Provnice in China
‡ Sourced from Inner Mongolia

It can be seen that the reported isotherms disagree considerably with the adsorbed amount ranging between 250 µmol/g to 650 µmol/g ($CO_2$), and 150 µmol/g to 550 µmol/g ($CH_4$) near a bulk density value of 5 mol/L (corresponding to 80 bar and 120 bar for $CO_2$ and $CH_4$ at 50 °C, respectively). The nature of the interlayer cation (e.g. Na v. Ca) affects the available micropore volume (Rutherford et al., 1997) and may explain the trend observed among the isotherms measured with $CH_4$ (Ji et al., 2012; Liu et al., 2013). In fact, higher values of SSA are reported by these studies using clay samples with possibly larger interlayer cations (>70 $m^2$/g for Ji et al. (2012) and >50 $m^2$/g for Liu et al. (2013)), as compared to the value obtained in this study (32.02 $m^2$/g). While the adsorption isotherms reported by Busch et al. (2008), Schaef et al. (2014), and Fan et al. (2014) were all measured on montmorillonite SWy-2, only the results reported by Fan et al. (2014) agree with those measured here. On the one hand, inaccuracies in the estimation of the skeletal volume may be the origin of some of the discrepancies observed at elevated pressures (see Section 5.5.2), including the appearance of negative excess adsorption values. On the other hand, the spread of the values that is observed at sufficiently low pressures indicates that this may not be the sole reason. It has been reported that incompletely dried clay samples lead to hydrated states with expanded interlayer spaces (thus, available pore spaces) (Norrish, 1954; Heller-Kallai, 2006; Schaef et al., 2012). If accessible, this interlayer space may be expanded even further due to the intercalation of adsorbing gases as seen in the case of supercritical $CO_2$, leading to larger sorption capacities (Giesting et al., 2012a; Loring et al., 2012; Schaef et al., 2012). Laboratory studies that systematically investigate the effect of exchanged cations and the hydration states on adsorption at elevated pressures are not sufficient in the literature and so is the analysis of measurement uncertainties associated with

supercritical adsorption experiments on clays. This makes it challenging to ascertain the reliability of the reported literature data and to make interlaboratory comparisons.

### 5.6.2 Adsorbed phase in clay nanopores

As briefly discussed in Section 4.2.1, a temperature-dependent saturation factor $c_{\mathrm{sat}}$ was introduced and defined as the ratio of the maximum volume occupied by the adsorbed fluid and the total pore volume. While this expedient was required to achieve a good agreement between experiments and LDFT model results, it also possesses a physical basis, as explained in the following. The achievement of $\rho_{\mathrm{max}}$ represents a theoretical limit imposed by the regular lattice; in practice, the adsorbed molecules are likely to experience packing inefficiencies in the confined pore space of the adsorbent material (Brandani et al., 2016). Furthermore, the absence of a vapor-liquid transition at supercritical conditions precludes a complete filling of the pore space by the supercritical adsorbed phase, even at extremely large pressures (Do et al., 2010). Both effects are expected to depend on the experimental temperature and to be molecule-specific. Accordingly, in our modeling approach the values of $\rho_{\mathrm{max}}$ and $v_{\mathrm{pore}}$ are kept constant (as these represent physical limits imposed by the chosen model and the material, respectively), while the specific volume of the supercritical adsorbed phase can vary, reaching a value at "saturation" ($= c_{\mathrm{sat}} v_{\mathrm{pore}}$) that is temperature- and fluid-dependent. This definition of the saturation factor is somewhat analogous to earlier attempts introduced to capture this variability in the LDFT adsorption model, such as the temperature-dependent pore-filling capacity ($\rho_{\mathrm{max}} v_{\mathrm{pore}}$) (Hocker et al., 2003) or the so-called "isotherm pre-factor" that accounts for the temperature-variable density of active pores (Bénard and Chahine, 1997, 2001).

The values of $c_{\mathrm{sat}}$ obtained in this study are plotted in Figure 5.9 as a function of temperature and for each fluid. For both $CO_2$ and $CH_4$, the values of $c_{\mathrm{sat}}$ suggest that the pores are far from being fully saturated with adsorbed fluid ($c_{\mathrm{sat}} < 0.7$ for $CO_2$ and $c_{\mathrm{sat}} < 0.5$ for $CH_4$). Interestingly, the value of this parameter (i) increases with decreasing temperature and (ii) is larger for $CO_2$ ($c_{\mathrm{sat}} = 0.55 - 0.7$) as compared to $CH_4$ ($c_{\mathrm{sat}} = 0.4 - 0.45$) at equivalent temperature. Upon normalization of the experiment temperature with the critical temperature, the data delineate a common curve (shown in the inset of Figure 5.9), where the volume occupied by the adsorbed phase increases with decreasing temperature with a gradient that becomes steeper as the critical temperature is approached. This behavior is reminiscent of early observations of critical adsorption on porous solids (Blümel and Findenegg, 1985) and suggests that complete saturation of the

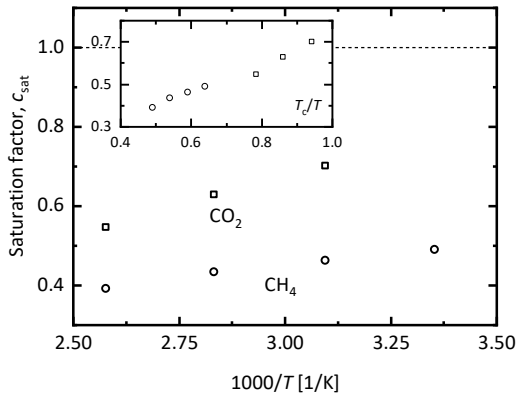



Figure 5.9: Pore volume saturation factor, $c_{\mathrm{sat}}$, as a function of $1/T$, as predicted from the LDFT model fitted to the experimental supercritical adsorption data. Symbols represent model results at the given experimental temperature for $CO_2$ (squares) and $CH_4$ (circles), and the dashed line show $c_{\mathrm{sat}} = 1$ that is attained at complete saturation. The inset plot shows the same values of $c_{\mathrm{sat}}$ plotted against $T_{\mathrm{c}}/T$, where $T_{\mathrm{c}}$ is the critical temperature.

pore space in clays may be achieved at near-critical conditions. This interesting finding has been corroborated with additional experimental data on different substrates in Chapter 6.

### 5.6.3 Modeling supercritical adsorption on geosorbents

The successful application of the LDFT model to describe supercritical adsorption on SWy-2 leads to the question of whether simpler and semi-empirical adsorption models would be equally suitable. The Langmuir model is a widely used example of such models and has been previously applied to clays (Ji et al., 2012; Liu et al., 2013; Fan et al., 2014; Heller and Zoback, 2014). As described in Section 4.3, the LDFT model reduces to the Langmuir equation (Equation 4.16) when adsorption coverage is limited to a monolayer and the interaction energy between fluid molecules is neglected. The obtained equation can be dimensionalized and combined with the definition of the excess amount of adsorption to yield the following expression:

$$n^{\mathrm{ex}} = \frac{n^{\infty} k_{\mathrm{L}} f}{1 + k_{\mathrm{L}} f} \left(1 - \frac{\rho_{\mathrm{b}}}{\rho_{\mathrm{a}}}\right) \tag{5.13}$$

where $n^{\infty}$ is the monolayer capacity, $k_{\mathrm{L}}$ is the Langmuir equilibrium constant, $f$ is the fugacity, and $\rho_{\mathrm{a}}$ is the adsorbed phase density. To describe adsorption in the high-pressure range, the value of $\rho_{\mathrm{a}}$ is assumed, usually equal to the liquid density at specific conditions (Pini, 2014). In the following, two scenarios are investigated, namely where this density is taken as the maximum value determined by the LDFT model ($\rho_{\mathrm{max}} = 26.8\,\mathrm{mol/L}$ for $CO_2$ and $\rho_{\mathrm{max}} = 24.9\,\mathrm{mol/L}$ for $CH_4$) or

where it is used as a fitting parameter (see Table 5.5). The results from this parameter estimation are presented in Figure 5.10a ($CO_2$) and b ($CH_4$) for the excess adsorption isotherms measured on SWy-2 at 50 °C, where the relative percentage error between experiment and models (Langmuir and LDFT) is plotted as a function of the bulk density. For the sake of clearer representation, only one Langmuir scenario is shown where the adsorbed phase density was used as fitting parameter.

Table 5.5: Langmuir model parameters

| Model | Parameter | Unit | $CO_2$ | $CH_4$ |
|---|---|---|---|---|
| Scenario 1 | $n^{\infty}$ | [µmol/g] | 606 | 243 |
| | $k_{\mathrm{L}}$ | [$\mathrm{bar}^{-1}$] | 0.036 | 0.023 |
| | $\rho_{\mathrm{a}}$ | [mol/L] | 26.8† | 24.9† |
| Scenario 2 | $n^{\infty}$ | [µmol/g] | 888 | 256 |
| | $k_{\mathrm{L}}$ | [$\mathrm{bar}^{-1}$] | 0.018 | 0.021 |
| | $\rho_{\mathrm{a}}$ | [mol/L] | 23.2 | 23.1 |

† Values of $\rho_{\max}$ obtained from the LDFT model

It can be seen that both models perform equally well on the $CH_4$ data; deviations are generally less than 5 % and the values of the minimized objective function normalized by the maximum excess adsorbed amount ($\widehat{\Phi} = \Phi/n^{\mathrm{ex}}_{\max}$) are small ($\widehat{\Phi} = 2.7\,\mu\mathrm{mol/g}$ and $\widehat{\Phi} = 1.2\,\mu\mathrm{mol/g}$ for the LDFT and Langmuir model, respectively). On the contrary, the two models differ considerably in the description of the $CO_2$ isotherm, where the LDFT model ($\widehat{\Phi} = 11\,\mu\mathrm{mol/g}$) now outperforms the Langmuir model ($\widehat{\Phi} = 22\,\mu\mathrm{mol/g}$). We note that statistical significance is implied here, because both models use the same number of adjustable parameters to find the optimum match to the experimental data.

Figure 5.10c compares excess adsorption isotherms on SWy-2 at 50 °C obtained upon application of the LDFT and Langmuir models. For the latter, two sets of curves are shown to represent the results obtained for different (constant) values of the adsorbed phase density. In agreement with the considerations above, both models produce similar isotherms for $CH_4$, which therefore both agree with the experimental data. Deviations are observed only for $\rho_{\mathrm{b}} > 10\,\mathrm{mol/L}$, but the validation of the model predictions at these elevated bulk densities is precluded by the lack of experimental observations above 250 bar. The $CO_2$ isotherms produced by the two models are quite different; as shown in the figure, only the LDFT model matches the experimental data well, while both Langmuir fits result in significantly larger values of the minimized objective function ($\widehat{\Phi} = 22\,\mu\mathrm{mol/g}$ for $\rho_{\mathrm{a}} = 23.1\,\mathrm{mol/L}$ and $\widehat{\Phi} = 35\,\mu\mathrm{mol/g}$ for $\rho_{\mathrm{a}} = 26.8\,\mathrm{mol/L}$). Notably, the Langmuir model misplaces systematically the maximum excess adsorbed amount and fails at capturing the characteristic non-linear descending part of the isotherm for both scenarios considered. As anticipated above,

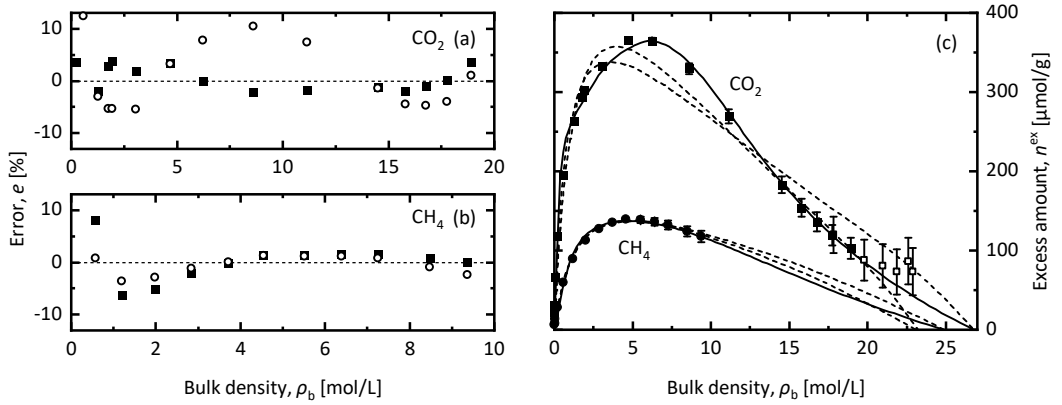



Figure 5.10: Relative deviations between experiment and model (LDFT - closed squares; Langmuir model - open circles) as a function of the bulk density for the isotherms measured at 50 °C on SWy-2 with (a) $CO_2$ and (b) $CH_4$. (c) The corresponding experimental excess adsorption isotherms (symbols) are compared to predictions by the LDFT (solid lines) and Langmuir model (dashed lines - two scenarios). The filled symbols are the same data reported in Figure 5.5, while the empty symbols are measurements carried out in a different Rubotherm balance up to 650 bar.

the ability to validate these models at elevated bulk densities is often limited by the scarcity of experimental data. In the figure, fresh data are shown that have been measured in this study between 200 bar and 650 bar on SWy-2 using a different Rubotherm balance that is able to achieve these extreme conditions ($\rho_b > 20$ mol/L). The agreement between these data and the LDFT prediction is satisfactory considering the small values of the excess adsorbed amount at these elevated pressures (∼100 µmol/g) and the associated measurement uncertainties (shown by the error bars). In particular, we note that in agreement with the LDFT model and contrary to the Langmuir model, the experiments outline a convex isotherm shape with increasing bulk density.

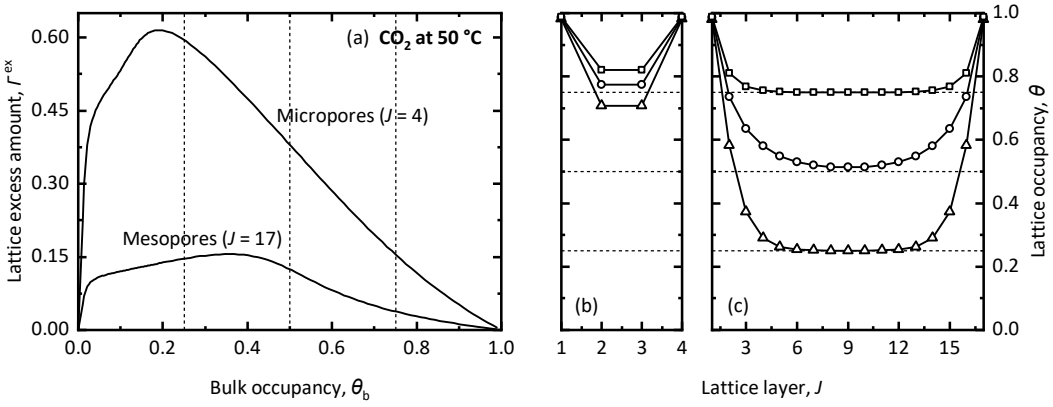



Figure 5.11: (a) Lattice excess adsorption isotherms computed for $CO_2$ at 50 °C in two pores, namely 4 (micropores) and 17 layers (mesopores). The corresponding lattice occupancy profiles in (b) 4 layer pore and (c) 17 layer pore. The dashed lines represent the values of $\theta_b$: 0.25, 0.5, and 0.75.

The richer (and more complex) behavior of the $CO_2$ isotherm can be traced back to the temperature of the experiment, which is closer to the fluid critical temperature ($T/T_c = 1.06$) as compared to $CH_4$ ($T/T_c = 1.7$). The vicinity to the critical point is such that confinement effects in pores become more pronounced and the isotherm shape reflects features that can be associated with a specific distribution of pore sizes (Hocker et al., 2003). In SWy-2, these features are typical of a material that possesses a large fraction of mesopores for which the isotherm maximum occurs at higher density ($\rho_b > 5\,\text{mol/L}$) and the bending behavior of the isotherm becomes more pronounced, as observed in commercial mesoporous adsorbents (Di Giovanni et al., 2001; Pini et al., 2008). The LDFT model can be used to reveal these patterns, because it produces individual, pore-specific isotherms and pore-density profiles, as shown in Figure 5.11. In the figure, (a) excess isotherms and (b)/(c) pore occupancy profiles are presented in lattice units and refer to $CO_2$ adsorption data computed at 50 °C in micro- and mesopores with 4 and 17 layers, respectively (corresponding to 1.6 nm and 6.8 nm). In the micropore, adsorption at low coverages increases steeply reaching a maximum at approximately $\theta_b = 0.2$ followed by a fairly linear decrease. On the contrary, in the mesopore the increase in the adsorbed amount is more gentle, the maximum is reached only at $\theta_b = 0.4$ and the descending part is characterized by a pronounced curvature. It is the combination of these features that gives rise to the behavior observed experimentally and shown in Figure 5.10c. Accordingly, the greater value of lattice adsorption in the micropores as compared to the mesopores is the manifestation of the lattice occupancy profiles observed in these pores and shown in Figure 5.11b and c. Although the fluid-solid interaction parameter, $\epsilon_{sf}$, is the same for both pores, the close proximity of the parallel pore walls inside the micropores causes the values of lattice occupancy of all layers to be above their corresponding values of bulk occupancy. In contrast, fluid densification in the mesopores is reached only near the walls, while in the center of the pores the lattice occupancy profiles plateau to the bulk values.

## 5.7 Concluding remarks

A combined experimental and modeling approach has been employed to understand the adsorption mechanisms of $CO_2$ and $CH_4$ on clay minerals relevant to many applications, including the geological storage of $CO_2$ and the recovery of shale gas. In this study, the adsorption of $CO_2$ and $CH_4$ on dry Na-montmorillonite (SWy-2) has been measured over a wide range of temperature and pressure conditions using a gravimetric technique. The experimental data have been evaluated using both net and excess adsorption formalisms. The results indicate that $CO_2$ adsorbs more

strongly than $CH_4$ on SWy-2, as quantified by the selectivity, $S = K_{H,CO_2}/K_{H,CH_4} \approx 5.5$, and the adsorption energetics, $\Delta h_{0,CO_2}/\Delta h_{0,CH_4} \approx 1.3$. The adsorption isotherms have been successfully described by the LDFT model, which proves to be more rigorous and accurate than semi-empirical approaches based on the Langmuir isotherm (or variations thereof). The model uses the pore-size distribution of the material as input parameter and provides estimates of the isosteric heat that compare favorably with results obtained experimentally. Most significantly, the LDFT model reveals adsorption behaviors that are pore-size specific; these effects become particularly evident for isotherms that are measured at slightly supercritical temperatures ($CO_2$ in this study) in materials that possess a significant amount of mesoporosity, such as the clay investigated here. We contend that this observation is not limited to $CO_2$ and SWy-2, but that these phenomena are likely to be observed in other clay-rich rocks and with other relevant geo-fluids, such as light hydrocarbons or their mixtures that attain near-critical conditions at subsurface conditions.

# Chapter 6

# Supercritical sorption on illite and smectite clay minerals

Reprinted (adapted) with permission from Junyoung Hwang and Ronny Pini. Supercritical $CO_2$ and $CH_4$ Uptake by Illite-Smectite Clay Minerals. *Environmental Science and Technology* 2019, 53 (19), 11588–11596. Copyright 2019 American Chemical Society.

## 6.1 Introduction

As presented in the previous chapter, a workflow has been successfully developed to describe supercritical adsorption on clay minerals, including methods of data analysis and interpretation and a modeling approach that describes adsorption in terms of the complex textural properties of clay minerals. In this chapter, this workflow has been employed to describe supercritical adsorption of $CO_2$ and $CH_4$ of three illite and smectite clay minerals, which are most common in the mineralogy of sedimentary formations (Weaver, 1956), up to 300 bar at 25 °C to 115 °C. The structural properties of the clay minerals in this chapter have been characterized in a more thorough manner than reported in the previous chapter by complementing the $N_2$ analysis with physisorption experiments of Ar and $CO_2$ as recommended by the recent IUPAC report (Thommes et al., 2015) using Autosorb iQ from Quantachrome Instruments that has been set up in the laboratory. It should be noted that the $N_2$ physisorption measurements on SWy-2 have been repeated using Autosorb iQ, and the newly measured results are reported in this chapter. The physisorption measurements of

$N_2$, Ar, and $CO_2$ have been analyzed using the non-local density functional theory (NLDFT) and grand canonical Monte Carlo (GCMC) that are commercially available through Quantachrome's proprietary software, which are more sophisticated and comprehensive than the conventional theories. The findings reported in the previous chapter have been validated and further consolidated through collection of data from multiple samples with different porous structure and adsorption metrics.

## 6.2 Materials and experimental methods

The clay mineral samples are Na-rich montmorillonite (SWy-2), illite-smectite mixed layer (ISCz-1), and illite (IMt-2) all sourced from the Source Clay Repository of the Clay Minerals Society (Virginia, USA). The same pure gases listed in Section 5.2 were used. For the sorption measurements of $CO_2$ and $CH_4$ on IMt-2, the sample holder with a mesh lid was used as described in Section 3.2, the mass and volume of which have been measured to be 7.7045 g ($2 \times 10^{-5}$ g) and 1.4195 $cm^3$ ($1 \times 10^{-4}$ $cm^3$), respectively (the values in parentheses are uncertainty values).

### 6.2.1 Gas physisorption experiments

The textural properties of the clay minerals were characterized by low-pressure adsorption and desorption experiments using $N_2$ (77 K) and Ar (87 K) for micro- and mesopore analyses and $CO_2$ (273 K) for further micropore analysis as recommended by the most recent IUPAC guidelines (Thommes et al., 2015). The same degassing conditions and procedure were used as in Chapter 5. The experiments were performed in the pressure range of $3 \times 10^{-7}$ MPa to $1 \times 10^{-1}$ MPa using Autosorb iQ (Quantachrome Instruments, Florida, USA) equipped with the CryoSync module, which enables achieving cryogenic temperatures above the standard boiling point temperature of $N_2$ (77 K) without using additional cryogenic liquids. For experiments with $CO_2$, a liquid circulating thermostat (Julabo CORIO CD-200F, Seelbach, Germany) was used to control the temperature of a bath containing a water-ethylene glycol (50 vol%) mixture.

### 6.2.2 High-pressure sorption experiments

The high-pressure measurements were conducted in the pressure range of 0.15 bar to 300 bar at 25 °C, 50 °C, 80 °C and 115 °C using the experimental setup described in Chapter 3. The same

degassing conditions and procedure were used as in Chapter 5.

## 6.3 Results and discussion

### 6.3.1 Textural properties of illite and smectite clay minerals

Illite and smectite clay minerals contain nanopores of various sizes, including micro- ($< 2\,\text{nm}$), meso- (2 to 50 nm) and macropores ($> 50\,\text{nm}$). With reference to Bergaya and Lagaly (2006), these are largely associated with the interlayer regions, as well as voids created through the assembly of clay mineral particles and their aggregates. The physisorption isotherms of $N_2$ (77 K), Ar (87 K), and $CO_2$ (273 K) for SWy-2, ISCz-1, and IMt-2 are shown in Figure 6.1. The shapes of both

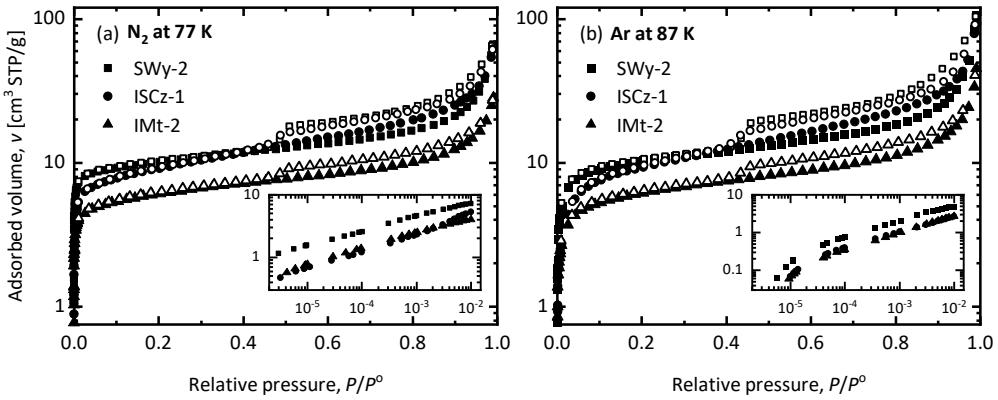



Figure 6.1: Adsorption (closed symbols) and desorption (open symbols) isotherms of (a) $N_2$ at 77 K and (b) Ar at 87 K on the clay minerals. The inset plots show the filling of the micropores for $P/P^o < 0.01$.

$N_2$ and Ar isotherms for all three clay minerals indicate the presence of a cavitation-induced H3 hysteresis loop that closes around $P/P^o \approx 0.4$; this type of isotherms implies that these materials consist of a fair amount of small mesopores (Groen et al., 2003; Kuila and Prasad, 2013) and is characteristic of slit-shaped pores (Thommes et al., 2015), which in clays are formed by the stacking of platy mineral particles. The steeper increase of the isotherms measured on ISCz-1 for $P/P^o > 0.01$ suggests a broader mesopore distribution as compared to SWy-2 and IMt-2. The inset plots of Figure 6.1 reveal appreciable adsorbed amounts in micropores ($P/P^o < 0.01$) with SWy-2 showing the largest amount adsorbed compared to the other two clays. This trend is better identified through the measurements with $CO_2$ shown in Figure 6.2, for which the strength of adsorption increases in the order of ISCz-1 < IMt-2 < SWy-2.

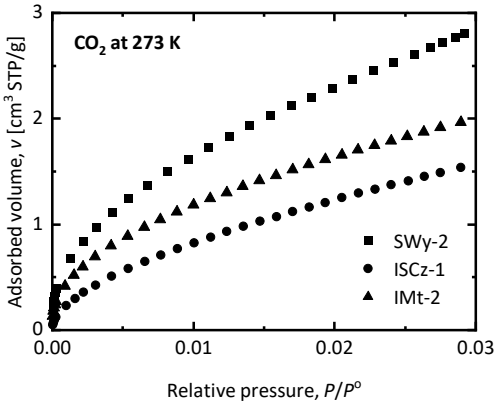



Figure 6.2: Adsorption isotherms of $CO_2$ at 273 K up to 760 Torr ($P/P^o \approx 0.03$, $P^0 = 26141$ Torr).

These experimental observations are verified by the pore volumes of the clay minerals computed using the NLDFT (for $N_2$ and Ar) and GCMC (for $CO_2$) that are summarized in Table 6.1. The adsorbent type and pore geometry adapted are zeolite cylindrical model and carbon model

Table 6.1: Summary of the textural properties of SWy-2, ISCz-1, and IMt-2.

| Property | Probe gas | Unit | SWy-2 | ISCz-1 | IMt-2 |
|---|---|---|---|---|---|
| **Pore volume**† | $N_2$ | $[cm^3/g]$ | 0.080 | 0.078 | 0.036 |
| | Ar | $[cm^3/g]$ | 0.110 | 0.101 | 0.044 |
| Micropore | $N_2$ | $[cm^3/g]$ | 0.007 | 0.001 | 0.003 |
| | Ar | $[cm^3/g]$ | 0.008 | 0.003 | 0.004 |
| | $CO_2$‡ | $[cm^3/g]$ | 0.009 | 0.006 | 0.007 |
| Mesopore | $N_2$ | $[cm^3/g]$ | 0.055 | 0.062 | 0.026 |
| | Ar | $[cm^3/g]$ | 0.059 | 0.064 | 0.026 |
| Macropore | $N_2$ | $[cm^3/g]$ | 0.018 | 0.015 | 0.007 |
| | Ar | $[cm^3/g]$ | 0.043 | 0.034 | 0.014 |
| **Specific surface area** | | | | | |
| BET | $N_2$ | $[m^2/g]$ | $36.72 \pm 0.06$ | $32.58 \pm 0.10$ | $21.90 \pm 0.09$ |
| | Ar | $[m^2/g]$ | $33.13 \pm 0.14$ | $30.15 \pm 0.16$ | $19.82 \pm 0.06$ |
| **Skeletal density** | | | | | |
| He gravimetry | He | $[g/cm^3]$ | $2.709 \pm 0.006$ | $2.689 \pm 0.009$ | $2.784 \pm 0.004$ |

† NLDFT on zeolite cylindrical pore model
‡ GCMC on carbon slit pore model

for the NLDFT and GCMC, respectively (see Appendix C). Although the clay minerals do not match exactly with the employed adsorbent type and pore geometry, the values of fitting error were reasonable low: 0.45 % to 0.77 % for $N_2$, 0.45 % to 0.65 % for Ar, and 1.07 % to 3.72 % for $CO_2$. The total pore volume of the clay minerals increase in the order IMt-2 < ISCz-1 < SWy-2 with values estimated using Ar as the probing gas being consistently larger (20 to 40 % for

the total pore volume) than those obtained from $N_2$ measurements across the entire pore-size distributions (micro-, meso-, and macropores). Notably, ISCz-1 shows the largest mesopore volume and a broader distribution of mesoporosity, while SWy-2 and IMt-2 show larger micropore volumes (contributing to 8 % and 16 % of the total pore volume, respectively). These observations highlight that the textural properties of mixed layer clay particles (ISCz-1) are not the result of the simple combination of the properties of the constituent layers (illite and smectite).

The specific surface areas (SSA) obtained by the application of the BET equation (Brunauer et al., 1938) are also summarized in Table 6.1. A good agreement is observed between estimates from $N_2$ and Ar measurements (6 to 9 % relative difference), which also show a positive correlation with the measured total pore volume. The estimated SSA values are consistent with those reported in the literature (Cheng and Huang, 2004; Carmody et al., 2007; Dogan et al., 2007; Busch et al., 2008; Kuila and Prasad, 2013; Joewondo, 2018), but significantly smaller than those obtained by adsorption of polar liquids, such as water or ethylene glycol monoethyl ether (EGME), that are approximately $100\,m^2/g$ for illite and over $500\,m^2/g$ for montmorillonite (Macht et al., 2011). While it is known that micropores in clays are only partly accessible to $N_2$, we show here for the first time that the same is true for Ar, thereby confirming that kinetics restrictions in very narrow micropores are present at cryogenic temperatures (77 and 87 K) (Thommes et al., 2015). The values of skeletal density have been calculated from the skeletal volume measured through He gravimetry as shown in Figure 6.3. Interestingly, an excellent agreement is found for IMt-2 between

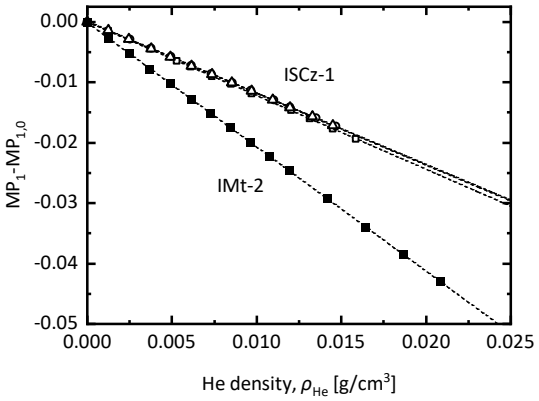



Figure 6.3: Normalized measured weight plotted against the He bulk density for ISCz-1 (open symbols) and IMt-2 (closed symbols). The measurements on SWy-2 are shown in Figure 5.3 in Chapter 5. The measurements for ISCz-1 show three different data sets as the experiment was interrupted, therefore, multiple sets were measured to test the possibility of sample loss.

crystallographic skeletal density values (Deeds and Van Olphen, 1961b) ($\rho_{cryst} = 2.780\,g/cm^3$) and

values measured by He gravimetry ($\rho_{sk} = 2.784\,g/cm^3$). However, a significant discrepancy is observed for SWy-2 ($\rho_{sk} = 2.709\,g/cm^3 < \rho_{cryst} = 2.798\,g/cm^3$ (Deeds and Van Olphen, 1961b)), indicating micropore inaccessibility to He. This peculiar pore accessibility of illite and smectite clays is also reflected in the micropore volumes obtained from $CO_2$ isotherms, which are 10 % (SWy-2), 80 % (IMt-2), and 100 % (ISCz-1) larger than the values obtained using Ar. These observations highlight the importance of conducting physisorption analyses with multiple probing gases to correctly represent the pore volumes of each pore class – micropores by $CO_2$ and mesopores by $N_2$ and Ar – in developing adsorption models that use such textural information.

### 6.3.2 Supercritical adsorption isotherms of $CO_2$ and $CH_4$

The excess adsorption and desorption isotherms of supercritical $CO_2$ and $CH_4$ on SWy-2, ISCz-1, and IMt-2 at four temperatures (25 to 115 °C) up to 300 bar are presented in Figure 6.4 as a function of the bulk fluid density. For the three clays and for both fluids, the excess isotherms are positive indicating that sorption contributes to gas storage inside clay nanopores throughout the entire pressure range investigated. While all the measured isotherms possess the non-monotonic behavior that is characteristic of excess adsorption data, they also reveal subtle differences that originate from the clay-specific pore-size distributions discussed in Section 6.3.1. SWy-2 and ISCz-1 show similar uptake capacities and their isotherm shapes resemble that of a mesoporous material, such as silica gel (Hocker et al., 2003; Pini et al., 2008), where the gradual increase in the adsorbed amount reaches a maximum at $\rho_b \geq 5\,mol/L$. However, the larger fraction of mesopores in ISCz-1 is also responsible for the characteristic pore-filling mechanism that produces a stronger dependence of the adsorbed amount on temperature compared to SWy-2 (particularly evident for the $CO_2$ isotherms measured at 50 °C and 80 °C). Smaller $CO_2$ and $CH_4$ uptakes are observed for IMt-2, reflecting its smaller total pore volume. However, the large fraction of micropores of IMt-2 results in a steep initial increase of the measured isotherms that is indeed typical of microporous materials (Moellmer et al., 2011; Schell et al., 2012; Pini, 2014; Murialdo et al., 2018). Interestingly, the isotherms of IMt-2 also show moderate, but not negligible, hystereses for both $CO_2$ and $CH_4$ at all temperatures. Previous observations of hysteresis at supercritical conditions have been limited to swelling clay minerals, such as smectite (Jeon et al., 2014; Zhao et al., 2018), the microstructure of which is sensitive to water content (Giesting et al., 2012a). Because IMt-2 is non-swelling, we attribute this observation to strongly attached $CO_2$ and $CH_4$ that are only removed at sufficiently high temperatures. The supercritical desorption isotherms indeed show sorbed amounts of both

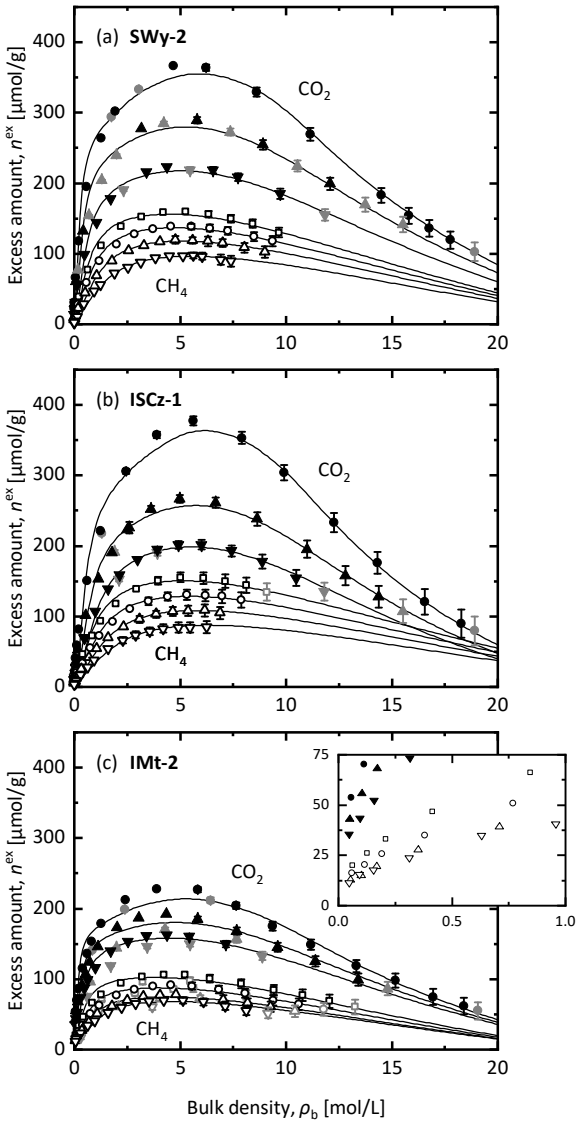



Figure 6.4: Supercritical adsorption (black) and desorption (grey) isotherms of $CO_2$ (filled symbols) and $CH_4$ (open symbols) on (a) SWy-2, (b) ISCz-1, and (c) IMt-2 up to 300 bar at 25, 50, 80 and 115 °C (loading decreases with increasing temperature). The inset plot of (c) shows the desorption points of IMt-2 under 1 mol/L. The solid lines are the LDFT model fits.

gases that persist between 10 $\mu$mol/g to 50 $\mu$mol/g at approximately 1.5 bar (inset of Figure 6.4c). Recent findings have revealed $CO_2$ interlayer trapping in muscovite (used as a proxy for illite) following incubation at 12 MPa and 90 °C (Wan et al., 2018). While they are not sufficient to define the controlling mechanisms for this phenomenon, our sorption results support these observations and extend them to $CH_4$ while covering a broader range of temperature and pressure.

### 6.3.3 Supercritical adsorption model

The LDFT model incorporates the materials' pore-size distributions and correctly describes the experimental isotherms as can be seen from the solid lines in Figure 6.4. Both adsorption and desorption data were used in fitting the isotherms of SWy-2 and ISCz-1, but only desorption data were used for IMt-2 due to the presence of the hysteresis loops and the limited amount of adsorption data.

Table 6.2: LDFT model parameters

| Parameter | Unit | Fluid | SWy-2 | ISCz-1 | IMt-2 |
|---|---|---|---|---|---|
| $\epsilon_{sf}/k$ | [K] | $CO_2$ | −1131.3 | −898.3 | −1277.2 |
| | | $CH_4$ | −859.5 | −771.1 | −969.7 |
| $\rho_{max}$ | [mol/L] | $CO_2$ | 26.95 | 24.78 | 25.43 |
| | | $CH_4$ | 26.45 | 28.78 | 24.13 |

The values of the fitted parameters, $\epsilon_{sf}$ and $\rho_{max}$, are summarized in Table 6.2. The attainment of $\rho_{max}$ corresponds to the complete filling of the lattice, at which the adsorbed density is equal to the bulk density. Comparable values were found for all three clay minerals for both $CO_2$ and $CH_4$, namely $\rho_{max} = 25.72 \pm 1.23$ mol/L for $CO_2$ and $\rho_{max} = 25.45 \pm 2.33$ mol/L, corresponding to $\rho_{max}/\rho_c \approx 2.5$. These values agree well with those previously reported from the application of the LDFT model for $CO_2$ and $CH_4$ on activated carbon (Bénard and Chahine, 1997; Sudibandriyo et al., 2010), as well as with the liquid densities at triple point $CO_2$ and standard boiling point of $CH_4$ (see Table 6.3). However, as indicated by GCMC simulations of supercritical adsorption in shale (Zhao et al., 2018), adsorbed phase densities are not constant and may differ from the saturated liquid densities. The LDFT model shows a similar behavior as summarized in Table 6.3, where the average density values of the first two adsorbed layers in each clay mineral are reported for both $CO_2$ and $CH_4$. While for $CO_2$ the obtained values are about 20 % below the saturated liquid density, the estimates for $CH_4$ are even lower (40 %), reflecting the equilibration with a bulk phase that has a lower density under the same temperature and pressure conditions. For $CH_4$

Table 6.3: Comparison of the calculated adsorbed densities of $CO_2$ and $CH_4$ with their respective liquid densities.

| Fluid | $P$ | $T$ | $\rho_{liq}$ | $P$ | $T$ | $\rho_{GCMC}$ [†] | $\rho_{LDFT}$ [‡] | | |
|---|---|---|---|---|---|---|---|---|---|
| | | | | | | | SWy-2 | ISCz-1 | IMt-2 |
| | [bar] | [°C] | [mol/L] | [bar] | [°C] | [mol/L] | [mol/L] | | |
| $CO_2$ | 5.187 | -56.56 | 26.78 | 150 | 60 | 25.53 | 22.09 | 20.52 | 21.35 |
| $CH_4$ | 1.013 | -161.48 | 26.33 | 150 | 60 | 17.42 | 15.26 | 15.26 | 15.09 |

[†] The area between the first two peaks of a density profile inside slit pores with structureless carbon surfaces simulated by GCMC (Zhao et al., 2018)
[‡] The average density of the first two adsorbed layers

on illite, adsorbed densities obtained by GCMC simulations (13.1 to 14.3 mol/L) reveal that this phenomenon persists even at a higher pressure (30 MPa at 90 °C) (Chen et al., 2018).

### 6.3.4 Adsorption energetics

The Henry constants, $K_H$, were obtained by describing the experimental data with the virial equation as descibed in Section 5.4.3 and 5.5.5. The virial plots in Figure 6.5 show discernible linear regions and the plot of $\ln(K_H)$ against $1/T$ (see Figure 6.6a) show good fits to linear regression ($R^2 = 0.967-0.996$), which validate the suitability of the approach to estimate the Henry constants. The data are summarized in Table 6.4 together with estimates of $\Delta h_0$ calculated from Equation 5.10 and the selectivity of $CO_2$ to $CH_4$ ($S = K_{H,CO_2}/K_{H,CH_4}$).

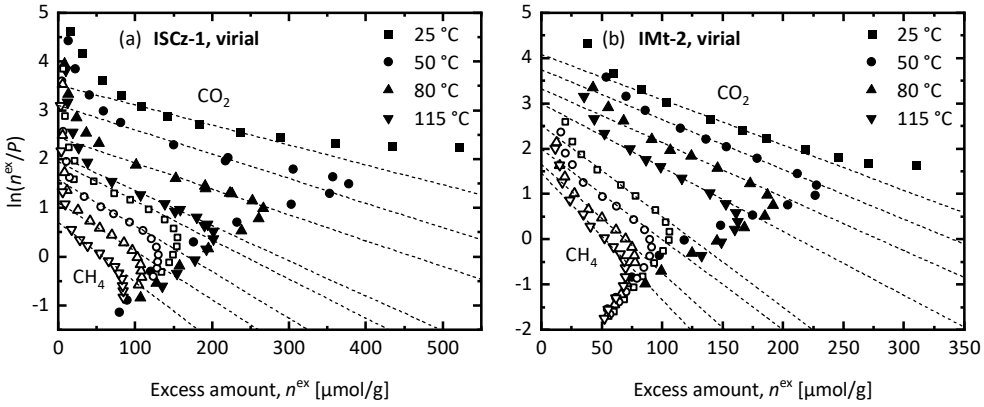



Figure 6.5: Excess adsorption isotherms of $CO_2$ (closed symbols) and $CH_4$ (open symbols) plotted in the virial format for (b) ISCz-1 and (c) IMt-2. The dashed lines are linear fits obtained with the two-parameter virial equation, and describe the linear regions that are well visible in the experimental isotherms.

The values of $|\Delta h_0|$ decrease from SWy-2 to IMt-2, consistent with estimates by Ji et al. (2012) for $CH_4$ on rocks each dominated by clays in this study. While $|\Delta h_0|$ is expected to increase

Table 6.4: Henry's constants, selectivity, and enthalpy of adsorption at zero coverage for $CO_2$ and $CH_4$ adsorption on SWy-2, ISCZ-1, and IMt-2.

| Sample | T [°C] | $K_{H,CO_2}$ | $K_{H,CH_4}$ | $S$ | $\Delta h_0$ $CO_2$ | $\Delta h_0$ $CH_4$ |
|---|---|---|---|---|---|---|
| | | [µmol/g· bar] | | [-] | [kJ/mol] | |
| SWy-2 | 25 | $85.3 \pm 8.0$ | $11.6 \pm 1.2$ | $7.4 \pm 1.0$ | $-18.4 \pm 0.6$ | $-14.2 \pm 0.7$ |
| | 50 | $43.3 \pm 1.1$ | $8.1 \pm 0.5$ | $5.3 \pm 0.4$ | | |
| | 80 | $25.3 \pm 0.9$ | $5.5 \pm 0.4$ | $4.6 \pm 0.4$ | | |
| | 115 | $15.1 \pm 0.7$ | $3.0 \pm 0.1$ | $5.0 \pm 0.3$ | | |
| ISCz-1 | 25 | $29.8 \pm 1.2$ | $7.0 \pm 0.4$ | $4.3 \pm 0.3$ | $-14.7 \pm 0.4$ | $-12.8 \pm 0.9$ |
| | 50 | $22.2 \pm 0.8$ | $4.9 \pm 0.4$ | $4.5 \pm 0.4$ | | |
| | 80 | $11.6 \pm 1.2$ | $3.0 \pm 0.1$ | $3.9 \pm 0.4$ | | |
| | 115 | $8.0 \pm 0.4$ | $2.2 \pm 0.3$ | $3.6 \pm 0.5$ | | |
| IMt-2 | 25 | $60.2 \pm 4.5$ | $12.0 \pm 1.3$ | $5.0 \pm 0.7$ | $-12.0 \pm 0.9$ | $-11.0 \pm 0.8$ |
| | 50 | $42.1 \pm 1.4$ | $7.8 \pm 0.6$ | $5.4 \pm 0.5$ | | |
| | 80 | $27.6 \pm 2.7$ | $5.5 \pm 0.6$ | $5.0 \pm 0.7$ | | |
| | 115 | $20.0 \pm 2.9$ | $4.3 \pm 0.4$ | $4.7 \pm 0.8$ | | |

with decreasing pore diameter (Myers, 2004a), IMt-2 shows the lowest value of $|\Delta h_0|$ despite its larger fraction of micropores. This suggests that adsorption energetics in clays may be additionally affected by other factors, such as the surface chemistry, as indicated by the observed decrease of $|\Delta h_0|$ with increasing illite content (Ji et al., 2012). As discussed previously in Section 5.5.4, these values are also on the lower end of the range indicated by the general approximation proposed for gas physisorption (Ruthven, 2000), i.e. $|\Delta h_0| < 1.5 - 2|\Delta h_{vap}|$, where $|\Delta h_{vap}|$ is the latent heat of condensation (10.3 kJ/mol for $CO_2$ at 273.15 K and 8.2 kJ/mol for $CH_4$ at 112 K (Lemmon et al., 1998)). The estimates of $\Delta h_0$ obtained from the LDFT model in the Henry's region (up to 0.3 bar) do not reveal any specific trend among the three clays ($|\Delta h_{0,CO_2}^{LDFT}| \approx 16.3 \pm 0.8$ kJ/mol and $|\Delta h_{0,CH_4}^{LDFT}| \approx 13.1 \pm 0.5$ kJ/mol). Most significantly, they compare well with their experimental counterparts and the observed discrepancy for IMt-2 is likely due to the model's description of the large sorption amounts in the low-pressure regions that cause hystereses, as discussed earlier. Notably, the ratio of $CO_2$ to $CH_4$ is correctly described by the model, i.e. $\Delta h_{0,CO_2}/\Delta h_{0,CH_4} \approx \Delta h_{0,CO_2}^{LDFT}/\Delta h_{0,CH_4}^{LDFT} \approx 1.2 \pm 0.1$.

The enthalpy of adsorption can be obtained as a function of loading from the virial equation written in the following form (Czepirski and Jagiello, 1989):

$$\ln(P/n) = \frac{1}{T}\sum_{i=0}^{m_a} a_i n^i + \sum_{i=0}^{m_b} b_i n^i \tag{6.1}$$

where $a_i$ and $b_i$ are temperature-independent virial coefficients equivalent to the terms in Equation 5.8 in the following manner: $a_0/T + b_0 = -K_0$, $a_1/T + b_1 = -K_1$, and so on. The isosteric

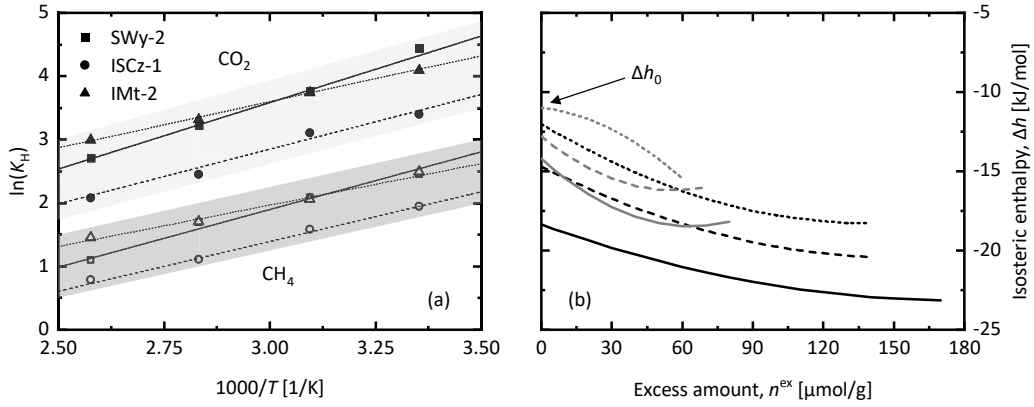



Figure 6.6: (a) $\ln(K_{\mathrm{H}})$ plotted against the inverse temperature, $1/T$, for $CO_2$ (closed symbols inside the light grey area) and $CH_4$ (open symbols inside the dark grey area). The lines (solid – SWy-2, dashed – ISCz-1, dotted – IMt-2) are linear fits to obtain the isosteric enthalpy of adsorption at zero coverage. (b) Isosteric enthalpy of adsorption of $CO_2$ (black lines) and $CH_4$ (grey lines) plotted against excess amount of adsorption.

enthalpy dependent on the loading amount can then be calculated from the following (Czepirski and Jagiello, 1989):

$$|\Delta h(n)| = -R\left[\frac{d\ln(P)}{d(1/T)}\right]_n = -R\sum_{i=0}^{m} a_i n^i \tag{6.2}$$

The experimental data have been described using Equation 6.1 ($m = n = 3$), where the zeroth-order virial coefficients ($a_0$ and $b_0$) were fixed due to their physicial significance known a priori in that $\Delta h_0 = R \cdot a_0$ and $K_{\mathrm{H}}^0 = \exp(-b_0)$. Figure 6.6b indicates that $|\Delta h|$ increases as a function of loading by approximately 5 to 6 kJ/mol and 3 to 4 kJ/mol for $CO_2$ and $CH_4$, respectively. This behavior is the result of increasing lateral adsorbate interactions on relatively homogeneous surfaces (Al-Muhtaseb and Ritter, 1999; Yuan et al., 2013; Murialdo et al., 2018) of clay minerals as opposed to heterogeneous shales that show decreasing $|\Delta h|$ for $CO_2$ and $CH_4$ (Duan et al., 2016). Notably, we do not observe the expected enhancement in the change of $|\Delta h|$ with loading due to molecular polarity (Ruthven, 1984), as $CO_2$ and $CH_4$ outline a similar behavior. This may partly be due to the limited range of densities used in the analysis.

The analysis of the adsorption energetics indicate that the three clay minerals are appropriate for enhanced $CH_4$ recovery through the injection of $CO_2$ as the released heat from $CO_2$ adsorption will lead to desorption of $CH_4$. The thermodynamic properties suggest that SWy-2 is most suited among the three clay minerals in this study for the application of $CO_2$ storage and enhanced recovery. The adsorption enthalpy indicates the strongest interaction with $CO_2$ and the highest average selectivity of $CO_2$ over $CH_4$. It should be highlighted that these conclusions apply to

a thoroughly dried clay. While in actual geological formations clays are hydrated, the effect of water on the total extent of adsorption of reservoir gases (and, accordingly, energetics) remains uncertain. Experimental studies have shown that water may either decrease the adsorption capacity by competitively occupying sorption sites or increase it by providing more accessible micropore volume, as a result of clay swelling (Schaef et al., 2015).

### 6.3.5 $CO_2$ and $CH_4$ in clay nanopores

The LDFT model provides insight into the uptake of supercritical $CO_2$ and $CH_4$ within clay nanopores including pore size-dependent adsorption behaviors and into the degree of pore occupancy of the supercritical adsorbed phase. Figure 6.7a shows the $CO_2$ excess adsorption isotherm on SWy-2 at 50 °C produced by the LDFT model with the individual contributions from each pore class, and Figure 6.7b to d show the lattice occupancy profiles for four selected pore classes. It can

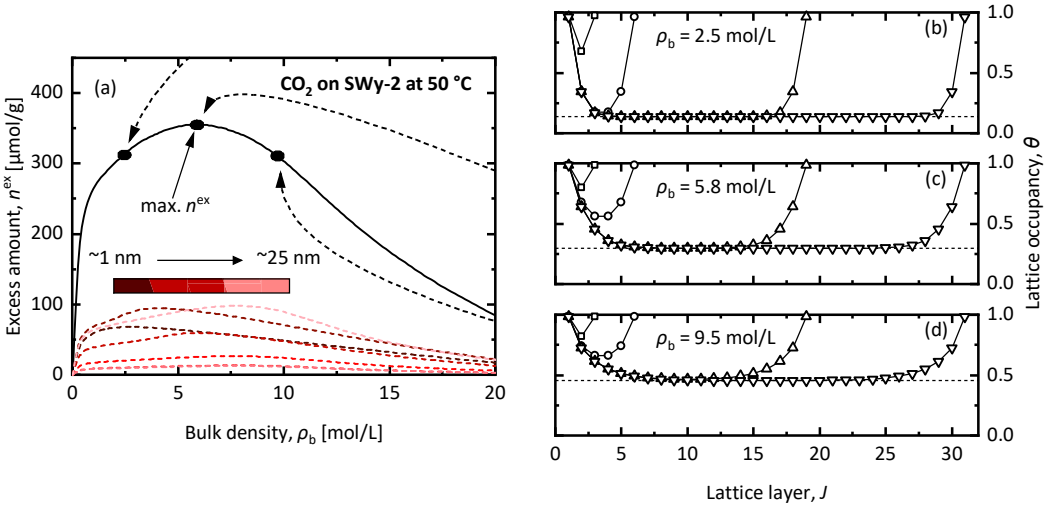



Figure 6.7: (a) $CO_2$ adsorption isotherm at 50 °C on SWy-2 (solid line) with isotherms of individual pores (dashed lines) in color. The pore sizes of the individual isotherms are indicated by the color scale. (b) – (d) Lattice occupancy profiles corresponding to three density values highlighted in (a) – maximum amount of adsorption, $n^{ex}{}_{max}$, and points before and after $n^{ex}{}_{max}$ with the same amount of excess adsorption – for the lattice pores with 3 (1.2 nm, square), 6 (2.4 nm, circle), 19 (7.6 nm, upward triangle), and 31 (12.4 nm, downward triangle) layers.

be seen that the adsorption process is controlled by pore filling (significant density enhancement above that of the bulk phase) up to small mesopores ($J = 6$, $< 2.5$ nm); for pores larger (upward and downward triangles), multiple layers are formed as the bulk density increases, while the center of the pore remains filled with bulk supercritical fluids. This observation of pore size-specific behavior compares well with the supercritical sorption mechanism shown by GCMC simulations

(Jin and Firoozabadi, 2013; Chen et al., 2016a, 2018) inside slit pores of clay minerals, in which the filling of adsorbate occurs for micropores while the adsorption layers on the surface dominate the adsorption behavior for larger mesopores. The observed difference in the extent of fluid densification inside pores suggests that supercritical adsorption on clay mineral surfaces should not be assessed using a single pore system.

Figure 6.8 shows the pore saturation factors, $c_{\mathrm{sat}}$, plotted against the reciprocal of reduced temperature, $T_{\mathrm{c}}/T$. It can be seen that $c_{\mathrm{sat}}$ increases linearly with values approaching unity as the critical temperature of the fluid is reached. This reduction as $T$ increases beyond $T_{\mathrm{c}}$ suggests that

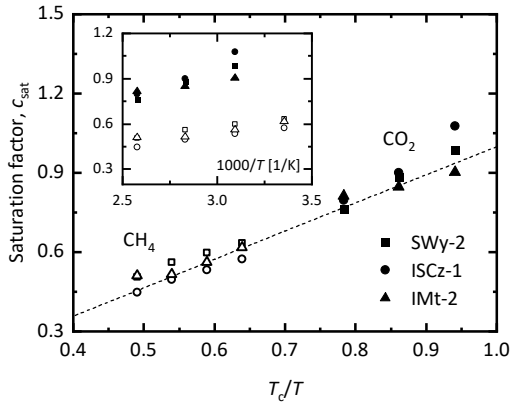



Figure 6.8: Saturation factors of $CO_2$ (closed symbols) and $CH_4$ (open symbols) as a function of $T_{\mathrm{c}}/T$. The inset plot shows the same values against $1/T$. The linear regression of the data shown in the plot can be described by the equation $c_{\mathrm{sat}} = 1.07(T_{\mathrm{c}}/T) - 0.07$. The value of $c_{\mathrm{sat}}$ of ISCz-1 at 50 °C was omitted in linear regression for the reason discussed in the main text, and the intercept was corrected to equate the value of $c_{\mathrm{sat}}$ to unity as $T_{\mathrm{c}}/T$ approaches unity.

the adsorbed fluid does not occupy the entire space of the pore volume at these conditions, and $c_{\mathrm{sat}}$ accounts for the temperature-dependent variability of the packing density in the LDFT model. Bénard and Chahine (1997) and Do (1998) similarly explained the phenomenon by attributing it to the compressibility and thermal expansion characteristics of the adsorbed phase that becomes greater above the critical temperature. It should be noted that the value of $c_{\mathrm{sat}}$ for $CO_2$ on ISCz-1 at 50 °C is above 1 although it is considered to be physically implausible by the definition provided in this study. This again highlights the difficulty to accurately measure the pore-size distributions of clay minerals and may indicate the enhanced accessibility of gases, such as $CO_2$, in clay nanopores. The most relevant observation is that the three clay minerals and the two gases outline a single characteristic line (Figure 6.8) suggesting that the degree of occupancy depends solely on temperature. This observation of temperature dependence drawn from multiple samples greatly extends the predictive capability of the model for supercritical adsorption on clay-bearing

geosorbents.

## 6.4 Concluding remarks

In this chapter, the workflow presented in Chapter 5 has been extended to three different clay minerals under dry conditions: Na-rich montmorillonite, illite-smectite mixed layer, and illite. The three clay minerals are characterized by distinct features of micro- and mesoporosity, for which the significance of conducting physisorption experiments using a combination of various gases ($N_2$, Ar, and $CO_2$) has been highlighted in this chapter. These structural properties are clearly manifested in the sorption isotherms of supercritical $CO_2$ and $CH_4$ on the three clay minerals, which are described well by the LDFT model. The LDFT model not only captures the isotherm features that arise from the varying porous properties of the three clay minerals, but also correctly models the relative quantities of enthalpy of adsorption for $CO_2$ and $CH_4$ that agree well with the values obtained from the experimental data. Lastly, the correlation between $c_{\mathrm{sat}}$ and $T_{\mathrm{c}}/T$ that was found solely for SWy-2 in the previous chapter has been further confirmed by the addition of ISCz-1 and IMt-2, and a linear relationship between the two quantities has been derived. The results presented in this chapter can be crucial in assessing the interaction of reservoir $CO_2$ and $CH_4$ with the microstructure of numerous geosorbents, which are likely to be dominated by mixtures of illite and smectite clay minerals, in the context of geoenergy applications.

# Chapter 7

# Supercritical sorption on hydrated clay minerals

Reprinted (adapted) with permission from Junyoung Hwang and Ronny Pini. Enhanced Sorption of Supercritical $CO_2$ and $CH_4$ in the Hydrated Interlayer Pores of Smectite. *Langmuir* 2021. Copyright 2021 American Chemical Society.

## 7.1 Introduction

The previous two chapters discussed the sorption of $CO_2$ and $CH_4$ on thoroughly dried clay minerals (dehydrated at 200 °C under continuous vacuum for over 12 h). However, a key factor in controlling the gas sorption capacities of clay-rich formations is the presence of water in the clay nanostructure, more specifically within the interlayer of swelling clay minerals, such as smectite. The hydration state of the interlayer in smectite clay minerals depends on the burial depth (Bird, 1984; Busch et al., 2016; Wentinck and Busch, 2017) and is classified as zero (0W, dehydrated), one (1W), two (2W), and three (3W) water molecular layer states (Mooney et al., 1952b; Bérend et al., 1995; Cases et al., 1997; Ferrage et al., 2005; Morodome and Kawamura, 2009). Although the width of the interlayer spacing of smectite clay minerals varies depending on the layer charge, size of the exchangeable cations, and relative humidity condition (Morodome and Kawamura, 2009; Salles et al., 2010), it generally demonstrates maximum expansion of approximately 4 Å to 6 Å from its initial dry state (0W) upon hydration. Such level of expansion is sufficient to generate

additional microporosity previously not accessible to surrounding gases and fluids. This notion is supported by the inability of gases, such as $N_2$ and Ar, to measure by physisorption the total surface area of expandable clay minerals, dominated by the interlayers that are only accessible to water (Tournassat et al., 2003; Środoń and McCarty, 2008) as briefly discussed previously in Section 5.5.2.

Recent experimental evidence (Giesting et al., 2012a; Ilton et al., 2012; Loring et al., 2012; Schaef et al., 2012; Rother et al., 2013; Loring et al., 2014; Schaef et al., 2015) supported by simulation studies (Myshakin et al., 2013; Makaremi et al., 2015; Loganathan et al., 2018) indicates that supercritical $CO_2$ molecules can access the interlayer spacing of smectite clay minerals in their appropriate hydration states. By exploiting advanced *in operando* techniques to probe the clay samples, these experimental studies have unequivocally shown that the intercalation of $CO_2$ in smectite peaks between sub-1W and 1W hydration states, and decreases at higher hydration states (Giesting et al., 2012b; Schaef et al., 2012; Rother et al., 2013; Loring et al., 2014; Schaef et al., 2015). This water saturation-dependent intercalation is likely to apply to other gases, such as $CH_4$, albeit only limited observations have been reported thus far (Bowers et al., 2018; Lee et al., 2018; Bowers et al., 2019). These studies suggest an increase in the uptake amount of $CO_2$ and $CH_4$ on clay minerals with hydrated interlayers, but the rigorous quantification of the sorption phenomenon is still lacking. For instance, molecular simulations of $CO_2$ and $CH_4$ adsorption on cla minerals in the presence of water have been mostly performed with fixed pore widths (Jin and Firoozabadi, 2014; Wang et al., 2019). While these studies indicate weaker sorption of $CO_2$ and $CH_4$ in clay nanopores as water molecules competitively occupy the sorption sites, questions remain on the applicability of observations that do not take into consideration the expansion of the clay interlayer. The comparison of published experimental data on wet clay minerals (Busch et al., 2008; Ji et al., 2012; Liu et al., 2013; Grekov et al., 2020; Ziemiański et al., 2020) indicates that the estimation of the adsorbed amount of either $CO_2$ or $CH_4$ is still affected by a large degree of uncertainty. A possible explanation for the disparity in the experimental results is the method of obtaining hydrated clay minerals, which has relied on using different degassing temperatures (leading to different hydrated states) rather than a systematic approach of hydration adopted for other materials, such as carbon (Billemont et al., 2011, 2013) or coal (Krooss et al., 2002; Kim et al., 2011). In the case of smectite clay minerals, accurate estimation of the water amount within the microstructure is crucial as different hydration states of smectite interlayers have varying, often opposite, effects on the adsorption capacity.

In this chapter, the effect of water on the adsorption of supercritical $CO_2$ and $CH_4$ on clay minerals under subsurface temperature and pressure conditions is quantified. The work performed to accomplish this objective is twofold. First, the water uptake capacity was measured at 20 °C up to 0.9 relative humidity (RH) for four source clay minerals, STx-1b (Ca-rich montmorillonite), SWy-2, ISCz-1, and IMt-2. In addition to revealing the truly accessible pore structure of the clays, the water sorption isotherms provide the means to assess the level of RH in the high-pressure adsorption experiments. Second, the single-component sorption isotherms of $CO_2$ and $CH_4$ were measured on STx-1b and IMt-2 up to 300 bar at 50 °C under dry and hydrated (RH of approximately 0.05) conditions. The non-expandable IMt-2 was used to serve as a reference that does not possess accessible interlayers. The sorption isotherms were modeled using the LDFT model to further quantify and validate the degree of pore-volume expansion in the hydrated clay interlayer.

## 7.2 Materials and experimental methods

The clay mineral samples, STx-1b, SWy-2, ISCz-1, and IMt-2, have been sourced from the Source Clay Repository of the Clay Minerals Society (Virginia, USA) and were ground and sieved to below particle size of 50 $\mu$m. These clay minerals can be roughly categorized as swelling (STx-1b and SWy-2) and non-swelling (ISCz-1 and IMt-2), although the partial smectite layer structure imparts some level of swelling to ISCz-1. The pure gases used in this study were obtained from BOC (Surrey, UK) at purities of 99.9992 % for $N_2$, 99.999 % for Ar and He, 99.995 % for $CO_2$, and 99.995 % for $CH_4$. Water was purified using PURELAB Chorus 1 (ELGA LabWater, High Wycombe, UK) to obtain 18.2 MΩ · cm resistivity. Water was degassed *ex situ* for 2 h under vacuum at 50 °C while being stirred and additionally degassed *in situ* for 30 min under vacuum before vapor sorption experiments.

### 7.2.1 Water sorption

Low-pressure adsorption and desorption of water vapor (at 293 K) on the clay mineral samples were measured using Autosorb iQ (Quantachrome Instruments, Florida, USA), which was also used to measure low-pressure sorption of $N_2$, Ar, and $CO_2$ as described in Section 6.2.1 (also performed for STx-1b in this chapter). The samples were degassed *ex situ* at 200 °C under vacuum for 12 h prior to the measurements. Experimental temperature of 293 K was obtained using a liquid circulating thermostat (Julabo CORIO CD-200F, Seelbach, Germany) with a bath containing a water-ethylene

glycol (50 vol%) mixture. The low-pressure data were used to estimate the BET surface area of both dry and hydrated samples, pore-size and pore-volume distributions (see Appendix A and C), as well as the unconstrained volumetric expansion of the pore volume upon water sorption.

### 7.2.2 High-pressure adsorption experiments

#### Dry samples

The high-pressure adsorption measurements of $CO_2$ and $CH_4$ have been performed for dry (degassed *in situ* at 200 °C for 12 h under continuous vacuum) STx-1b and IMt-2 in the pressure range of 0.02 to 30 MPa at 50 °C. It should be noted that freshly ground IMt-2 sample was used for the high-pressure sorption measurements in this chapter because the batch previously used for the results presented in Chapter 6 had been depleted (the high-pressure sorption data of $CO_2$ and $CH_4$ on the fresh batch of dry IMt-2 were newly measured for this chapter). While the new batch of IMt-2 differed slightly in its sorption capacities for $CO_2$ and $CH_4$, the effect of water on the sorption of $CO_2$ and $CH_4$ on non-swelling IMt-2 reported in this chapter is still valid.

#### Hydrated samples

The excess adsorbed amounts of $CO_2$ and $CH_4$ on hydrated STx-1b and IMt-2 (with pre-adsorbed water) have been measured in the pressure range of 0.5 to 17 MPa at 50 °C. These experiments were conducted only in adsorption mode under the assumption that water is not removed during the adsorption of $CO_2$ and $CH_4$, which has been demonstrated previously through simulation (Billemont et al., 2011; Jin and Firoozabadi, 2014) and experimental studies (Giesting et al., 2012a; Schaef et al., 2012). The sample was first degassed at 200 °C and hydrated using Autosorb iQ via adsorbing water up to RH of 0.9 as described in Section 7.2.1. The hydrated sample was transferred into the measuring chamber of the magnetic suspension balance where it was allowed to quickly equilibrate under vacuum at the experimental temperature of 50 °C *in situ* prior to adsorption measurements. This step allowed $MP_{1,0}$ (reference weight measured under vacuum) in Equation 3.1 to be obtained (equal to the sum of $m_s$ and the pre-adsorbed water mass, $m_w$), while extracting the air that was present inside the measuring chamber allowing pure adsorbate fluids to be introduced. Similar moisture-equilibrium procedures have been used to obtain an approximate state of ≤1W for Na- (Ilton et al., 2012) and Ca-montmorillonite (Schaef et al., 2012). However, this equilibration step inevitably removed excess amounts of the pre-adsorbed water, which does

not allow the value of $m_w$ to be known. Therefore, the samples were degassed again *in situ* under vacuum at 200 °C for 12 h to achieve complete dehydration after each adsorption isotherm measurement to obtain $m_s$. This degassing step allowed an accurate estimate of $m_w$ for each clay mineral samples (hence the RH in the measuring chamber) to be determined by subtracting the weight of the degassed sample from that of the hydrated sample. The specific molar amount of excess adsorbed fluid ($CO_2$ or $CH_4$) on the hydrated clay minerals is then calculated using the following equation:

$$n^{ex}(\rho, T) = \frac{MP_1(\rho, T) - MP_{1,0} + \rho_b(V_0 + V_w)}{M(m_s + m_w)} \tag{7.1}$$

We note that Equation 7.1 explicitly accounts for the volume of pre-adsorbed water, $V_w$. The sum $V_0 + V_w$ was determined again with helium as the probing gas assuming that the amount of pre-adsorbed water remains constant with the increasing helium pressure.

For the high-pressure adsorption experiments on hydrated STx-1b and IMt-2, three separate aliquots of each samples were prepared following the above experimental procedure. The first aliquot was probed by helium to determine the value of $V_0 + V_w$. The second and third aliquots were used to measure the amounts of excess adsorption of $CO_2$ and $CH_4$, respectively.

### 7.2.3 TGA

The thermogravimetric analysis (TGA) was performed using TGA Q500 (TA Instruments) to quantify the amount of water retained by as-received clay mineral samples by heating them up to 1000 °C at a rate of 10 °C/ min after equilibrating initially at 30 °C. The sample atmosphere was continuously purged with $N_2$ gas with a purge rate of 60 mL/ min.

### 7.2.4 XRD

The X-ray diffraction (XRD) patterns were collected using X'Pert Pro from PANalytical equipped with a copper anode ($\lambda = 1.54$ Å) for the four source clay mineral samples completely dehydrated (following the procedure described above) and for STx-1b with pre-adsorbed water to observe the change in $d_{001}$ spacing upon hydration. The measurements were collected from $2\,\theta$ of 5° to 60° with a scan step size of 0.03°. The values of $d_{001}$ spacing were calculated using the Bragg's Law.

## 7.3 Results and discussion

### 7.3.1 Water sorption isotherms

Figure 7.1a shows adsorption and desorption isotherms of water on the four source clay minerals at 20 °C up to 0.9 RH. The isotherms were measured at least twice with separate aliquots to confirm their reproducibility. All four clay minerals display hysteresis between adsorption and desorption isotherms. The amounts of water sorption uptake as a function of RH for each clay

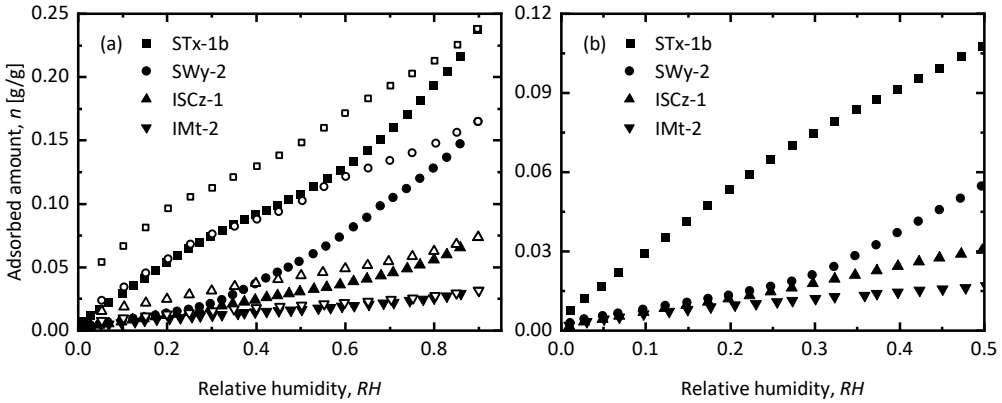



Figure 7.1: Water adsorption (closed symbols) and desorption (open symbols) isotherms on four source clay minerals at 293 K (a) up to 15.8 Torr (RH of 0.9) and (b) up to RH of 0.5 (only adsorption data are shown for visual clarity).

minerals closely follow the trend shown by TGA curves of the as-received clay minerals up to 200 °C shown in Figure 7.2. The TGA curves show that a significant weight loss, especially for smectite clay minerals (STx-1b and SWy-2), first occurs up to approximately 200 °C, at which the water present on the clay mineral surfaces is removed (dehydration). Another significant weight loss at approximately 500 °C to 600 °C corresponds to the removal of structural water (dehydroxylation) (Środoń and McCarty, 2008; Sanders et al., 2010; Che et al., 2011; Macht et al., 2011; Kuila and Prasad, 2013). The extent of dehydration (weight loss up to 200 °C) of the clay minerals follows the same order of total water uptake (STx-1b > SWy-2 > ISCz-1 > IMt-2) shown in Figure 7.1a, which indicates that water sorption up to RH of 0.9 is dominated by physisorption of surface water rather than chemisorption of structural water. The sorption isotherms of STx-1b and SWy-2 are in good agreement with the majority of previously reported data on Ca- and Na-montmorillonite samples (Bérend et al., 1995; Cases et al., 1997; Chiou and Rutherford, 1997; Likos and Lu, 2006, 2012; Thompson et al., 2014; Schaef et al., 2015). Fewer studies have been conducted on illite clay minerals and indicate much larger water uptake (> 20 wt% to 30 wt%) (Schuttlefield et al.,

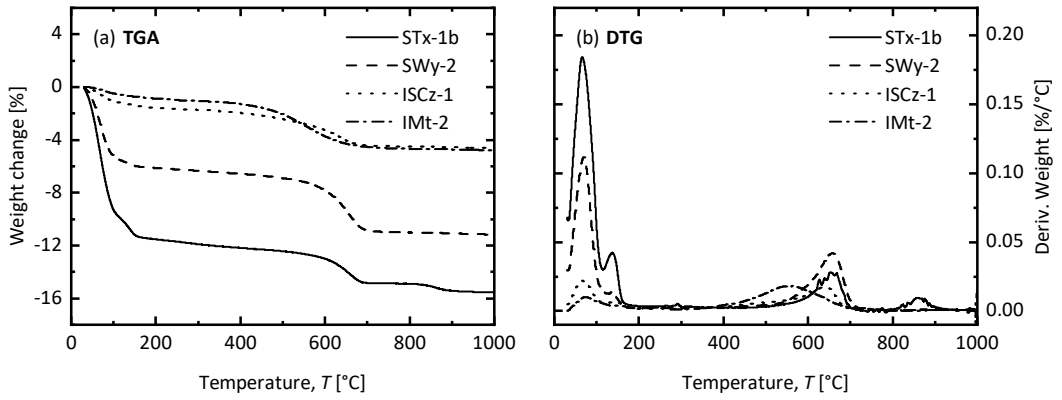



Figure 7.2: (a) TGA curves and (b) DTG curves that show two distinct regions of significant weight loss for all four clay minerals: one below 200 °C and another at approximately between 500 °C to 700 °C.

2007; Hatch et al., 2012). As discussed below, these are in disagreement with the smaller values of surface area and pore volume reported for illite clay (and the lack of interlayer expansion), further indicating that the trend in the total uptake amount from IMt-2 to STx-1b shown in Figure 7.1a is correct.

### Internal surface area

Table 7.1 summarizes the values of surface area obtained from the water isotherms in Figure 7.1 for the four clay minerals with the surface areas measured from $N_2$ and Ar physisorption measurements (see Figure C.1). It has been shown that $N_2$ and Ar gases only access the external surface area ($S_{\text{ext}}$) of clay minerals, while polar liquids, such as ethylene glycol monoethyl ether (EGME) or water, can be used to probe and quantify the internal surface area ($S_{\text{int}}$) (Cerato and Lutenegger, 2002; Środoń and McCarty, 2008; Macht et al., 2011). The use of different probing molecules is important for the characterization of expandable clays, such as smectite, because $S_{\text{ext}}$ is a small fraction of the theoretical surface area obtained from structural data (Mooney et al., 1952a; Quirk and Murray, 1999; Cerato and Lutenegger, 2002; Meunier, 2005; Środoń and McCarty, 2008; Kozlowski et al., 2014; Rother et al., 2013), which amounts to 700 $m^2/g$ to 800 $m^2/g$.

The values of $S_{\text{int}}$ reported in Table 7.1 have been calculated by applying a modified BET theory (Mooney et al., 1952a) that combines measurements of the external surface area (measured by Ar in this study) with the surface area obtained from the BET region of the water isotherms ($S_{\text{BET,w}}$, see Table 7.2):

$$S_{\text{int}} = 2(S_{\text{BET,w}} - S_{\text{ext}}) \tag{7.2}$$

Table 7.1: Surface area of clay samples measured by $N_2$, Ar, and $H_2O$ in comparison with literature values[†]

| Reference | Method | STx-1b | SWy-2 | ISCz-1 | IMt-2 |
|---|---|---|---|---|---|
| **Specific external surface area,** $S_{ext}$ [$m^2/g$] | | | | | |
| This study | $N_2$ | $100.77 \pm 0.19$ | $36.72 \pm 0.08$ | $32.59 \pm 0.08$ | $21.90 \pm 0.06$ |
| | Ar | $82.31 \pm 0.10$ | $33.14 \pm 0.21$ | $30.15 \pm 0.16$ | $19.82 \pm 0.08$ |
| Zhang et al. (2017) | $N_2$ | 96.56 | 25.42 | 31.96 | 19.74 |
| Joewondo (2018) | $N_2$ | – | 34.02 | 32.45 | $20.65^{(a)}$ |
| Van Olphen and Fripiat (1979) | $N_2$ | $83.79 \pm 0.22^{(b)}$ | $31.82 \pm 0.22$ | – | – |
| Busch et al. (2008) | $N_2$ | 92.3 | 28 | – | – |
| Sanders et al. (2010) | $N_2$ | 82.9 | 34 | – | – |
| Dogan et al. (2007) | $N_2$ | – | – | $34.3 \pm 1.76$ | $17.5 \pm 0.27$ |
| **Specific internal surface area,** $S_{int}$ [$m^2/g$] | | | | | |
| This study | $H_2O$ | $567.80 \pm 5.90$ | $540.75 \pm 7.78$ | $143.59 \pm 2.84$ | $50.06 \pm 0.68^{(c)}$ |
| Środoń and McCarty (2008)[(d)] | $H_2O$ | $691^{(b)}$ | $652^{(e)}$ | – | – |
| | EGME | $741^{(b)}$ | $748^{(e)}$ | – | – |
| Cerato and Lutenegger (2002)[(d)] | EGME | $534^{(b)}$ | 637 | – | – |
| Kraehenbuehl et al. (1987) | $H_2O$ | $589^{(b)}$ | – | – | – |

[†] The literature values have been obtained only for clay minerals sourced from the Clay Minerals Society.
[(a)] The value was measured for IMt-1, which is an illite clay mineral sample sourced from the same site as IMt-2 (Cambrian shale of Silver Hill, Montana, United States) (Dogan et al., 2007).
[(b)] The value was measured for STx-1. STx-1b was collected from the same site as STx-1 when STx-1 supplies were depleted (Sanders et al., 2010).
[(c)] The value was not calculated using the method proposed by Mooney et al. (1952b) given that water does not access the IMt-2 interlayer.
[(d)] The study reports total specific surface area.
[(e)] The value was measured for SWy-1. SWy-2 was collected from the same site as SWy-1 at a later occasion (`https://www.clays.org/sourceclays_data/`).

where the multiplication by 2 is based on the interpretation that the monolayer of water molecules that is formed inside the interlayer is in contact with both the upper and lower tetrahedral layers of the interlayer spacing. The resulting values of $S_{\text{int}}$ of STx-1b ($\sim$570 $\text{m}^2/\text{g}$) and SWy-2 ($\sim$540 $\text{m}^2/\text{g}$) are close to the theoretical surface area of smectite clay minerals and are in agreement with values reported in the literature for water and EGME (see Table 7.1). These are also much larger than the values obtained by using either Ar or $N_2$, namely $S_{\text{ext}}$ ranging from 80 $\text{m}^2/\text{g}$ to 100 $\text{m}^2/\text{g}$ for STx-1b and 30 $\text{m}^2/\text{g}$ to 40 $\text{m}^2/\text{g}$ for SWy-2. The value of $S_{\text{int}}$ of ISCz-1 amounts to approximately 25 % of those of STx-1b and SWy-2. Yet, the substantial increase of $S_{\text{int}}$ relative to $S_{\text{ext}}$ demonstrates partial interlayer accessibility in the mixed layers of illite-smectite (30 wt% smectite content). Interestingly, the value of $S_{\text{int}}$ of IMt-2 (50 $\text{m}^2/\text{g}$) also shows 133 % to 155 % increase from $S_{\text{ext}}$ ($N_2$ and Ar) despite its non-swelling nature. This observed increase may be due to the filling of small interparticle micropores that are accessible to water molecules, but inaccessible to $N_2$ and Ar gases (Deeds and Van Olphen, 1961a; Hatch et al., 2012). Nonetheless, the internal surface area is still much smaller than values observed for the other three clay minerals, confirming that the interlayer is precluded to water.

Table 7.2: BET surface areas, $S_{\text{BET,w}}$, calculated from water adsorption and desorption isotherms

| Surface area | Unit | STx-1b | SWy-2 | ISCz-1 | IMt-2 |
|---|---|---|---|---|---|
| Adsorption | [$\text{m}^2/\text{g}$] | 345.22 | 74.91 | 69.12 | 43.39 |
| Desorption | [$\text{m}^2/\text{g}$] | 366.21 | 303.51 | 101.95 | 50.06 |
| Ratio[†] | [-] | 0.94 | 0.25 | 0.68 | 0.87 |

[†] The ratio between the values of surface area obtained from the adsorption and desorption isotherms.

We note that the assumption of monolayer formation has been questioned in the application of the BET theory to water sorption on clay minerals because the water molecules in the interlayers will tend to cluster around cations (Quirk, 1955). However, the fundamental BET parameters are generally fulfilled, particularly for the desorption curves, and the linear BET regions are well established (see Appendix A). The evident disparity between $S_{\text{BET,w}}$ values obtained from adsorption and desorption curves on SWy-2 (Table 7.2) is consistent with the interpretation that water adsorption occurs mainly on the external surface in the BET range ($0.05 < \text{RH} < 0.35$), within which a single hydrate layer is still present during dehydration (Cases et al., 1992).

**Interlayer expansion of smectite clay minerals**

The larger total uptake of water shown in Figure 7.1 on STx-1b and SWy-2 compared to ISCz-1 and IMt-2 is attributed to water sorption in the smectite interlayer. Notably, the resulting expansion of the clay framework as RH increases produces isotherm shapes that do not conform to any isotherm types classified by the recent IUPAC report (Thommes et al., 2015). On the contrary, the amount of uptake for illite-dominated clay minerals is limited to sorption in interparticle pores and on the external surface (Dettmann, 1958; Grekov et al., 2019); the resulting isotherm follows the IUPAC Type II isotherm that is characteristic of multilayer adsorption. The isotherm of ISCz-1, illite-smectite mixed layer, shows the distinctive characteristics of both the SWy-2 and IMt-2 isotherms, resulting in higher water uptake than IMt-2 over the entire RH range. Since interlayer expansion causes a greater adsorbed volume of water compared to that of $N_2$ or Ar, we propose to express the extent of volumetric swelling, $s$, as the difference between the accessible pore volume estimated from the adsorbed volumes of water ($\tilde{v}_\mathrm{w}$) and Ar ($\tilde{v}_\mathrm{g}$) at equivalent partial pressures:

$$s = \rho_\mathrm{b}(\tilde{v}_\mathrm{w} - \tilde{v}_\mathrm{g}) \tag{7.3}$$

where the clay bulk density, $\rho_\mathrm{b}$, is obtained from the following expression:

$$\frac{1}{\rho_\mathrm{b}} = v_\mathrm{g} + \frac{1}{\rho_\mathrm{sk}} \tag{7.4}$$

where $v_\mathrm{g}$ is the total specific pore volume estimated by the adsorbed volume of Ar at relative pressure of 0.9, and $\rho_\mathrm{sk}$ is the skeletal density measured by He gravimetry. The resulting values of $s$ shown in Figure 7.3b demonstrate a gradual increase of $s$ with RH, reaching maximum values of 24 % (STx-1b), 34 % (SWy-2), 10 % (ISCz-1) and 4 % (IMt-2). We discuss in the following the analogy between the behavior outlined by $s$ and independent literature measurements of the $d_{001}$ spacing as a function of RH.

Adsorption of water on Na-montmorillonite has been shown to occur first on the external surface at low water content (RH $< 0.25$) followed by stepwise hydration of the interlayer at higher RH (Cases et al., 1992; Bérend et al., 1995; Frinak et al., 2005; Hatch et al., 2012). The similarity in the uptake amounts between SWy-2 and ISCz-1 in the low RH region (Figure 7.1b) is the result of their similar external surface area (approximately 30 $\mathrm{m^2/g}$, see Table 7.1), and confirms that water adsorption on SWy-2 up to RH $\approx 0.25$ is dominated by the external surface (interlayer sorption of water is limited for ISCz-1 over the entire RH range). The onset of water sorption

inside the SWy-2 interlayer is manifested in the sharp increase in the uptake amount at RH $\approx 0.3$, producing a departure from the isotherms of ISCz-1 and IMt-2. This onset of interlayer sorption closely aligns with the stepwise increase of the $d_{001}$ spacing of Na-montmorillonite (Sato et al., 1992; Morodome and Kawamura, 2009; Loring et al., 2014), as shown in Figure 7.3a. Notably, the volumetric swelling isotherm shown in Figure 7.3b for SWy-2 also increases more rapidly at the RH level of approximately 30 %.

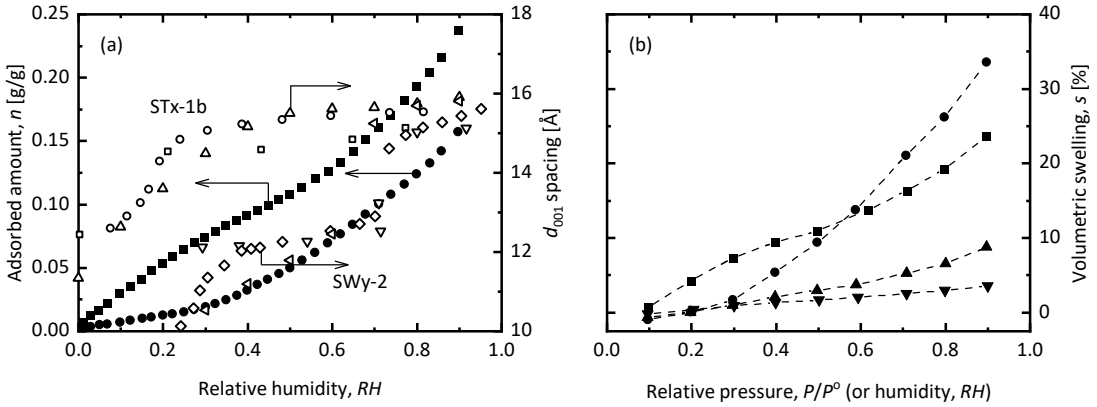



Figure 7.3: (a) Water adsorption isotherms of STx-1b and SWy-2 (closed symbols, left $y$-axis, indicated by arrows) from Figure 7.1a and $d_{001}$ spacing (open symbols, right $y$-axis, indicated by arrows) collected from the literature. For STx-1b, the squares are from Schaef et al. (2015) (50 °C and 90 bar), the circles are from Morodome and Kawamura (2009) (50 °C), and the upward triangles are from Sato et al. (1992). For SWy-2, the downward triangles are from Loring et al. (2014) (50 °C and 90 bar), the diamonds are from Morodome and Kawamura (2009) (50 °C), and left triangles are from Sato et al. (1992). (b) Unconstrained volumetric swelling obtained from the difference between the accessible pore volumes estimated from the adsorption isotherms of water and Ar.

In contrast, STx-1b shows significantly larger water uptake in the low RH region than SWy-2 (Figure 7.3a) and the isotherm does not exhibit a convex shape as for SWy-2. This adsorption behavior can be ascribed to the larger external surface area of STx-1b (approximately 80 $m^2/g$ to 100 $m^2/g$, see Table 7.1) if the hydration of Ca-montmorillonite is assumed to follow the same mechanism as Na-montmorillonite. Remarkably, $d_{001}$ spacing of Ca-montmorillonite also shows an immediate and gradual increase in the low RH region (Mooney et al., 1952b; Sato et al., 1992; Cases et al., 1997; Morodome and Kawamura, 2009; Schaef et al., 2015), indicating an earlier onset of interlayer sorption, too. Again, the swelling isotherm computed for STx-1b (Figure 7.3b) closely mimics this behavior, confirming the validity of our proposed approach to estimate interlayer expansion. The difference in the hydration mechanisms between STx-1b and SWy-2 can primarily be attributed to the greater hydration energy of $Ca^{2+}$ than that of $Na^+$ (1505 kJ/mol and 365 kJ/mol, respectively (Marcus, 1994)) and the larger initial $d_{001}$ spacing of $Ca^{2+}$ bearing clay minerals (Xu et al., 2000)

(measured values of $d_{001}$ spacing of dry STx-1b and SWy-2 are 11.3 Å and 9.71 Å, respectively, see Figure 7.4), which indicates a lower energy of layer separation for STx-1b. The larger initial $d_{001}$ spacing is also reflected in the smaller cumulative volumetric swelling of STx-1b compared to SWy-2 in Figure 7.3b, as the final $d_{001}$ spacing at RH of 0.9 is approximately equal at 16 Å for both montmorillonites.

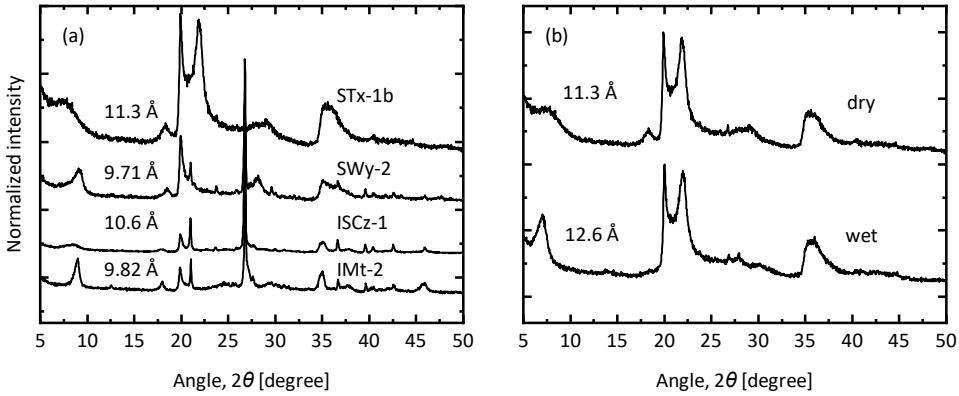



Figure 7.4: (a) XRD patterns of the four clay minerals after being completely dried at 200 °C and (b) XRD patterns of dry and hydrated STx-1b.

The comparability of the desorption isotherms of STx-1b and SWy-2 shown in Figure 7.5 demonstrates that the hydration mechanisms discussed above are not fully reversible during dehydration, which causes the hysteresis loop of SWy-2 to be larger than that of STx-1b, a common observation between the two montmorillonite samples (Bérend et al., 1995; Cases et al., 1997; Xu et al., 2000). The parallel trend between desorption of STx-1b and SWy-2 shown in Figure 7.5a indicates that dehydration steps, in which the water adsorbed on the external surface is removed first and the interlayer water remains until low RH due to the relatively strong hydration energy of the cations (Cases et al., 1992), are equally applied to STx-1b and SWy-2. This similarity is again validated by the evolution of volumetric swelling shown in Figure 7.5b especially below RH $\leq 0.4$.

### 7.3.2 Supercritical $CO_2$ and $CH_4$ adsorption

To investigate the effect of the expanded smectite interlayer and available internal surface area in the presence of water on the supercritical uptake amount of $CO_2$ and $CH_4$, excess adsorption of $CO_2$ and $CH_4$ on STx-1b and IMt-2 were measured under dry and hydrated conditions; IMt-2 was used as a non-swelling reference material.

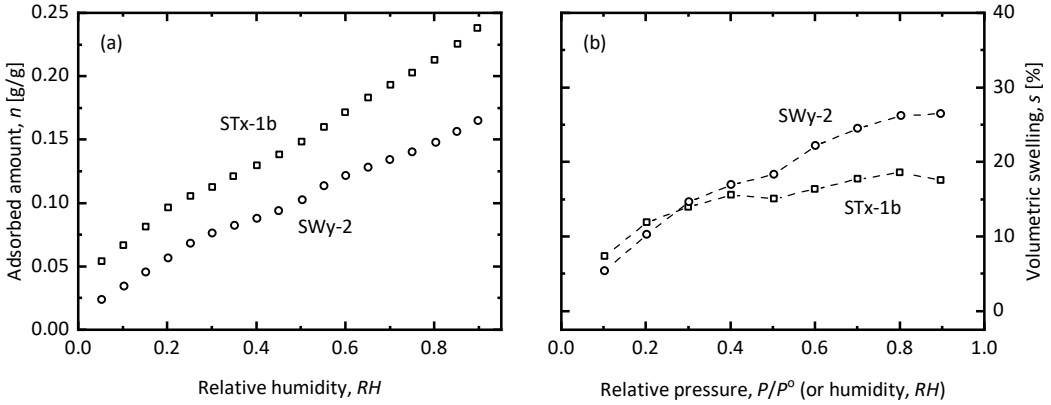



Figure 7.5: (a) Desorption isotherms of STx-1b and SWy-2 and (b) unconstrained volumetric swelling obtained from the desorption isotherms of water and Ar.

### Pre-adsorbed water

Table 7.3 summarizes the values of the skeletal density, $\rho_{\mathrm{sk}}$, of dry and hydrated STx-1b and IMt-2 (obtained by He gravimetry), and the amounts of pre-adsorbed water directly obtained from the difference in the measured weights of hydrated and dry clay minerals (dried at 200 °C after each isotherm experiments). The values of $\rho_{\mathrm{sk}}$ of STx-1b show 6 % decrease from its dry to hydrated

Table 7.3: Skeletal density of dry and hydrated STx-1b and IMt-2 and the amount of pre-adsorbed water obtained from the difference between the measured weight of hydrated and dry samples (degassed at 200 °C after each experiments)

| Property | Unit | STx-1b | IMt-2[†] |
|---|---|---|---|
| $\rho_{\mathrm{sk,dry}}$ | [g/cm$^3$] | $2.543 \pm 0.006$ | $2.838 \pm 0.005$ |
| $\rho_{\mathrm{sk,hydrated}}$ | [g/cm$^3$] | $2.398 \pm 0.008$ | $2.839 \pm 0.005$ |
| $m_{\mathrm{w,He}}$ | [g/g] | 0.037 | 0.006 |
| $m_{\mathrm{w,CO_2}}$ | [g/g] | 0.049 | 0.007 |
| $m_{\mathrm{w,CH_4}}$ | [g/g] | 0.047 | 0.006 |

[†] The value of $\rho_{\mathrm{sk}}$ for dry IMt-2 differs from that reported in Hwang and Pini (2019) because a new batch of IMt-2 sample was used for high-pressure adsorption measurements reported in this study.

state, indicating that pre-adsorbed water on STx-1b amounts to $0.042 \pm 0.004$ g/g (assuming that the change in $\rho_{\mathrm{sk}}$ is solely due to the presence of liquid water with density of 1 g/cm$^3$). The calculated value is in excellent agreement with the average of the measured weights of pre-adsorbed water of $0.044 \pm 0.006$ g/g determined from degassing the sample after each experiment (He, $CO_2$, and $CH_4$). We note that the difference between each of the individual measurements reported in Table 7.3 results in small deviations in the corresponding RH condition. The desorption curves

shown in Figure 7.1a are used to estimate the RH as approximately 0.05, at which STx-1b exists in partially hydrated sub-1W state. While the pre-adsorbed water on IMt-2 could not be calculated in the same way as the values of $\rho_{sk}$ remain unchanged within the range of measurement uncertainty for IMt-2, the measured weight of pre-adsorbed water is 0.006 g/g, which is significantly less than that of STx-1b as anticipated from its lower sorption uptake of water.

### Adsorption of $CO_2$ and $CH_4$ on dry and hydrated STx-1b and IMt-2

Figure 7.6 shows the high-pressure excess sorption isotherms of $CO_2$ and $CH_4$ on STx-1b and IMt-2 measured at 50 °C under dry and hydrated conditions. Expectedly, the larger external surface area and total pore volume lead to much greater amounts of sorption of $CO_2$ and $CH_4$ on dry STx-1b ($n^{ex}_{max}$ = 1.16 mmol/g and $n^{ex}_{max}$ = 0.39 mmol/g for $CO_2$ and $CH_4$, respectively) in comparison to the amounts of sorption on the other clay minerals that have been reported in Chapter 6. Most importantly, we observe that the excess adsorption amounts of both $CO_2$ and

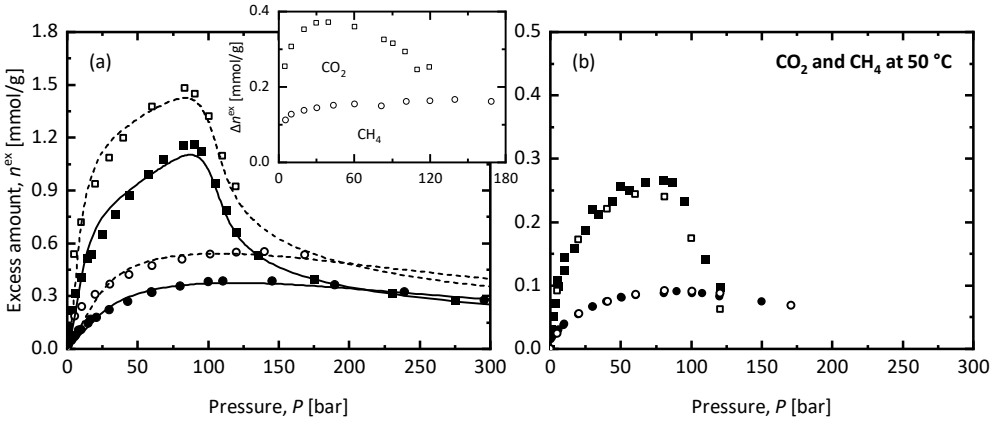



Figure 7.6: Excess sorption isotherms of $CO_2$ (squares) and $CH_4$ (circles) on (a) STx-1b and (b) IMt-2 under dry (closed symbols) and hydrated (open symbols) conditions at 50 °C. The inset of (a) shows the difference in the excess amounts of sorption between dry and hydrated STx-1b ($\Delta n^{ex} = n^{ex}_{hyd} - n^{ex}_{dry}$) plotted against pressure. No distinction was made between adsorption and desorption points for dry clay minerals, and error bars were omitted for visual clarity. The values of uncertainty were below 0.029 mmol/g and 0.014 mmol/g for $CO_2$ and $CH_4$, respectively, on STx-1b and 0.014 mmol/g and 0.010 mmol/g, respectively on IMt-2.

$CH_4$ are greater on hydrated STx-1b compared to its dry state over the entire pressure range investigated ($P \leq 150$ bar), while the difference between dry and hydrated IMt-2 is insignificant. As shown in the inset of Figure 7.6a, at a pressure of approximately 30 bar, the excess amount adsorbed on the hydrated STx-1b exceeds the value on dry STx-1b by $\Delta n^{ex} = 0.37$ mmol/g ($\sim 50$ % relative increase) for $CO_2$ and by $\Delta n^{ex} = 0.13$ mmol/g ($\sim 65$ % relative increase) for $CH_4$. The lack

of change in the adsorption amount observed for IMt-2 is equally interesting because it suggests that the small amount of pre-adsorbed water in the microstructure of IMt-2 is mainly located inside the interparticle micropores of IMt-2, which appear to be inaccessible to both $CO_2$ and $CH_4$ molecules under dry conditions. This characteristic interparticle pore accessibility in IMt-2 is in line with our interpretation of the larger surface area obtained from water than that of either $N_2$ or Ar (see Table 7.1). We note that the increase in the adsorbed amounts observed on hydrated STx-1b greatly exceeds the solubility of $CO_2$ and $CH_4$ in water (conservatively estimated to be 0.064 mmol/g and 0.006 mmol/g, respectively, at 50 °C and 200 bar) (Duan et al., 2006; Ou et al., 2015), in agreement with recent simulation studies by Makaremi et al. (2015). The increase seen equally for both $CO_2$ and $CH_4$ also precludes the possible formation of carbonate species speculated for clay surface (Cole et al., 2010; Giesting et al., 2012b,a) or zeolite (Baltrusaitis et al., 2007). This conclusion is also supported via the observation of reversible sorption process (Rother et al., 2013) and the NMR and IR spectroscopy measurements (Loring et al., 2012, 2014).

The enhanced sorption uptake of STx-1b for both $CO_2$ and $CH_4$ in the presence of water is attributed to the increased microporosity caused by the expansion of the interlayer pores that arises from the aforementioned sub-1W hydrated state. At the given RH and hydrated state, the $d_{001}$ spacing of Ca-montmorillonite expands to approximately $> 12.5$ Å (Mooney et al., 1952b) (confirmed by our own value of $d_{001}$ spacing equal to 12.6 Å as measured by *ex situ* XRD, see Figure 7.4), giving rise to an interlayer spacing of approximately $> 3.5$ Å (TOT layer thickness = 9 Å (Rother et al., 2013; Lainé et al., 2017; Wan et al., 2018)). In this expanded state, the interlayer may accommodate $CO_2$ and $CH_4$ molecules without any further interlayer swelling as demonstrated by the schematic representation in Figure 7.7. While previous studies have documented $CO_2$ and $CH_4$ intercalation in Ca-montmorillonite interlayer for sub-1W state with a minimum required $d_{001}$ spacing of approximately 11.5 Å (Schaef et al., 2012; Bowers et al., 2018; Lee et al., 2018), we provide here a direct quantification of this phenomenon in terms of the amount of $CO_2$ and $CH_4$ sorption. Remarkably, our measurements in Figure 7.6a (inset) show that the enhancement in $CO_2$ sorption increases with pressure, while it remains fairly constant for $CH_4$. These results are again in agreement with the previous notion of subsequent interlayer swelling due to $CO_2$ intercalation (Giesting et al., 2012a,b; Schaef et al., 2012; Rother et al., 2013), as opposed to the negligible change in the $d_{001}$ spacing from $CH_4$ intercalation (Bowers et al., 2018, 2019). We emphasize here the importance of determining the hydrated state through independent water sorption isotherms in interpreting the $CO_2$ and $CH_4$ sorption isotherms of hydrated clay minerals. Such interpretation

possibly explains the contrasting observation of decreased $CO_2$ and $CH_4$ sorption on hydrated montmorillonite samples (Busch et al., 2008; Liu et al., 2013) where the hydrated states were simply obtained from using different degassing conditions and may vary from the favorable sub-1W state.

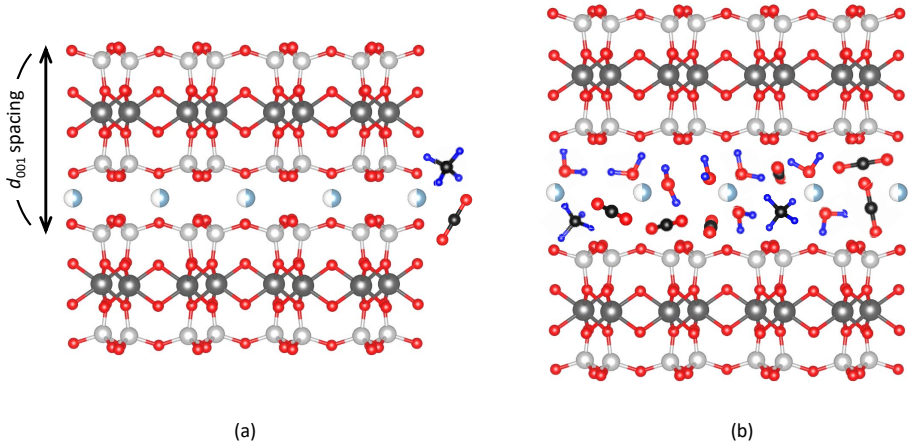



Figure 7.7: Schematic representation of the STx-1b interlayer under (a) dry and (b) hydrated conditions. The atoms are color coded as such, blue is hydrogen, red is oxygen, silicon is light gray, aluminum is dark gray, black is carbon, and white and light blue is calcium. The schematic of the STx-1b layers was taken from the structure of Ca-montmorillonite (STx-1) obtained from Downs and Hall-Wallace (2003), documented by Viani et al. (2002), and visualized using VESTA (Momma and Izumi, 2011). The basal spacing ($d_{001}$ spacing) is the sum of the interlayer spacing and the T-O-T layer.

### Pore volume expansion

We have applied the LDFT model to describe the sorption of supercritical $CO_2$ and $CH_4$ on dry STx-1b and used it to quantify the change in pore volume caused by the swelling of the interlayer pores in hydrated STx-1b. The model results are plotted in Figure 7.6a alongside the experimental data and show excellent agreement. As described in Chapter 4, a key distinctive feature of the LDFT model is the description of the adsorption process on a pore-by-pore level, which is informed by the knowledge of independent measurements of the pore-size distributions and pore volumes (determined from Ar and $CO_2$ physisorption measurements on dry STx-1b, see Appendix C). To reproduce the increase in the micropore volume due to interlayer expansion, a single micropore with a width of 0.8 nm (two lattice layers) was added to the original pore-size distribution of STx-1b. The amount of additional microporosity was used as an additional fitting parameter to obtain a good agreement between the LDFT model and the experimental data for hydrated STx-1b. The

remaining model parameters, namely the solid-fluid interaction energy ($\epsilon_{sf}/k$), the lattice fluid maximum packing density ($\rho_{max}$) and the "dry" discretized pore-size distributions have been kept the same between dry and hydrated STx-1b.

Table 7.4: LDFT model parameters

| Parameter | $\epsilon_{sf}/k$ | $\rho_{max}$ | $c_{sat}$ | $\Delta v_{pore}$ |
|---|---|---|---|---|
| | [K] | [mol/L] | [-] | [$cm^3/g$] |
| $CO_2$ | −965.30 | 26.51 | 1.00 | 0.016 |
| $CH_4$ | −797.39 | 26.43 | 0.54 | 0.017 |

The model parameters obtained from fitting the LDFT model to the experimental data are summarized in Table 7.4. The stronger interaction observed for $CO_2$ ($\epsilon_{sf}/k = -965.30\,K$) as compared to $CH_4$ ($\epsilon_{sf}/k = -797.39\,K$) and the similar values of the packing density of the two gases ($\rho_{max} = 26.45\,mol/L$) support our previous model findings on SWy-2, ISCz-1, and IMt-2 in Chapter 6. The values of $c_{sat}$, which is the saturation factor that accounts for the temperature-dependent variability of the packing density, are 1.00 and 0.54 for $CO_2$ and $CH_4$, respectively, at 50 °C. Again, these values conform well to the linear temperature-dependent correlation ($c_{sat} = 1.07(T_c/T) - 0.07$) shown in Figure 6.8.

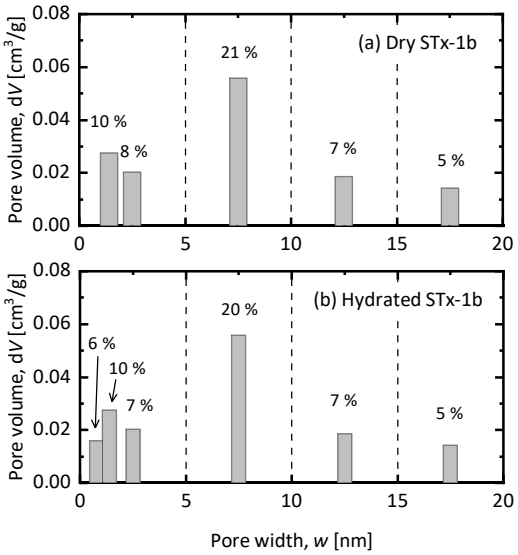



Figure 7.8: Discretized pore volume distributions of (a) dry and (b) hydrated STx-1b used as input parameters for the LDFT model. The extra bar in (b) represents the extra pore volume of $0.017\,cm^3/g$ contributed by interlayer expansion.

As shown in Figure 7.8 and reported in Table 7.4, the added micropore volumes, $\Delta v_{pore}$, were calculated to be $0.016\,cm^3/g$ and $0.017\,cm^3/g$ for $CO_2$ and $CH_4$, respectively, which is approximately

6 % of the total pore volume ($v_{\text{pore}} = 0.268\,\text{cm}^3/\text{g}$) estimated from the analysis of the low-pressure physisorption data. The similarity of the $\Delta v_{\text{pore}}$ values for the simulations conducted using $CO_2$ and $CH_4$ is expected, given that the expansion of the interlayer is largely caused by the sorption of water. While the additional pore volumes represent the void space filled by $CO_2$ and $CH_4$ molecules in the interlayer, it is noteworthy that the increase in pore volume compares well with the volumetric swelling of STx-1b at RH of 0.1 (7.3 %) calculated from the desorption branch (the comparison is made with the desorption branch since the pre-adsorbed water is obtained from a procedure that resembles the desorption of water) as can be seen in Figure S4b. This consistency again confirms that the enhanced sorption of $CO_2$ and $CH_4$ is owed to the interlayer accessibility introduced by water molecules, which is substantial enough to compensate for the reduction in the amount of $CO_2$ and $CH_4$ adsorption due to competitive adsorption with water.

## 7.4 Concluding remarks

The chapter has presented an experimental approach to quantify single-component gas uptake in hydrated clay minerals by profitably combining two distinct techniques: water physisorption analysis and high-pressure gas sorption. The high-pressure experiments were conducted at 50 °C and RH $\approx 0.05$, and demonstrated enhanced sorption capacities of supercritical $CO_2$ and $CH_4$ in STx-1b (Ca-rich montmorillonite) and non-competitive sorption of the same gases with water in IMt-2 (illite). While they are consistent with the previously observed phenomenon of $CO_2/CH_4$ intercalation into smectite interlayers most favored at sub-1W state, our results quantify the observation in terms of the amount of sorption. These results contrast with simulation studies on clays at the molecular scale (Jin and Firoozabadi, 2014; Kadoura et al., 2016; Wang et al., 2019) and experimental observations made from other gas/solid systems (Billemont et al., 2011; Kim et al., 2011; Lee et al., 2013), which indicate competitve sorption between water and $CO_2/CH_4$. The enhanced sorption is a result of increased microporosity and accessible internal surface area for the smectite clay mineral that arise from the interlayer expansion in the presence of water as demonstrated by water sorption isotherms and further confirmed by X-ray diffraction measurements showing increased $d_{001}$ spacing. Therefore, the findings of this study provide empirical basis for estimating the storage capacity of $CO_2$ and natural gas for formations rich in clay layers likely to exist with water present in their microstructures. While the present work quantified the amount of $CO_2$ and $CH_4$ interlayer sorption under sub-1W hydrated state, further work involving *in situ* hydration technique that enables precise control over the amount of pre-adsorbed water

is of interest to examine and quantify the dependence of uptake on varying hydration states (see Section 8.2.3).

# Chapter 8

# Conclusion and future work

## 8.1 Concluding remarks

In this thesis, we have employed a combined experimental and modeling approach to study sorption mechanisms of $CO_2$ and $CH_4$ on clay minerals in the context of geological $CO_2$ storage and unconventional hydrocarbon recovery. The workflow of measuring and modeling sorption of supercritical fluids on clay minerals was developed using Na-montmorillonite (smectite clay mineral) as a representative clay sample in Chapter 5 and extended to illite-smectite mixed layer and illite in Chapter 6. Adsorption and desorption at elevated temperature and pressure conditions were measured gravimetrically using a magnetic suspension balance as described in Chapter 3. The determination of the uncertainty values associated with the experimental measurements was highlighted in this study in view of the disparity among the scattered data sets of sorption on clay minerals observed in the literature. The instrument's measurement accuracy was additionally validated by reproducing the isotherms of two reference systems, $CO_2$/ZSM-5 and $CH_4$/zeolite Y, reported by NIST within their uncertainty values as discussed in Chapter 3. The stronger adsorption affinity of $CO_2$ compared to that of $CH_4$ was demonstrated for all three types of clay minerals as quantified by the selectivity ($K_{\mathrm{H,CO_2}}/K_{\mathrm{H,CH_4}} = 3.6 - 7.4$) and the adsorption energetics ($\Delta h_{0,\mathrm{CO_2}}/\Delta h_{0,\mathrm{CH_4}} = 1.2 - 1.3$) extracted from the experimental isotherms. These values were well-reproduced by the surface-fluid interaction energies obtained from the LDFT model, the isotherms of which also show excellent agreement with the experimental sorption isotherms. By taking into consideration the porous structure of the clay minerals, the LDFT model provided insights into the pore-size dependent behaviors of adsorption inside clay nanopores showing good

comparison with the results of GCMC simulations, while being computationally less burdensome. The correlation found between $c_{sat}$ and temperature shows that the occupancy of fluids inside pore volumes is dependent on temperature and pores become less and less saturated as the temperature increases beyond the fluid critical temperature. This observation is significant in assessing the sorption capacity for $CO_2$ and hydrocarbons under supercritical conditions and demonstrates that the model can be predictive.

The adsorption of $CO_2$ and $CH_4$ on clay minerals impacted by their hydration states was also quantified in Chapter 7. Two clay minerals were studied in this context: Ca-montmorillonite and illite, each representing swelling and non-swelling clay minerals, respectively. The results shown in Chapter 7 provided direct experimental evidence of increased sorption amounts of $CO_2$ and $CH_4$ for Ca-montmorillonite with pre-adsorbed water as compared to its dry state (approximately 50 % to 65 % relative increase). In the case of illite, however, the presence of water led to insignificant change in its sorption capacity not showing any competitive adsorption between water and $CO_2/CH_4$. We concluded that the enhanced sorption of Ca-montmorillonite is attributed to the expansion of its interlayers under sub-1W hydration state, which provides additional micropore volume that was inaccessible under dry conditions. The water sorption isotherms of Na- and Ca-montmorillonite also validated the presence of surface area of swelling clays only assessed by water; the values estimated are approximately an order of magnitude larger than those determined by $N_2$ or Ar physisorption. The micropore volume created by the interlayer expansion was quantified using the LDFT model, which showed 6 % increase in the total pore volume.

In conclusion, the experimental data and modeling analysis presented in this thesis provide qualitative and quantitative description of the sorption of supercritical $CO_2$ and $CH_4$ on three main types of dry and hydrated clay minerals – smectite, illite-smectite mixed layers, and illite – that appear most abundantly in natural subsurface environments. The experimental data present significant implications in studying subsurface fluid interactions in clay-rich systems. Furthermore, the successful application of the LDFT model to describe sorption on clay minerals has demonstrated a significant departure from conventional empirical adsorption models, such as the Langmuir model, the key assumptions of which have shown to be inapplicable for adsorbent materials characterized by a complex and wide range of porosity, such as clay minerals.

## 8.2 Future work

In this section, I summarize four independent research projects that I had hoped to explore during my study at Imperial College London, but were left incomplete. These research opportunities focus on challenging experimental work that may further address the knowledge gaps still present in the literature in evaluating the interactions between supercritical fluids and clay minerals under various conditions.

### 8.2.1 Workflow application to clay-rich rocks

The workflow of measuring and modeling supercritical sorption on clay minerals can be applied to clay-rich rocks that make up geological formations. Opalinus Clay is considered as a potential host site for geological disposal of nuclear waste in Switzerland (Delage et al., 2010; Minardi et al., 2016), and is a good analogue material for simulating $CO_2$ leakage through the caprock seals (Goodman et al., 2017). In this section, we present the results from preliminary characterization ($N_2$ at 77 K) and high-pressure sorption ($CO_2$ at 50 °C) experiments conducted on powdered Opalinus Clay sample (particle size $\leq$100 µm) sourced from the Mont Terri underground laboratory in Switzerland. The sample used is largely dominated by clay minerals (70 wt%), including illite-smectite mixed layer (12 wt%) and illite (30 wt%) (the rest is mostly kaolinite, another non-expandable clay mineral) (Wenning et al., 2021). Table 8.1 summarizes the skeletal density, surface area, and pore volume of Opalinus Clay in comparison to those of ISCz-1 and IMt-2. The structural properties of Opalinus Clay reflect its clay mineral compositions, a mixture illite-smectite mixed layer (represented by ISCz-1) and illite (represented by IMt-2). The total pore volume of Opalinus Clay (0.058 $cm^3/g$) is greater than that of IMt-2 (0.036 $cm^3/g$), but smaller than that of ISCz-1 (0.078 $cm^3/g$), resulting in the value of $\rho_{sk}$ also between that of the two source clay

Table 8.1: Summary of the textural properties of Opalinus Clay, ISCz-1, and IMt-2

| Property | Probe gas | Unit | Opalinus Clay | ISCz-1 | IMt-2 |
|---|---|---|---|---|---|
| Skeletal density | He | $[g/cm^3]$ | $2.731 \pm 0.01$ | $2.689 \pm 0.009$ | $2.784 \pm 0.004$ |
| External surface area† | $N_2$ | $[m^2/g]$ | $38.39 \pm 0.13$ | $32.58 \pm 0.10$ | $21.90 \pm 0.09$ |
| Internal surface area‡ | $H_2O$ | $[m^2/g]$ | $63.13 \pm 2.47$ | $143.59 \pm 2.84$ | $50.06 \pm 0.68$ |
| Micropore volume* | $N_2$ | $[cm^3/g]$ | 0.004 | 0.001 | 0.003 |
| Mesopore volume* | $N_2$ | $[cm^3/g]$ | 0.047 | 0.062 | 0.026 |
| Macropore volume* | $N_2$ | $[cm^3/g]$ | 0.007 | 0.015 | 0.007 |

† BET surface area (Brunauer et al., 1938)
‡ Modified BET surface area (Mooney et al., 1952a)
* NLDFT on zeolite cylindrical model

minerals. However, the micropore volume of Opalinus Clay is greater than that of both ISCz-1 and IMt-2, possibly responsible for its larger surface area. Although the internal surface area of Opalinus Clay is larger than it external surface area, the difference is not as significant as that of STx-1b, SWy-2, or ISCz-1 reflecting its composition dominated by non-expandable illite and kaolinite. However, more accurate estimates of the structural properties must be obtained from sorption measurements using multiple gases as discussed in the preceding chapters. The higher micropore volume and surface area of Opalinus Clay compared to ISCz-1 and IMt-2 are manifested in the high-pressure sorption isotherms of $CO_2$ shown in Figure 8.1. The $CO_2$ sorption amount of Opalinus Clay is greater than that of ISCz-1 especially for $\rho_b \leq 5\,\text{mol/L}$ due to its higher micropore volume. The interpretation of the isotherms can be better made with the results obtained from

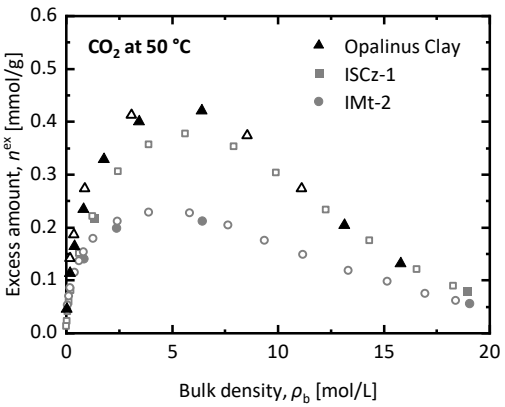



Figure 8.1: $CO_2$ adsorption (closed symbols) and desorption (open symbols) isotherms on Opalinus Clay, STx-1b, SWy-2, ISCz-1, and IMt-2 at 50 °C. Error bars are omitted for visual clarity.

the LDFT model as demonstrated in this thesis. For clay-rich rocks, such as Opalinus Clay, the model can also be predictive by accounting for the interactions on their heterogeneous surfaces. In other words, the interaction energies obtained from the pure clay minerals can be used to predict adsorption on rocks dominated by the same clay minerals given that the porous properties of the rock are estimated accurately.

### 8.2.2 Binary adsorption of $CO_2$ and $CH_4$

The adsorption measurements reported in this thesis have only been performed for single-component $CO_2$ and $CH_4$ and any quantitative estimate of binary adsorption of the two fluids has been determined through the analysis of adsorption metrics, such as adsorption selectivity. However, our understanding of the competitive adsorption between $CO_2$ and $CH_4$ is relevant to

the application of enhanced gas recovery, and can be consolidated and benefit from experimental binary adsorption data. To the best of my knowledge, experimental measurements of adsorption of the binary mixture of $CO_2$ and $CH_4$ have not yet been reported on clay minerals or clay-rich rocks possibly due to the intrinsic difficulty of conducting such experiments. While the experimental procedure of measuring the uptake amount of $CO_2/CH_4$ mixture does not significantly differ from that of measuring single-component adsorption, the data analysis needed to present the composition of the adsorbed amount requires the knowledge of the void volume of the measuring chamber, $V_{\text{void}}$ (the volume of the measuring chamber minus the volume of the sample and suspended metal parts), and the composition of the bulk phase inside the measuring chamber. The rest of this subsection describes the preliminary work performed in an effort to modify the setup described in Chapter 3 for the capability of measuring binary adsorption data.

The mass adsorbed for the individual components of binary mixtures can be determined from the following mass balance (Dreisbach et al., 1999; Ottiger et al., 2008a):

$$m_{\text{ads},i} = m_{\text{feed},i} - m_{\text{bulk},i} = w_{\text{feed},i} m_{\text{feed}} - w_{\text{feed},i} m_{\text{bulk}} \tag{8.1}$$

where $m_{\text{ads},i}$ is the adsorbed mass of component $i$, $m_{\text{feed},i}$ is the mass of component $i$ in the feed mixture, and $m_{\text{bulk},i}$ is the mass of component $i$ in the bulk phase after reaching equilibrium. The terms $w_{\text{feed},i}$ and $w_{\text{feed},i}$ represent the mass concentration of component $i$ in the feed and in the bulk phase, respectively; and $m_{\text{feed}} = m_{\text{ads}} + m_{\text{bulk}}$ and $m_{\text{bulk}} = \rho_{\text{b}} V_{\text{void}}$. The value of total adsorbed mass, $m_{\text{ads}}$, is determined from Equation 3.1.

The value of $V_{\text{void}}$ can be measured through the method of gas expansion (Ottiger et al., 2008a) as shown in Figure 8.2. A container with an unknown volume, $V_1$, is connected to the measuring chamber of $V_{\text{void}}$ with a valve installed between them. The measuring chamber is first filled with an inert gas, such as He or Ar, the density and pressure of which are measured precisely as described in Chapter 3. The valve is then opened to allow the gas to expand into two volumes. The following equation can be written to describe the expansion:

$$\rho_1 V_{\text{void}} = \rho_2 V_{\text{void}} + \rho_2 V_1 \tag{8.2}$$

where $\rho_1$ and $\rho_2$ are the gas densities before and after the valve is opened, respectively. The container is then filled with stainless steel balls with a known collective volume of $V_{\text{balls}}$. The same

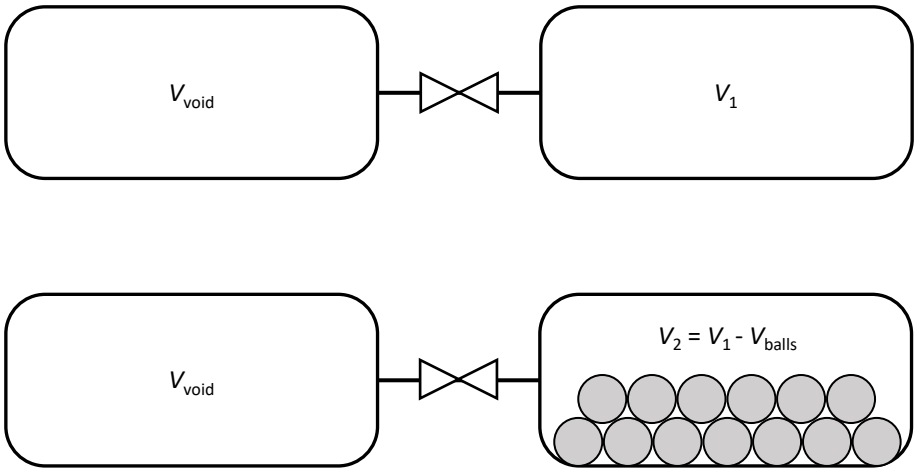



Figure 8.2: Schematic representation of the two-step gas expansion experiment in which a container with an unknown volume of $V_1$ is connected to the measuring chamber for the first step of the experiment (top). The second step of the experiment involves the same container filled with steel balls with a known volume of $V_{\text{balls}}$ (bottom).

procedure described above can be repeated for which the following equation can be written:

$$\rho_1^* V_{\text{void}} = \rho_2^* V_{\text{void}} + \rho_2^* V_2 = \rho_2^* V_{\text{void}} + \rho_2^* (V_1 - V_{\text{balls}}) \tag{8.3}$$

where $\rho_1^*$ and $\rho_2^*$ are the gas densities before and after the valve is opened, respectively, measured from the second expansion experiment. Equation 8.2 and 8.3 can then be combined to find the value of $V_{\text{void}}$:

$$V_{\text{void}} = \frac{\rho_2^* V_{\text{balls}}}{\left((\rho_2^*/\rho_2)(\rho_1 - \rho_2) + (\rho_2^* - \rho_1^*)\right)} \tag{8.4}$$

While the value of $V_{\text{void}}$ determined from preliminary expansion experiments using He and Ar was approximately $170\,\text{cm}^3$, additional experiments must be conducted to produce multiple sets of repeated measurements to obtain a more accurate estimate.

The value of $w_{\text{bulk},i}$ can be obtained with the use of analytic instruments, such as gas chromatography (GC) or mass spectrometry (MS), or from the measured density of the mixture which can be defined as a function of composition as described in Dreisbach et al. (2002b). Both methods require a significant amount of adsorption to take place to generate sufficient change in the bulk phase composition. The basket shown in Figure 8.3 has been designed and made to contain more adsorbent

materials and fit inside the measuring chamber below the original sample basket. However, the

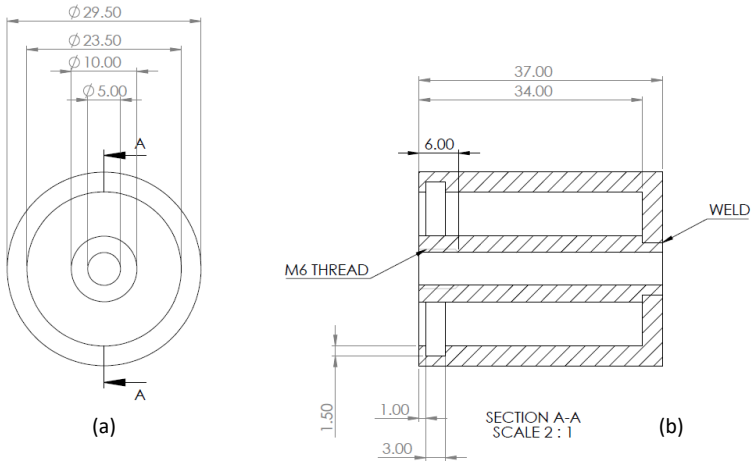



Figure 8.3: (a) Top and (b) side view of the design of a sample basket for holding extra adsorbent materials to induce greater change in the bulk phase composition. The sample basket was designed and machined by Mr. Gavin Barnes from the Department of Chemical Engineering Workshop.

method proposed by Dreisbach et al. (2002b) of using the measured density to estimate the bulk phase composition could not be completed due to two major challenges. First, the $CO_2$ and $CH_4$ densities were too close in value to be distinguished at the experimental pressure and temperature (below 50 bar and 50 °C) for the measured density to be used to calculate the bulk composition; the use of GC or MS may be a more suitable method. Second, the powdered adsorbent sample inside the sample basket shown in Figure 8.3 presented an issue of sample elutriation, preventing an accurate estimate of the adsorbed amount contributed by the extra adsorbent materials. These challenges were left unsolved, but I hope the work on binary adsorption continues in the future as the lab could benefit from an experimental setup capable of measuring mixture adsorption also for applications not considered in this thesis, such as carbon capture technologies or adsorption-based separation processes.

### 8.2.3 Effect of various hydration states on supercritical sorption

We demonstrated in Chapter 7 that the presence of water inside smectite interlayers increases the amount of adsorption for $CO_2$ and $CH_4$. Only sub-1W hydration state was studied in this thesis, but smectite clay minerals have varying degrees of swelling depending on their hydration states as discussed in Chapter 7. The amount of adsorption on smectite clay minerals is expected to change under variably hydrated states as shown by the differing levels of intercalation of $CO_2$ and $CH_4$ (Schaef et al., 2012; Bowers et al., 2018). Comprehensive quantification of the effect of

varying hydration states on sorption uptake of expansive clay minerals is of great interest as the clay minerals present in clay-rich environments are likely to exist in variably hydrated states. The amount of pre-adsorbed water can be controlled by moisture-equilibrating the clay mineral sample *in situ* inside the measuring chamber of the Rubotherm balance. This can be done by installing a basket containing purified water at the bottom of the measuring chamber of the balance below the sample basket (similar to the basket shown in Figure 8.3) and a humidity sensor that measures the relative humidity inside the measuring chamber. However, the method of filling the measuring chamber with pure fluid (either $CO_2$ or $CH_4$) in the presence of water still remains a major challenge.

### 8.2.4 Direct observation of supercritical fluid confinement using neutron scattering techniques

The magnetic suspension balance is an excellent tool for quantifying the sorption uptake of adsorbent materials under elevated temperature and pressure conditions as demonstrated in this thesis. However, the sorption measurements alone can only provide limited understanding and indirect evidence of fluid confinement and pore space invasion as the nanoscale structure and dynamics of adsorbed $CO_2$ and $CH_4$ molecules cannot be known from them. Therefore, the findings of this thesis inferred from the sorption measurements, such as the estimated density of the adsorbed phase, the location of adsorbed $CO_2$ and $CH_4$ molecules inside the microstructure of dry and hydrated clay minerals, and the peculiar micropore accessibility of illite, can be greatly complemented and confirmed by experimental data produced by *in situ* neutron scattering experiments as demonstrated by recent studies (Steriotis et al., 2004; Melnichenko et al., 2012; Rother et al., 2013; Stefanopoulos et al., 2017; Liu et al., 2019). Furthermore, the examination of porous structure, especially the microstructure of natural rocks, is increasingly conducted by small angle neutron scattering (SANS) (Clarkson et al., 2013; Sang et al., 2018), which can complement the results of the conventional characterization techniques utilized in this thesis, such as gas/vapor sorption and He gravimetry/pycnometry. In this aim, I had planned to conduct experiments using General Purpose Small Angle Neutron Scattering (GP-SANS) diffractometer at Oak Ridge National Laboratory (ORNL) in the United States through participation in ORNL's short-term research program for graduate students. The GP-SANS diffractometer is capable of providing nanoscale information in the length range of 0.5 nm to 200 nm (`https://neutrons.ornl.gov/gpsans`) and hosting various sample environments including sample chambers that are able to withstand ex-

treme pressure and temperature conditions considered in this thesis. Two main research objectives were planned to be accomplished at ORNL to complement and extend the work presented in Chapter 5, 6, and 7: 1) textural characterization of clay minerals using SANS to obtain properties such as skeletal density, specific interface area, and pore-size distribution, and 2) direct observation of molecule confinement of $CO_2$ and $CH_4$ ($CD_4$) inside the nanopores of swelling and non-swelling clay minerals (both under dry and hydrated conditions) at 50 °C at 50 bar, 70 bar, 100 bar and 200 bar. The results of the experiments could be analyzed in direct comparison with the sorption measurements produced by the Rubotherm balance repoted in this thesis, which has been rarely done in the literature. The program was unfortunately suspended indefinitely due to the travel restrictions imposed by ORNL in the midst of worldwide spread of the novel coronavirus in early 2020. However, the idea of complementing the experimental work produced by the Rubotherm balance with the neutron scattering technique is an exciting research opportunity and I hope it can be pursued in the near future.

# Bibliography


Al-Muhtaseb, S.A., Ritter, J.A., 1999. Roles of Surface Heterogeneity and Lateral Interactions on the Isosteric Heat of Adsorption and Adsorbed Phase Heat Capacity. The Journal of Physical Chemistry B 103, 2467–2479.

Amann, A., Waschbüsch, M., Bertier, P., Busch, A., Krooss, B.M., Littke, R., 2011. Sealing rock characteristics under the influence of $CO_2$. Energy Procedia 4, 5170–5177.

Amann-Hildenbrand, A., Bertier, P., Busch, A., Krooss, B.M., 2013. Experimental investigation of the sealing capacity of generic clay-rich caprocks. International Journal of Greenhouse Gas Control 19, 620–641.

Ambrose, R.J., Hartman, R.C., Diaz-Campos, M., Akkutlu, I.Y., Sondergeld, C.H., 2012. Shale gas-in-place calculations part I: new pore-scale considerations. SPE Journal 17, 219–229.

Ansari, H., Joss, L., Hwang, J., Trusler, J.P.M., Maitland, G., Pini, R., 2020. Supercritical adsorption in micro- and meso-porous carbons and its utilisation for textural characterisation. Microporous and Mesoporous Materials 308, 110537.

Aranovich, G.L., Donohue, M.D., 1995. Adsorption isotherms for microporous adsorbents. Carbon 33, 1369–1375.

Aranovich, G.L., Donohue, M.D., 1996. A new model for lattice systems. The Journal of Chemical Physics 105, 7059–7063.

Aranovich, G.L., Donohue, M.D., 1997. Predictions of Multilayer Adsorption Using Lattice Theory. Journal of Colloid and Interface Science 189, 101–108.

Aranovich, G.L., Donohue, M.D., 2003. Theory of multilayer adsorption with correct critical behavior. Langmuir 19, 3822–3829.

Armitage, P.J., Worden, R.H., Faulkner, D.R., Aplin, A.C., Butcher, A.R., Espie, A.A., 2013. Mercia Mudstone Formation caprock to carbon capture and storage sites: petrology and petrophysical characteristics. Journal of the Geological Society 170, 119–132.

Bakhshian, S., Sahimi, M., 2017. Adsorption-induced swelling of porous media. International Journal of Greenhouse Gas Control 57, 1–13.

Baltrusaitis, J., Schuttlefield, J.D., Zeitler, E., Jensen, J.H., Grassian, V.H., 2007. Surface Reactions of Carbon Dioxide at the Adsorbed Water-Oxide Inteface. The Journal of Physical Chemistry C 111, 14870–14880.

Barrett, E.P., Joyner, L.G., Halenda, P.P., 1951. The Determination of Pore Volume and Area Distributions in Porous Substances. I. Computations from Nitrogen Isotherms. Journal of the American Chemical Society 73, 373–380.

Bénard, P., Chahine, R., 1997. Modeling of high-pressure adsorption isotherms above the critical temperature on microporous adsorbents: application to methane. Langmuir 13, 808–813.

Bénard, P., Chahine, R., 2001. Determination of the Adsorption Isotherms of Hydrogen on Activated Carbons above the Critical Temperature of the Adsorbate over Wide Temperature and Pressure Ranges. Langmuir 17, 1950–1955.

Berberan-Santos, M.N., Bodunov, E.N., Pogliani, L., 2008. The van der Waals equation: analytical and approximate solutions. Journal of Mathematical Chemistry 43, 1437–1457.

Bérend, I., Cases, J.M., Francois, M., Uriot, J.P., Michot, L., Masion, A., Thomas, F., 1995. Mechanism of Adsorption and Desorption of Water Vapor by Homoionic Montmorillonites: 2. The $Li^+$, $Na^+$, $K^+$, $Rb^+$, and $Cs^+$-Exchanged Forms. Clays and Clay Minerals 43, 324–336.

Bergaya, F., Lagaly, G., 2006. General Introduction: Clays, Clay Minerals, and Clay Science, in: Bergaya, F., Theng, B.K.G., Lagaly, G. (Eds.), Handbook of Clay Science. 1st ed.. Elsevier, Oxford. volume 1. chapter 1, pp. 1–18.

Bi, H., Jiang, Z., Li, J., Li, P., Chen, L., Pan, Q., Wu, Y., 2016. The Ono–Kondo model and an experimental study on supercritical adsorption of shale gas: A case study on Longmaxi shale in southeastern Chongqing, China. Journal of Natural Gas Science and Engineering 35, 114–121.

Billemont, P., Coasne, B., De Weireld, G., 2011. An Experimental and Molecular Simulation Study of the Adsorption of Carbon Dioxide and Methane in Nanoporous Carbons in the Presence of Water. Langmuir 27, 1015–1024.

Billemont, P., Coasne, B., De Weireld, G., 2013. Adsorption of Carbon Dioxide, Methane, and Their Mixtures in Porous Carbons: Effect of Surface Chemistry, Water Content, and Pore Disorder. Langmuir 29, 3328–3338.

Bird, P., 1984. Hydration-phase diagrams and friction of montmorillonite under laboratory and geologic conditions, with implications for shale compaction, slope stability, and strength of fault gouge. Tectonophysics 107, 235–260.

Blümel, S., Findenegg, G.H., 1985. Critical Adsorption of a Pure Fluid on a Graphite Substrate. Physical Review Letters 54, 447–450.

Bourg, I.C., Beckingham, L.E., DePaolo, D.J., 2015. The nanoscale basis of $CO_2$ trapping for geologic storage. Environmental Science and Technology 49, 10265–10284.

Bowers, G.M., Loring, J.S., Schaef, H.T., Walter, E.D., Burton, S.D., Hoyt, D.W., Cunniff, S.S., Loganathan, N., Kirkpatrick, R.J., 2018. Interaction of Hydrocarbons with Clays under Reservoir Conditions: In Situ Infrared and Nuclear Magnetic Resonance Spectroscopy and X-ray Diffraction for Expandable Clays with Variably Wet Supercritical Methane. ACS Earth and Space Chemistry 2, 640–652.

Bowers, G.M., Loring, J.S., Walter, E.D., Burton, S.D., Bowden, M.E., Hoyt, D.W., Arey, B., Larsen, R.K., Kirkpatrick, R.J., 2019. Influence of Smectite Structure and Hydration on Supercritical Methane Binding and Dynamics in Smectite Pores. The Journal of Physical Chemistry C 123, 29231–29244.

Brandani, S., Mangano, E., Sarkisov, L., 2016. Net, excess and absolute adsorption and adsorption of helium. Adsorption 22, 261–276.

Brigatti, M.F., Galan, E., Theng, B.K.G., 2006. Structures and Mineralogy of Clay Minerals, in: Bergaya, F., Theng, B.K.G., Lagaly, G. (Eds.), Handbook of Clay Science. 1st ed.. Elsevier, Oxford. volume 1. chapter 2, pp. 19–86.

Brunauer, S., 1943. The Adsorption of Gases and Vapors Vol. 1 Physical Adsorption. Oxford University Press, London.

Brunauer, S., Emmett, P.H., Teller, E., 1938. Adsorption of Gases in Multimolecular Layers. Journal of the American Chemical Society 60, 309–319.

Busch, A., Alles, S., Gensterblum, Y., Prinz, D., Dewhurst, D.N., Raven, M.D., Stanjek, H., M., K.B., 2008. Carbon dioxide storage potential of shales. International Journal of Greenhouse Gas Control 2, 297–308.

Busch, A., Amann-Hildenbrand, A., Bertier, P., Waschbuesch, M., Krooss, B.M., 2010. The significance of caprock sealing integrity for $CO_2$ storage, in: SPE International Conference on $CO_2$ Capture, Storage, and Utilization, Society of Petroleum Engineers. pp. 1–8.

Busch, A., Bertier, P., Gensterblum, Y., Rother, G., Spiers, C.J., Zhang, M., Wentinck, H.M., 2016. On sorption and swelling of $CO_2$ in clays. Geomechanics and Geophysics for Geo-energy and Geo-resources 2, 111–130.

Busch, A., Schweinar, K., Kampman, N., Coorn, A., Pipich, V., Feoktystov, A., Leu, L., Amann-Hildenbrand, A., Bertier, P., 2017. Determining the porosity of mudrocks using methodological pluralism. Geological Society, London, Special Publications 454, 15–38.

Carmody, O., Frost, R., Xi, Y., Kokot, S., 2007. Surface characterisation of selected sorbent materials for common hydrocarbon fuels. Surface Science 601, 2066–2076.

Cases, J.M., Berend, I., Besson, G., Francois, M., Uriot, J.P., Thomas, F., Poirier, J.E., 1992. Mechanism of adsorption and desorption of water vapor by homoionic montmorillonite. 1. The sodium-exchanged form. Langmuir 8, 2730–2739.

Cases, J.M., Berend, I., Francois, M., Uriot, J.P., Michot, L.J., Thomas, F., 1997. Mechanism of adsorption and desorption of water vapor by homoionic montmorillonite: 3. The $Mg^{2+}$, $Ca^{2+}$, $Sr^{2+}$ and $Ba^{2+}$ exchanged form. Clays and Clay Minerals 45, 8–22.

Cases, J.M., Cunin, P., Grileet, Y., Poissignon, C., Yvon, J., 1986. Methods of analyzing morphology of kaolinites - Relations between crystalographic and morphological properties. Clay Minerals 21, 55–68.

Cerato, A.B., Lutenegger, A.J., 2002. Determination of surface area of fine-grained soils by the ethylene glycol monoethyl ether (EGME) method. Geotechnical Testing Journal 25, 315–321.

Che, C., Glotch, T.D., Bish, D.L., Michalski, J.R., Xu, W., 2011. Spectroscopic study of the dehydration and/or dehydroxylation of phyllosilicate and zeolite minerals. Journal of Geophysical Research 116, 1–23.

Chen, G., Lu, S., Liu, K., Han, T., Xu, C., Xue, Q., Shen, B., Guo, Z., 2018. GCMC simulations on the adsorption mechanisms of $CH_4$ and $CO_2$ in K-illite and their implications for shale gas exploration and development. Fuel 224, 521–528.

Chen, G., Lu, S., Zhang, J., Xue, Q., Han, T., Xue, H., Tian, S., Li, J., Xu, C., Pervukhina, M., Clennell, B., 2016a. Research of $CO_2$ and $N_2$ Adsorption Behavior in K-Illite Slit Pores by GCMC Method. Scientific Reports 6, 1–10.

Chen, G., Zhang, J., Lu, S., Pervukhina, M., Liu, K., Xue, Q., Tian, H., Tian, S., Li, J., Clennell, M.B., Dewhurst, D.N., 2016b. Adsorption Behavior of Hydrocarbon on Illite. Energy and Fuels 30, 9114–9121.

Cheng, A.L., Huang, W.L., 2004. Selective adsorption of hydrocarbon gases on clays and organic matter. Organic Geochemistry 35, 413–423.

Chiou, C.T., Rutherford, D.W., 1997. Effects of exchanged cation and layer charge on the sorption of water and EGME vapors on montmorillonite clays. Clays and Clay Minerals 45, 867–880.

Clarkson, C.R., Solano, N., Bustin, R.M., Bustin, A.M.M., Chalmers, G.R.L., He, L., Melnichenko, Y.B., Radliński, A.P., Blach, T.P., 2013. Pore structure characterization of North American shale gas reservoirs using USANS/SANS, gas adsorption, and mercury intrusion. Fuel 103, 606–616.

Cole, D.R., Chialvo, A.A., Rother, G., Vlček, L., Cummings, P.T., 2010. Supercritical fluid behavior at nanoscale interfaces: implications for $CO_2$ sequestration in geologic formations. Philosophical Magazine 90, 2339–2363.

Curtis, J.B., 2002. Fractured shale-gas systems. AAPG Bulletin 86, 1921–1938.

Czepirski, L., Jagiello, J., 1989. Virial-type thermal equation of gas-solid adsorption. Chemical Engineering Science 44, 797–801.

De Jong, S.M., Spiers, C.J., Busch, A., 2014. Development of swelling strain in smectite clays through exposure to carbon dioxide. International Journal of Greenhouse Gas Control 24, 149–161.

De Weireld, G., Frère, M., Jadot, R., 1999. Automated determination of high-temperature and high-pressure gas adsorption isotherms using a magnetic suspension balance. Measurement Science and Technology 10, 117–126.

Deeds, C.T., Van Olphen, H., 1961a. Density Studies in Clay-Liquid Systems, in: Copeland, L.E., Beebe, R.A., Graham, D.P., Zettlemoyer, A.C., Zisman, W.C. (Eds.), Solid Surfaces and the Gas-Solid Interfaces. ACS Publications, Washington D.C.. volume 33. chapter 35, pp. 332–339.

Deeds, C.T., Van Olphen, H., 1961b. Density studies in clay-liquid systems, part II: application to core analysis. Clays and Clay Minerals 10, 318–328.

Delage, P., Cui, Y.J., Tang, A.M., 2010. Clays in radioactive waste disposal. Journal of Rock Mechanics and Geotechnical Engineering 2, 111–123.

Dettmann, M.G., 1958. Water uptake by pure clays and soil crumbs. Journal of Soil Science 9, 306–315.

Di Giovanni, O., Dörfler, W., Mazzotti, M., Morbidelli, M., 2001. Adsorption of supercritical carbon dioxide on silica. Langmuir 17, 4316–4321.

Do, D.D., 1998. Adsorption Analysis: Equilibria and Kinetics. volume 2 of *Series on Chemical Engineering*. Imperial College Press, London.

Do, D.D., Do, H.D., 2002. Analysis of Adsorption Data of Graphitized Thermal Carbon Black with a DFT-Lattice Gas Theory. Adsorption 8, 309–324.

Do, D.D., Do, H.D., 2007. Appropriate volumes for adsorption isotherm studies: The absolute void volume, accessible pore volume and enclosing particle volume. Journal of Colloid and Interface Science 316, 317–330.

Do, D.D., Do, H.D., Fan, C., Nicholson, D., 2010. On the Existence of Negative Excess Isotherms for Argon Adsorption on Graphite Surfaces and in Graphitic Pores under Supercritical Conditions at Pressures up to 10,000 atm. Langmuir 26, 4796–4806.

Dogan, M., Dogan, A.U., Yesilyurt, F.I., Alaygut, D., Buckner, I., Wurster, D.E., 2007. Baseline studies of The Clay Minerals Society special clays: specific surface area by the Brunauer Emmett Teller (BET) method. Clays and Clay Minerals 55, 534–541.

Donohue, M.D., Aranovich, G.L., 1998. Classification of Gibbs adsorption isotherms. Advances in Colloid and Interface Science 76-77, 137–152.

Downs, R.T., Hall-Wallace, M., 2003. The American Mineralogist crystal structure database. American Mineralogist 88, 247–250.

Dreisbach, F., Lösch, H.W., Harting, P., 2002a. Highest Pressure Adsorption Equilibria Data: Measurement with Magnetic Suspension Balance and Analysis with a New Adsorbent/Adsorbate-Volume. Adsorption 8, 95–109.

Dreisbach, F., Seif A. H., R., Lösch, H.W., 2002b. Gravimetric Measurement of Adsorption Equilibria of Gas Mixture $CO/H_2$ with a Magnetic Suspension Balance. Chemical Engineering and Technology 25, 1060–1065.

Dreisbach, F., Staudt, R., Keller, J.U., 1999. High pressure adsorption data of methane, nitrogen, carbon dioxide and their binary and ternary mixtures on activated carbon. Adsorption 5, 215–227.

Duan, S., Gu, M., Du, X., Xian, X., 2016. Adsorption Equilibrium of $CO_2$ and $CH_4$ and Their Mixture on Sichuan Basin Shale. Energy and Fuels 30, 2248–2256.

Duan, Z., Sun, R., Zhu, C., Chou, I.M., 2006. An improved model for the calculation of $CO_2$ solubility in aqueous solutions containing $Na^+$, $K^+$, $Ca^{2+}$, $Mg^{2+}$, $Cl^-$, and $SO_4{}^{2-}$. Marine Chemistry 98, 131–139.

Dubinin, M.M., Radushkevich, L.V., 1947. The Equation of the Characteristic Curve of the Activated Charcoal. Proceedings of the Union of Soviet Socialist Republics Academy of Sciences 55, 331–337.

Fan, E., Tang, S., Zhang, C., Guo, Q., Sun, C., 2014. Methane sorption capacity of organics and clays in high-over matured shale-gas systems. Energy Exploration and Exploitation 32, 927–942.

Ferrage, E., Lanson, B., Sakharov, B.A., Drits, V.A., 2005. Investigation of smectite hydration properties by modeling experimental X-ray diffraction patterns: Part I. Montmorillonite hydration properties. American Mineralogist 90, 1358–1374.

Frinak, E.K., Mashburn, C.D., Tolbert, M.A., 2005. Infrared characterization of water uptake by low-temperature Na-montmorillonite: Implications for Earth and Mars. Journal of Geophysical Research 110, 1–7.

Gao, W., Butler, D., Tomasko, D.L., 2004. High-pressure adsorption of $CO_2$ on NaY zeolite and model prediction of adsorption isotherms. Langmuir 20, 8083–8089.

Gasparik, M., Rexer, T.F., Aplin, A.C., Billemont, P., De Weireld, G., Gensterblum, Y., Henry, M., Krooss, B.M., Liu, S., Ma, X., Sakurovs, R., Song, Z., Staib, G., Thomas, K.M., Wang, S.,

Zhang, T., 2014. First international inter-laboratory comparison of high-pressure $CH_4$ , $CO_2$ and $C_2H_6$ sorption isotherms on carbonaceous shales. International Journal of Coal Geology 132, 131–146.

Giesting, P., Guggenheim, S., Koster van Groos, A.F., Busch, A., 2012a. Interaction of carbon dioxide with Na-exchanged montmorillonite at pressures to 640 bars: Implications for $CO_2$ sequestration. International Journal of Greenhouse Gas Control 8, 73–81.

Giesting, P., Guggenheim, S., Koster van Groos, A.F., Busch, A., 2012b. X-ray Diffraction Study of K- and Ca-Exchanged Montmorillonites in $CO_2$ Atmospheres. Environmental Science and Technology 46, 5623–5630.

Goodman, H.E., Imbus, S.W., Espie, T., Minnig, C., Rösli, U., Fierz, T., Lettry, Y., 2017. Large Rock Mass Experimentation @ Mont Terri Underground Research Laboratory - $CO_2$ Containment Assurance Experiments. Energy Procedia 114, 5139–5150.

Gregg, S.J., Sing, K.S.W., 1982. Adsorption, Surface Area and Porosity. 2nd ed., Academic Press, London.

Grekov, D., Montavon, G., Robinet, J.C., Grambow, B., 2019. Smectite fraction assessment in complex natural clay rocks from interlayer water content determined by thermogravimetric and thermoporometry analysis. Journal of Colloid and Interface Science 555, 157–165.

Grekov, D.I., Suzuki-Muresan, T., Kalinichev, A.G., Pré, P., Grambow, B., 2020. Thermodynamic data of adsorption reveal the entry of $CH_4$ and $CO_2$ in a smectite clay interlayer. Physical Chemistry Chemical Physics 22, 16727–16733.

Groen, J.C., Peffer, L.A.A., Pérez-Ramírez, J., 2003. Pore size determination in modified micro- and mesoporous materials . Pitfalls and limitations in gas adsorption data analysis. Microporous and Mesoporous Materials 60, 1–17.

Guggenheim, S., Martin, R.T., 1995. Definition of Clay and Clay Mineral: Joint Report of the AIPEA Nomenclature and CMS Nomenclature Committees. Clays and Clay Minerals 43, 255–256.

Gumma, S., Talu, O., 2010. Net Adsorption: A Thermodynamic Framework for Supercritical Gas Adsorption and Storage in Porous Solids. Langmuir 26, 17013–17023.

Han, D., Nur, A., Morgan, D., 1986. Effects of porosity and clay content on wave velocities in sandstones. Geophysics 51, 2093–2107.

Han, R., Walton, K.S., Sholl, D.S., 2019. Does Chemical Engineering Research Have a Reproducibility Problem? Annual Review of Chemical and Biomolecular Engineering 10, 43–57.

Hatch, C.D., Wiese, J.S., Crane, C.C., Harris, K.J., Kloss, H.G., Baltrusaitis, J., 2012. Water Adsorption on Clay Minerals As a Function of Relative Humidity: Application of BET and Freundlich Adsorption Models. Langmuir 28, 1790–1803.

Heller, R., Zoback, M.D., 2014. Adsorption of methane and carbon dioxide on gas shale and pure mineral samples. Journal of Unconventional Oil and Gas Resources 8, 14–24.

Heller-Kallai, L., 2006. Thermally Modified Clay Minerals, in: Bergaya, F., Theng, B.K.G., Lagaly, G. (Eds.), Handbook of Clay Science. 1st ed.. Elsevier, Oxford. volume 1. chapter 7.2, pp. 289–308.

Hill, T.L., 1987. Statistical Mechanics: Principles and Selected Applications. McGraw-Hill, New York.

Hirschfelder, J.O., Curtiss, C.F., Bird, R.B., 1954. Molecular Theory of Gases and Liquids. John Wiley and Sons, New York.

Hocker, T., Rajendran, A., Mazzotti, M., 2003. Measuring and Modeling Supercritical Adsorption in Porous Solids. Carbon Dioxide on 13X Zeolite and on Silica Gel. Langmuir 19, 1254–1267.

Holtz, R.D., Kovacs, W.D., 1981. An Introduction to Geotechnical Engineering. 1st ed., Prentice-Hall, New Jersey.

Horváth, G., Kawazoe, K., 1983. Method for the calculation of effective pore size distribution in molecular sieve carbon. Journal of Chemical Engineering of Japan 16, 470–475.

Hower, J., Eslinger, E.V., Hower, M.E., Perry, E.A., 1976. Mechanism of burial metamorphism of argillaceous sediment: 1. Mineralogical and chemical evidence. Geological Society of America Bulletin 87, 725.

Hwang, J., Joss, L., Pini, R., 2019. Measuring and modelling supercritical adsorption of $CO_2$ and $CH_4$ on montmorillonite source clay. Microporous and Mesoporous Materials 273, 107–121.

Hwang, J., Pini, R., 2019. Supercritical $CO_2$ and $CH_4$ Uptake by Illite-Smectite Clay Minerals. Environmental Science and Technology 53, 11588–11596.

Ijiri, A., Tomioka, N., Wakaki, S., Masuda, H., Shozugawa, K., Kim, S., Khim, B.K., Murayama, M., Matsuo, M., Inagaki, F., 2018. Low-Temperature Clay Mineral Dehydration Contributes to Porewater Dilution in Bering Sea Slope Subseafloor. Frontiers in Earth Science 6, 1–18.

Ilton, E.S., Schaef, H.T., Qafoku, O., Rosso, K.M., Felmy, A.R., 2012. In situ X-ray diffraction study of $Na^+$ saturated montmorillonite exposed to variably wet super critical $CO_2$. Environmental Science and Technology 46, 4241–4248.

Jeon, P.R., Choi, J., Yun, T.S., Lee, C.H., 2014. Sorption equilibrium and kinetics of $CO_2$ on clay minerals from subcritical to supercritical conditions: $CO_2$ sequestration at nanoscale interfaces. Chemical Engineering Journal 255, 705–715.

Ji, L., Zhang, T., Milliken, K.L., Qu, J., Zhang, X., 2012. Experimental investigation of main controls to methane adsorption in clay-rich rocks. Applied Geochemistry 27, 2533–2545.

Jiang, S., 2012. Clay Minerals from the Perspective of Oil and Gas Exploration, in: Valaškova, M., Martynkova, G.S. (Eds.), Clay Minerals in Nature - Their Characterization, Modification and Application. InTech. chapter 2, pp. 21–38.

Jin, Z., Firoozabadi, A., 2013. Methane and carbon dioxide adsorption in clay-like slit pores by Monte Carlo simulations. Fluid Phase Equilibria 360, 456–465.

Jin, Z., Firoozabadi, A., 2014. Effect of water on methane and carbon dioxide sorption in clay minerals by Monte Carlo simulations. Fluid Phase Equilibria 382, 10–20.

Joewondo, N., 2018. Pore structure of micro- and mesoporous mudrocks based on nitrogen and carbon dioxide sorption. Master's thesis. Colorado School of Mines.

Kadoura, A., Nair, A.K.N., Sun, S., 2016. Adsorption of carbon dioxide, methane, and their mixture by montmorillonite in the presence of water. Microporous and Mesoporous Materials 225, 331–341.

Kapoor, A., Ritter, J.A., Yang, R.T., 1989. On the Dubinin-Radushkevich Equation for Adsorption in Microporous Solids in the Henry's Law Region. Langmuir 5, 1118–1121.

Kim, H.J., Shi, Y., He, J., Lee, H.H., Lee, C.H., 2011. Adsorption characteristics of $CO_2$ and $CH_4$ on dry and wet coal from subcritical to supercritical conditions. Chemical Engineering Journal 171, 45–53.

Kloprogge, J.T., Komarneni, S., Amonette, J.E., 1999. Synthesis of smectite clay minerals: A critical review. Clays and Clay Minerals 47, 529–554.

Kozlowski, T., Rusin, A., Nartowska, E., 2014. The specific heat of dry homoionic forms of bentonites SWy-2 and Stx-1b: An effect of the fraction of particles less than 2$\mu$m. Applied Clay Science 101, 82–89.

Kraehenbuehl, F., Stoeckli, H.F., Brunner, F., Kahr, G., Mueller-Vonmoos, M., 1987. Study of the water-bentonite system by vapour adsorption, immersion calorimetry and X-ray techniques: I. Micropore volumes and internal surface areas, following Dubinin's theory. Clay Minerals 22, 1–9.

Krooss, B.M., van Bergen, F., Gensterblum, Y., Siemons, N., Pagnier, H.J.M., David, P., 2002. High-pressure methane and carbon dioxide adsorption on dry and moisture-equilibrated Pennsylvanian coals. International Journal of Coal Geology 51, 69–92.

Kuila, U., Prasad, M., 2013. Specific surface area and pore-size distribution in clays and shales. Geophysical Prospecting 61, 341–362.

Kurniawan, Y., Bhatia, S.K., Rudolph, V., 2006. Simulation of binary mixture adsorption of methane and $CO_2$ at supercritical conditions in carbons. AIChE Journal 52, 957–967.

Kwon, O., Kronenberg, A.K., Gangi, A.F., Johnson, B., 2001. Permeability of Wilcox shale and its effective pressure law. Journal of Geophysical Research 106, 19339–19353.

Lainé, M., Balan, E., Allard, T., Paineau, E., Jeunesse, P., Mostafavi, M., Robert, J.L., Le Caër, S., 2017. Reaction mechanisms in swelling clays under ionizing radiation: influence of the water amount and of the nature of the clay mineral. RSC Advances 7, 526–534.

Lee, H.H., Kim, H.J., Shi, Y., Keffer, D., Lee, C.H., 2013. Competitive adsorption of $CO_2/CH_4$ mixture on dry and wet coal from subcritical to supercritical conditions. Chemical Engineering Journal 230, 93–101.

Lee, M.S., McGrail, B.P., Rousseau, R., Glezakou, V.A., 2018. Molecular Level Investigation of $CH_4$ and $CO_2$ Adsorption in Hydrated Calcium–Montmorillonite. The Journal of Physical Chemistry C 122, 1125–1134.

Lemmon, E.W., Bell, I.H., Huber, M.L., McLinden, M.O., 2018. NIST Standard Reference Database 23: Reference Fluid Thermodynamic and Transport Properties-REFPROP.

Lemmon, E.W., McLinden, M.O., Friend, D.G., 1998. Thermophysical Properties of Fluid Systems.

Likos, W.J., Lu, N., 2006. Pore-scale analysis of bulk volume change from crystalline interlayer swelling in $Na^{+}$- and $Ca^{2+}$-smectite. Clays and Clay Minerals 54, 515–528.

Likos, W.J., Lu, N., 2012. Characterizing Physical Properties of Clay by Water Vapor Sorption, in: GeoCongress 2012, American Society of Civil Engineers, Reston, VA. pp. 1175–1184.

Liu, D., Yuan, P., Liu, H., Li, T., Tan, D., Yuan, W., He, H., 2013. High-pressure adsorption of methane on montmorillonite, kaolinite and illite. Applied Clay Science 85, 25–30.

Liu, S., Zhang, R., Karpyn, Z., Yoon, H., Dewers, T., 2019. Investigation of Accessible Pore Structure Evolution under Pressurization and Adsorption for Coal and Shale Using Small-Angle Neutron Scattering. Energy and Fuels 33, 837–847.

Loganathan, N., Bowers, G.M., Yazaydin, A.O., Schaef, H.T., Loring, J.S., Kalinichev, A.G., Kirkpatrick, R.J., 2018. Clay Swelling in Dry Supercritical Carbon Dioxide: Effects of Interlayer Cations on the Structure, Dynamics, and Energetics of $CO_2$ Intercalation Probed by XRD, NMR, and GCMD Simulations. The Journal of Physical Chemistry C 122, 4391–4402.

Loring, J.S., Ilton, E.S., Chen, J., Thompson, C.J., Martin, P.F., Bénézeth, P., Rosso, K.M., Felmy, A.R., Schaef, H.T., 2014. In Situ Study of $CO_2$ and $H_2O$ Partitioning between Na–Montmorillonite and Variably Wet Supercritical Carbon Dioxide. Langmuir 30, 6120–6128.

Loring, J.S., Schaef, H.T., Turcu, R.V.F., Thompson, C.J., Miller, Q.R.S., Martin, P.F., Hu, J., Hoyt, D.W., Qafoku, O., Ilton, E.S., Felmy, A.R., Rosso, K.M., 2012. In situ molecular spectroscopic evidence for $CO_2$ intercalation into montmorillonite in supercritical carbon dioxide. Langmuir 28, 7125–7128.

Lu, X.C., Li, F.C., Watson, A.T., 1995. Adsorption measurements in Devonian shales. Fuel 74, 599–603.

Lynch, F.L., 1997. Frio Shale mineralogy and the stoichiometry of the smectite-to-illite reaction: the most important reaction in clastic sedimentary diagenesis. Clays and Clay Minerals 45, 618–631.

Macht, F., Eusterhues, K., Pronk, G.J., Totsche, K.U., 2011. Specific surface area of clay minerals: Comparison between atomic force microscopy measurements and bulk-gas ($N_2$) and -liquid (EGME) adsorption methods. Applied Clay Science 53, 20–26.

Makaremi, M., Jordan, K.D., Guthrie, G.D., Myshakin, E.M., 2015. Multiphase Monte Carlo and Molecular Dynamics Simulations of Water and $CO_2$ Intercalation in Montmorillonite and Beidellite. The Journal of Physical Chemistry C 119, 15112–15124.

Malbrunot, P., Vidal, D., Vermesse, J., Chahine, R., Bose, T.K., 1997. Adsorbent Helium Density Measurement and Its Effect on Adsorption Isotherms at High Pressure. Langmuir 13, 539–544.

Marcus, Y., 1994. A simple empirical model describing the thermodynamics of hydration of ions of widely varying charges, sizes, and shapes. Biophysical Chemistry 51, 111–127.

Melnichenko, Y.B., He, L., Sakurovs, R., Kholodenko, A.L., Blach, T., Mastalerz, M., Radliński, A.P., Cheng, G., Mildner, D.F., 2012. Accessibility of pores in coal to methane and carbon dioxide. Fuel 91, 200–208.

Meunier, A., 2005. Clays. Springer, Heidelberg.

Michels, L., Fossum, J.O., Rozynek, Z., Hemmen, H., Rustenberg, K., Sobas, P.A., Kalantzopoulos, G.N., Knudsen, K.D., Janek, M., Plivelic, T.S., da Silva, G.J., 2015. Intercalation and retention of carbon dioxide in a smectite clay promoted by interlayer cations. Scientific reports 5, 8775.

Middleton, R.S., Carey, J.W., Currier, R.P., Hyman, J.D., Kang, Q., Karra, S., Jiménez-Martínez, J., Porter, M.L., Viswanathan, H.S., 2015. Shale gas and non-aqueous fracturing fluids: Opportunities and challenges for supercritical $CO_2$. Applied Energy 147, 500–509.

Minardi, A., Crisci, E., Ferrari, A., Laloui, L., 2016. Anisotropic volumetric behaviour of Opalinus clay shale upon suction variation. Géotechnique Letters 6, 144–148.

Moellmer, J., Moeller, A., Dreisbach, F., Glaeser, R., Staudt, R., 2011. High pressure adsorption of hydrogen, nitrogen, carbon dioxide and methane on the metal-organic framework HKUST-1. Microporous and Mesoporous Materials 138, 140–148.

Momma, K., Izumi, F., 2011. VESTA 3 for three-dimensional visualization of crystal, volumetric and morphology data. Journal of Applied Crystallography 44, 1272–1276.

Montgomery, S.L., Jarvie, D.M., Bowker, K.A., Pollastro, R.M., 2005. Mississippian Barnett Shale, Fort Worth basin, north-central Texas: gas-shale play with multi–trillion cubic foot potential. AAPG Bulletin 89, 155–175.

Mooney, R.W., Keenan, A.G., Wood, L.A., 1952a. Adsorption of Water Vapor by Montmorillonite. I. Heat of Desorption and Application of BET Theory. Journal of the American Chemical Society 74, 1367–1371.

Mooney, R.W., Keenan, A.G., Wood, L.A., 1952b. Adsorption of Water Vapor by Montmorillonite. II. Effect of Exchangeable Ions and Lattice Swelling as Measured by X-Ray Diffraction. Journal of the American Chemical Society 74, 1371–1374.

Morodome, S., Kawamura, K., 2009. Swelling Behavior of Na- and Ca-Montmorillonite up to 150C by in situ X-ray Diffraction Experiments. Clays and Clay Minerals 57, 150–160.

Murialdo, M., Ahn, C.C., Fultz, B., 2018. A thermodynamic investigation of adsorbate-adsorbate interactions of carbon dioxide on nanostructured carbons. AIChE Journal 64, 1026–1033.

Murray, H.H., 2007. Applied Clay Mineralogy: Occurrences, Processing and Application of Kaolins, Bentonite, Palygorskite-sepiolite, and Common Clays. volume 2. 1st ed., Elsevier, Amsterdam.

Myers, A.L., 2002. Thermodynamics of adsorption in porous materials. AIChE Journal 48, 145–160.

Myers, A.L., 2004a. Characterization of nanopores by standard enthalpy and entropy of adsorption of probe molecules. Colloids and Surfaces A: Physicochemical and Engineering Aspects 241, 9–14.

Myers, A.L., 2004b. Thermodynamics of Adsorption, in: Letcher, T.M. (Ed.), Chemical Thermodynamics for Industry. Royal Society of Chemistry. chapter 21, pp. 243–253.

Myers, A.L., Monson, P.A., 2002. Adsorption in porous materials at high pressure: theory and experiment. Langmuir 18, 10261–10273.

Myshakin, E.M., Saidi, W.A., Romanov, V.N., Cygan, R.T., Jordan, K.D., 2013. Molecular Dynamics Simulations of Carbon Dioxide Intercalation in Hydrated Na-Montmorillonite. The Journal of Physical Chemistry C 117, 11028–11039.

Nguyen, H.G.T., Espinal, L., van Zee, R.D., Thommes, M., Toman, B., Hudson, M.S.L., Mangano, E., Brandani, S., Broom, D.P., Benham, M.J., Cychosz, K.A., Bertier, P., Yang, F., Krooss, B.M., Siegelman, R.L., Hakuman, M., Nakai, K., Ebner, A.D., Erden, L., Ritter, J.A., Moran, A., Talu, O., Huang, Y., Walton, K.S., Billemont, P., De Weireld, G., 2018. A reference high-pressure $CO_2$ adsorption isotherm for ammonium ZSM-5 zeolite: results of an interlaboratory study. Adsorption 24, 531–539.

Nguyen, H.G.T., Sims, C.M., Toman, B., Horn, J., van Zee, R.D., Thommes, M., Ahmad, R., Denayer, J.F.M., Baron, G.V., Napolitano, E., Bielewski, M., Mangano, E., Brandani, S., Broom, D.P., Benham, M.J., Dailly, A., Dreisbach, F., Edubilli, S., Gumma, S., Möllmer, J., Lange, M., Tian, M., Mays, T.J., Shigeoka, T., Yamakita, S., Hakuman, M., Nakada, Y., Nakai, K., Hwang, J., Pini, R., Jiang, H., Ebner, A.D., Nicholson, M.A., Ritter, J.A., Farrando-Pérez, J., Cuadrado-Collados, C., Silvestre-Albero, J., Tampaxis, C., Steriotis, T., Řimnáčová, D., Švábová, M., Vorokhta, M., Wang, H., Bovens, E., Heymans, N., De Weireld, G., 2020. A reference high-pressure $CH_4$ adsorption isotherm for zeolite Y: results of an interlaboratory study. Adsorption 26, 1253–1266.

Norrish, K., 1954. The Swelling of Montmorillonite. Discussions of the Faraday of Society 18, 120–134.

Nuttall, B.C., Eble, C.F., Drahovzal, J.A., Bustin, R.M., 2005. Analysis of Devonian Black Shales in Kentucky for potential carbon dioxide sequestration and enhanced natural gas production. Technical Report. University of Kentucky, University of British Columbia. Lexington.

Oleinikova, A., Brovchenko, I., 2008. Nonmonotonic crossover from adsorption to desorption in supercritical fluid near a weakly attractive surface. Physical Review E - Statistical, Nonlinear, and Soft Matter Physics 78, 1–11.

Oleinikova, A., Brovchenko, I., Geiger, A., 2006. Behavior of a wetting phase near a solid boundary: Vapor near a weakly attractive surface. European Physical Journal B 52, 507–519.

Ono, S., Kondo, S., 1960. Molecular Theory of Surface Tension in Liquids, in: Structure of Liquids. Springer, Berlin, pp. 134–280.

Ottiger, S., Pini, R., Storti, G., Mazzotti, M., 2008a. Competitive adsorption equilibria of $CO_2$ and $CH_4$ on a dry coal. Adsorption 14, 539–556.

Ottiger, S., Pini, R., Storti, G., Mazzotti, M., 2008b. Measuring and Modeling the Competitive Adsorption of $CO_2$, $CH_4$, and $N_2$ on a Dry Coal. Langmuir 24, 9531–9540.

Ou, W., Geng, L., Lu, W., Guo, H., Qu, K., Mao, P., 2015. Quantitative Raman spectroscopic investigation of geo-fluids high-pressure phase equilibria: Part II. Accurate determination of $CH_4$ solubility in water from 273 to 603K and from 5 to 140MPa and refining the parameters of the thermodynamic model. Fluid Phase Equilibria 391, 18–30.

Pang, W., Jin, Z., 2019a. Ono-Kondo lattice model for propane multilayer adsorption in organic nanopores in relation to shale gas. Fuel 235, 158–166.

Pang, W., Jin, Z., 2019b. Revisiting methane absolute adsorption in organic nanopores from molecular simulation and Ono-Kondo lattice model. Fuel 235, 339–349.

Parilla, P.A., Gross, K., Hurst, K., Gennett, T., 2016. Recommended volumetric capacity definitions and protocols for accurate, standardized and unambiguous metrics for hydrogen storage materials. Applied Physics A 122, 201.

Park, J., Howe, J.D., Sholl, D.S., 2017. How Reproducible Are Isotherm Measurements in Metal–Organic Frameworks? Chemistry of Materials 29, 10487–10495.

Pevear, D.R., 1999. Illite and hydrocarbon exploration. Proceedings of the National Academy of Sciences 96, 3440–3446.

Pini, R., 2014. Interpretation of net and excess adsorption isotherms in microporous adsorbents. Microporous and Mesoporous Materials 187, 40–52.

Pini, R., Ottiger, S., Rajendran, A., Storti, G., Mazzotti, M., 2008. Near-critical adsorption of $CO_2$ on 13X zeolite and $N_2O$ on silica gel: lack of evidence of critical phenomena. Adsorption 14, 133–141.

Pini, R., Ottiger, S., Storti, G., Mazzotti, M., 2010. Prediction of competitive adsorption on coal by a lattice DFT model. Adsorption 16, 37–46.

Qajar, A., Daigle, H., Prodanović, M., 2016. The effects of pore geometry on adsorption equilibrium in shale formations and coal-beds: Lattice density functional theory study. Fuel 163, 205–213.

Quirk, J.P., 1955. Significance of surface areas calculated from water vapor sorption isotherms by use of the B.E.T. equation. Soil Science 80, 423–430.

Quirk, J.P., Murray, R.S., 1999. Appraisal of the Ethylene Glycol Monoethyl Ether Method for Measuring Hydratable Surface Area of Clays and Soils. Soil Science Society of America Journal 63, 839–849.

Reid, R.C., Prausnitz, J.M., Bruce, E.P., 1987. The Properties of Gases and Liquids. 4th ed., McGraw-Hill, New York.

Ross, D.J.K., Bustin, R.M., 2009. The importance of shale composition and pore structure upon gas storage potential of shale gas reservoirs. Marine and Petroleum Geology 26, 916–927.

Rother, G., Ilton, E.S., Wallacher, D., Hau$\beta$, T., Schaef, H.T., Qafoku, O., Rosso, K.M., Felmy, A.R., Krukowski, E.G., Stack, A.G., Grimm, N., Bodnar, R.J., 2013. $CO_2$ sorption to subsingle hydration layer montmorillonite clay studied by excess sorption and neutron diffraction measurements. Environmental Science and Technology 47, 205–211.

Rother, G., Krukowski, E.G., Wallacher, D., Grimm, N., Bodnar, R.J., Cole, D.R., 2012. Pore size effects on the sorption of supercritical $CO_2$ in mesoporous CPG-10 silica. Journal of Physical Chemistry C 116, 917–922.

Rouquerol, F., Rouquerol, J., Sing, K.S.W., Llewellyn, P., Maurin, G., 2014. Adsorption by Powders and Porous Solids: Principles, Methodology and Applications. 2nd ed., Academic Press, Oxford.

Rouquerol, J., Llewellyn, P., Rouquerol, F., 2007. Is the BET equation applicable to microporous adsorbents?. volume 160. Elsevier B.V.

Rutherford, D.W., Chiou, C.T., Eberl, D.D., 1997. Effects of exchanged cation on the microporosity of montmorillonite. Clays and Clay Minerals 45, 534–543.

Ruthven, D.M., 1984. Principles of Adsorption and Adsorption Processes. John Wiley and Sons, New York.

Ruthven, D.M., 2000. Adsorption.

Ruthven, D.M., Xu, Z., 1993. Diffusion of oxygen and nitrogen in 5A zeolite crystals and commercial 5A pellets. Chemical Engineering Science 48, 3307–3312.

Rutter, E., Mecklenburgh, J., Taylor, K., 2017. Geomechanical and petrophysical properties of mudrocks: introduction. Geological Society, London, Special Publications 454, 1–13.

Rutter, E.H., Mainprice, D.H., 1978. The effect of water on stress relaxation of faulted and unfaulted sandstone. Pure and Applied Geophysics 116, 634–654.

Salles, F., Bildstein, O., Douillard, J.M., Jullien, M., Raynal, J., Van Damme, H., 2010. On the Cation Dependence of Interlamellar and Interparticular Water and Swelling in Smectite Clays. Langmuir 26, 5028–5037.

Sanders, R.L., Washton, N.M., Mueller, K.T., 2010. Measurement of the Reactive Surface Area of Clay Minerals Using Solid-State NMR Studies of a Probe Molecule. The Journal of Physical Chemistry C 114, 5491–5498.

Sang, G., Liu, S., Zhang, R., Elsworth, D., He, L., 2018. Nanopore characterization of mine roof shales by SANS, nitrogen adsorption, and mercury intrusion: Impact on water adsorption/retention behavior. International Journal of Coal Geology 200, 173–185.

Sangwichien, C., Aranovich, G.L., 2002. Density functional theory predictions of adsorption isotherms with hysteresis loops. Colloids and Surfaces A: Physicochemical and Engineering Aspects 206, 313–320.

Sato, T., Watanabe, T., Otsuka, R., 1992. Effects of Layer Charge, Charge Location, and Energy Change on Expansion Properties of Dioctahedral Smectites. Clays and Clay Minerals 40, 103–113.

Schaef, H.T., Davidson, C.L., Owen, A.T., Miller, Q.R.S., Loring, J.S., Thompson, C.J., Bacon, D.H., Glezakou, V.A., McGrail, B.P., 2014. $CO_2$ utilization and storage in shale gas reservoirs: Experimental results and economic impacts. Energy Procedia 63, 7844–7851.

Schaef, H.T., Ilton, E.S., Qafoku, O., Martin, P.F., Felmy, A.R., Rosso, K.M., 2012. In situ XRD study of $Ca^{2+}$ saturated montmorillonite (STX-1) exposed to anhydrous and wet supercritical carbon dioxide. International Journal of Greenhouse Gas Control 6, 220–229.

Schaef, H.T., Loring, J.S., Glezakou, V.A., Miller, Q.R.S., Chen, J., Owen, A.T., Lee, M.S., Ilton, E.S., Felmy, A.R., McGrail, B.P., Thompson, C.J., 2015. Competitive sorption of $CO_2$ and $H_2O$ in 2:1 layer phyllosilicates. Geochimica et Cosmochimica Acta 161, 248–257.

Schell, J., Casas, N., Pini, R., Mazzotti, M., 2012. Pure and binary adsorption of $CO_2$, $H_2$, and $N_2$ on activated carbon. Adsorption 18, 49–65.

Schuttlefield, J.D., Cox, D., Grassian, V.H., 2007. An investigation of water uptake on clays minerals using ATR-FTIR spectroscopy coupled with quartz crystal microbalance measurements. Journal of Geophysical Research 112, 1–14.

Setzmann, U., Wagner, W., 1991. A New Equation of State and Tables of Thermodynamic Properties for Methane Covering the Range from the Melting Line to 625 K at Pressures up to 100 MPa. Journal of Physical and Chemical Reference Data 20, 1061–1155.

Shehata, A.M., Nasr-El-Din, H.A., 2014. Role of Sandstone Mineral Compositions and Rock Quality on the Performance of Low-Salinity Waterflooding, in: International Petroleum Technology Conference, International Petroleum Technology Conference, Kuala Lumpur. pp. 1–24.

Sholl, D.S., 2019. Five Easy Ways To Make Your Research More Reproducible. Langmuir 35, 13257–13258.

Sing, K.S.W., Everett, D.H., Haul, R.A.W., Moscou, L., Pierotti, R.A., Rouquerol, J., Siemieniewska, T., 1985. Reporting Physisorption Data for Gas/Solid Systems with Special Reference to the Determination of Surface Area and Porosity. Pure and Applied Chemistry 57, 603–619.

Sircar, S., 1999. Gibbsian Surface Excess for Gas Adsorption Revisited. Industrial and Engineering Chemistry Research 38, 3670–3682.

Sircar, S., 2001. Measurement of gibbsian surface excess. AIChE Journal 47, 1169–1176.

Sone, H., Zoback, M.D., 2013. Mechanical properties of shale-gas reservoir rocks - part 1: static and dynamic elastic properties and anisotropy. Geophysics 78, D381–D392.

Song, J., Zhang, D., 2013. Comprehensive review of caprock-sealing mechanisms for geologic carbon sequestration. Environmental Science and Technology 47, 9–22.

Span, R., Wagner, W., 1996. A New Equation of State for Carbon Dioxide Covering the Fluid Region from the TriplePoint Temperature to 1100 K at Pressures up to 800 MPa. Journal of Physical and Chemical Reference Data 25, 1509–1596.

Środoń, J., 1999. Nature of Mixed-layer Clays and Mechanisms of their Formation and Alteration. Annual Review of Earth and Planetary Sciences 27, 19–53.

Środoń, J., 2009. Quantification of illite and smectite and their layer charges in sandstones and shales from shallow burial depth. Clay Minerals 44, 421–434.

Środoń, J., McCarty, D.K., 2008. Surface area and layer charge of smectite from CEC and EGME/$H_2O$-retention measurements. Clays and Clay Minerals 56, 155–174.

Stefanopoulos, K.L., Youngs, T.G.A., Sakurovs, R., Ruppert, L.F., Bahadur, J., Melnichenko, Y.B., 2017. Neutron scattering measurements of carbon dioxide adsorption in pores within the Marcellus Shale: implications for sequestration. Environmental Science and Technology 51, 6515–6521.

Steriotis, T.A., Stefanopoulos, K.L., Kanellopoulos, N.K., Mitropoulos, A.C., Hoser, A., 2004. The structure of adsorbed $CO_2$ in carbon nanopores: a neutron diffraction study. Colloids and Surfaces A: Physicochemical and Engineering Aspects 241, 239–244.

Sudibandriyo, M., Mohammad, S.A., Robinson, R.L., Gasem, K.A.M., 2011. Ono–Kondo Model for High-Pressure Mixed-Gas Adsorption on Activated Carbons and Coals. Energy and Fuels 25, 3355–3367.

Sudibandriyo, M., Mohammad, S.A., Robinson, R.L., Jr., Gasem, K.A., 2010. Ono–Kondo lattice model for high-pressure adsorption: Pure gases. Fluid Phase Equilibria 299, 238–251.

Taylor, J.R., 1997. An Introduction to Error Analysis: The Study of Uncertainties in Physical Measurements. 2nd ed., University Science Books.

Thommes, M., Kaneko, K., Neimark, A.V., Olivier, J.P., Rodriguez-Reinoso, F., Rouquerol, J., Sing, K.S.W., 2015. Physisorption of gases, with special reference to the evaluation of surface area and pore size distribution (IUPAC Technical Report). Pure and Applied Chemistry 87, 1051–1069.

Thompson, C.J., Martin, P.F., Chen, J., Benezeth, P., Schaef, H.T., Rosso, K.M., Felmy, A.R., Loring, J.S., 2014. Automated high-pressure titration system with in situ infrared spectroscopic detection. Review of Scientific Instruments 85, 1–11.

Tournassat, C., Neaman, A., Villiéras, F., Bosbach, D., Charlet, L., 2003. Nanomorphology of montmorillonite particles: Estimation of the clay edge sorption site density by low-pressure gas adsorption and AFM observations. American Mineralogist 88, 1989–1995.

Ustinov, E.A., Do, D.D., Herbst, A., Staudt, R., Harting, P., 2002. Modeling of Gas Adsorption Equilibrium over a Wide Range of Pressure: A Thermodynamic Approach Based on Equation of State. Journal of Colloid and Interface Science 250, 49–62.

Van Olphen, H., Fripiat, J.J., 1979. Data Handbook for Clay Materials and Other Non-metallic Minerals. Pergamon Press.

Viani, A., Gualtieri, A.F., Artioli, G., 2002. The nature of disorder in montmorillonite by simulation of X-ray powder patterns. American Mineralogist 87, 966–975.

Wan, J., Tokunaga, T.K., Ashby, P.D., Kim, Y., Voltolini, M., Gilbert, B., DePaolo, D.J., 2018. Supercritical $CO_2$ uptake by nonswelling phyllosilicates. Proceedings of the National Academy of Sciences 115, 873–878.

Wang, S., Feng, Q., Javadpour, F., Hu, Q., Wu, K., 2019. Competitive adsorption of methane and ethane in montmorillonite nanopores of shale at supercritical conditions: A grand canonical Monte Carlo simulation study. Chemical Engineering Journal 355, 76–90.

Weaver, C.E., 1956. A discussion on the origin of clay minerals in sedimentary rocks. Clays and Clay Minerals 5, 159–173.

Webb, P., Orr, C., 1997. Analytical Methods in Fine Particle Technology. 1st ed., Micromeritics Instrument Corp., Norcross.

Wenning, Q.C., Madonna, C., Kurotori, T., Petrini, C., Hwang, J., Zappone, A., Wiemer, S., Giardini, D., Pini, R., 2021. ChemoMechanical Coupling in Fractured Shale With Water and Hydrocarbon Flow. Geophysical Research Letters 48, 1–12.

Wentinck, H.M., Busch, A., 2017. Modelling of $CO_2$ diffusion and related poro-elastic effects in a smectite-rich cap rock above a reservoir used for $CO_2$ storage. Geological Society, London, Special Publications 454, 155–173.

Wilson, M., Shaldybin, M., Wilson, L., 2016. Clay mineralogy and unconventional hydrocarbon shale reservoirs in the USA. I. Occurrence and interpretation of mixed-layer R3 ordered illite/smectite. Earth-Science Reviews 158, 31–50.

Wilson, M.J., Wilson, L., Patey, I., 2014. The influence of individual clay minerals on formation damage of reservoir sandstones: a critical review with some new insights. Clay Minerals 49, 147–164.

Wollenweber, J., Stanjek, H., Littke, R., Busch, A., Alles, S., Krooss, B.M., 2010. Experimental investigation of the $CO_2$ sealing efficiency of caprocks. International Journal of Greenhouse Gas Control 4, 231–241.

Wong, T.f., David, C., Zhu, W., 1997. The transition from brittle faulting to cataclasic flow in porous sandstones: Mechanical deformation. Journal of Geophysical Research 102, 3009–3025.

Worden, R.H., Morad, S., 2003. Clay minerals in sandstones: controls on formation, distribution and evolution, in: Worden, R.H., Morad, S. (Eds.), Clay Mineral Cements in Sandstones. Blackwell Publishing Ltd., Oxford. volume 34. chapter 1, pp. 3–41.

Xu, W., Johnston, C.T., Parker, P., Agnew, S.F., 2000. Infrared Study of Water Sorption on Na-, Li-, Ca-, and Mg-Exchanged (SWy-1 and SAz-1) Montmorillonite. Clays and Clay Minerals 48, 120–131.

Yuan, B., Wu, X., Chen, Y., Huang, J., Luo, H., Deng, S., 2013. Adsorption of $CO_2$, $CH_4$, and $N_2$ on ordered mesoporous carbon: approach for greenhouse gases capture and biogas upgrading. Environmental Science and Technology 47, 5474–5480.

Zang, A., Wagner, C.F., Dresen, G., 1996. Acoustic emission, microstructure, and damage model of dry and wet sandstone stressed to failure. Journal of Geophysical Research 101, 17507–17521.

Zhang, J., Lu, S., Li, J., Zhang, P., Xue, H., Zhao, X., Xie, L., 2017. Adsorption Properties of Hydrocarbons (n-Decane, Methyl Cyclohexane and Toluene) on Clay Minerals: An Experimental Study. Energies 10, 1–14.

Zhang, T., Ellis, G.S., Ruppel, S.C., Milliken, K.L., Yang, R., 2012. Effect of organic-matter type and thermal maturity on methane adsorption in shale-gas systems. Organic Geochemistry 47, 120–131.

Zhao, H., Wu, T., Firoozabadi, A., 2018. High pressure sorption of various hydrocarbons and carbon dioxide in Kimmeridge Blackstone and isolated kerogen. Fuel 224, 412–423.

Zhong, J., Chen, G., Lv, C., Yang, W., Xu, Y., Yang, S., Xue, L., 2016. Experimental study of the impact on methane adsorption capacity of continental shales with thermal evolution. Journal of Natural Gas Geoscience 1, 165–172.

Ziemiański, P.P., Derkowski, A., Szczurowski, J., Kozieł, M., 2020. The structural versus textural control on the methane sorption capacity of clay minerals. International Journal of Coal Geology 224, 103483.

Zuilhof, H., Yu, S.H., Sholl, D.S., 2018. Writing Theory and Modeling Papers for Langmuir: The Good, the Bad, and the Ugly. Langmuir 34, 1817–1818.

# Appendix A

# Surface area analysis

## A.1 Brunauer-Emmett-Teller theory for surface area calculation

The specific surface area of adsorbent materials are commonly calculated based on the Brunauer-Emmett-Teller (BET) theory that extended the Langmuir model to consider multilayer adsorption (Brunauer et al., 1938). The linearized form of the BET equation is expressed as follows:

$$\frac{P/P^{\mathrm{o}}}{v\big[1-(P/P^{\mathrm{o}})\big]} = \frac{1}{v_{\mathrm{m}}C} + \frac{C-1}{v_{\mathrm{m}}C}\Big(\frac{P}{P^{\mathrm{o}}}\Big) \tag{A.1}$$

where $P$ and $P^{\mathrm{o}}$ are equilibrium and saturation pressures, respectively; $v$ is the amount of adsorbed gas (in $\mathrm{cm}^3$/g STP); $v_{\mathrm{m}}$ is the amount of adsorbed gas to form a monolayer on the adsorbent surface; and $C$ is the BET constant. The values of $v_{\mathrm{m}}$ and $C$ can be obtained from the slope, $s$, and the intercept, $i$, of the linear region (usually $0.05 < P/P^{\mathrm{o}} < 0.35$) when $(P/P^{\mathrm{o}})/\big(v[1-(P/P^{\mathrm{o}})]\big)$ is plotted against $P/P^{\mathrm{o}}$ (RH in the case of water sorption) commonly referred to as the BET plot. The specific surface area, $S_{\mathrm{BET}}$, is then expressed as:

$$S_{\mathrm{BET}} = \frac{v_{\mathrm{m}}N_{\mathrm{A}}\sigma}{v_{\mathrm{m,STP}}} \tag{A.2}$$

where $N_{\mathrm{A}}$ is the Avogadro's number, $\sigma$ is the cross sectional molecular area, and $v_{\mathrm{m,STP}}$ is the adsorbate molar volume at the STP condition (22.4 mol/L). The linear region of the BET plot was determined using the Rouquerol method (Rouquerol et al., 2007), which suggested the following

criteria:

- The intercept of the linear region of the BET plot should be positive, i.e. the BET constant, $C$, should not be negative.
- The term $v(P - P^o)$ should increase monotonically when plotted against $P/P^o$ (commonly referred to as the Rouquerol plot) for the data selected to calculate the BET surface area.
- The value $P/P^o$ that corresponds to the monolayer capacity, $v_m$, should be within the range of $P/P^o$ selected to calculate the BET surface area.
- the value of $P/P^o$ recalculated from $C$ should roughly correspond to the value of $P/P^o$ for the monolayer capacity.

The values of $\sigma$ for $N_2$, Ar, and water are $0.162\,nm^2$, $0.142\,nm^2$ and $0.125\,nm^2$, respectively. Figure A.1 shows the BET and Rouquerol plots for $N_2$, Ar, and water isotherms on the four source clay minerals studied in the thesis, and the BET parameters are summarized in Table A.1.

Table A.1: BET parameters obtained from $N_2$, Ar, and water isotherms

| Probe | Parameter | STx-1b | SWy-2 | ISCz-1 | IMt-2 |
|---|---|---|---|---|---|
| $N_2$ | $v_m$ [$cm^3$/g STP] | 23.2 | 8.44 | 7.49 | 5.03 |
| | $C$ | 183.5 | 474.4 | 132.4 | 222.6 |
| | $P/P^o$ range | 0.05–0.23 | 0.04–0.10 | 0.06–0.25 | 0.06–0.14 |
| | $P/P^o$ at $v_m$ | 0.07 | 0.04 | 0.08 | 0.06 |
| | $R^2$ | 1 | 1 | 1 | 1 |
| Ar | $v_m$ [$cm^3$/g STP] | 21.6 | 8.69 | 7.90 | 5.20 |
| | $C$ | 56.18 | 147.4 | 54.22 | 89.86 |
| | $P/P^o$ range | 0.05–0.20 | 0.06–0.14 | 0.06–0.30 | 0.06–0.18 |
| | $P/P^o$ at $v_m$ | 0.12 | 0.089 | 0.12 | 0.09 |
| | $R^2$ | 1 | 1 | 1 | 1 |
| Water adsorption | $v_m$ [$cm^3$/g STP] | 105.9 | 22.75 | 21.08 | 12.85 |
| | $C$ | 4.13 | 5.86 | 5.52 | 11.0 |
| | $P/P^o$ range | 0.15–0.25 | 0.10–0.22 | 0.10–0.25 | 0.10–0.21 |
| | $P/P^o$ at $v_m$ | 0.36 | 0.27 | 0.28 | 0.23 |
| | $R^2$ | 0.998 | 0.991 | 0.993 | 0.999 |
| Water desorption | $v_m$ [$cm^3$/g STP] | 109.9 | 91.53 | 30.78 | 14.70 |
| | $C$ | 21.6 | 6.24 | 17.0 | 29.5 |
| | $P/P^o$ range | 0.05–0.3 | 0.10–0.3 | 0.10–0.35 | 0.10–0.35 |
| | $P/P^o$ at $v_m$ | 0.18 | 0.29 | 0.20 | 0.16 |
| | $R^2$ | 0.995 | 0.996 | 0.999 | 1 |

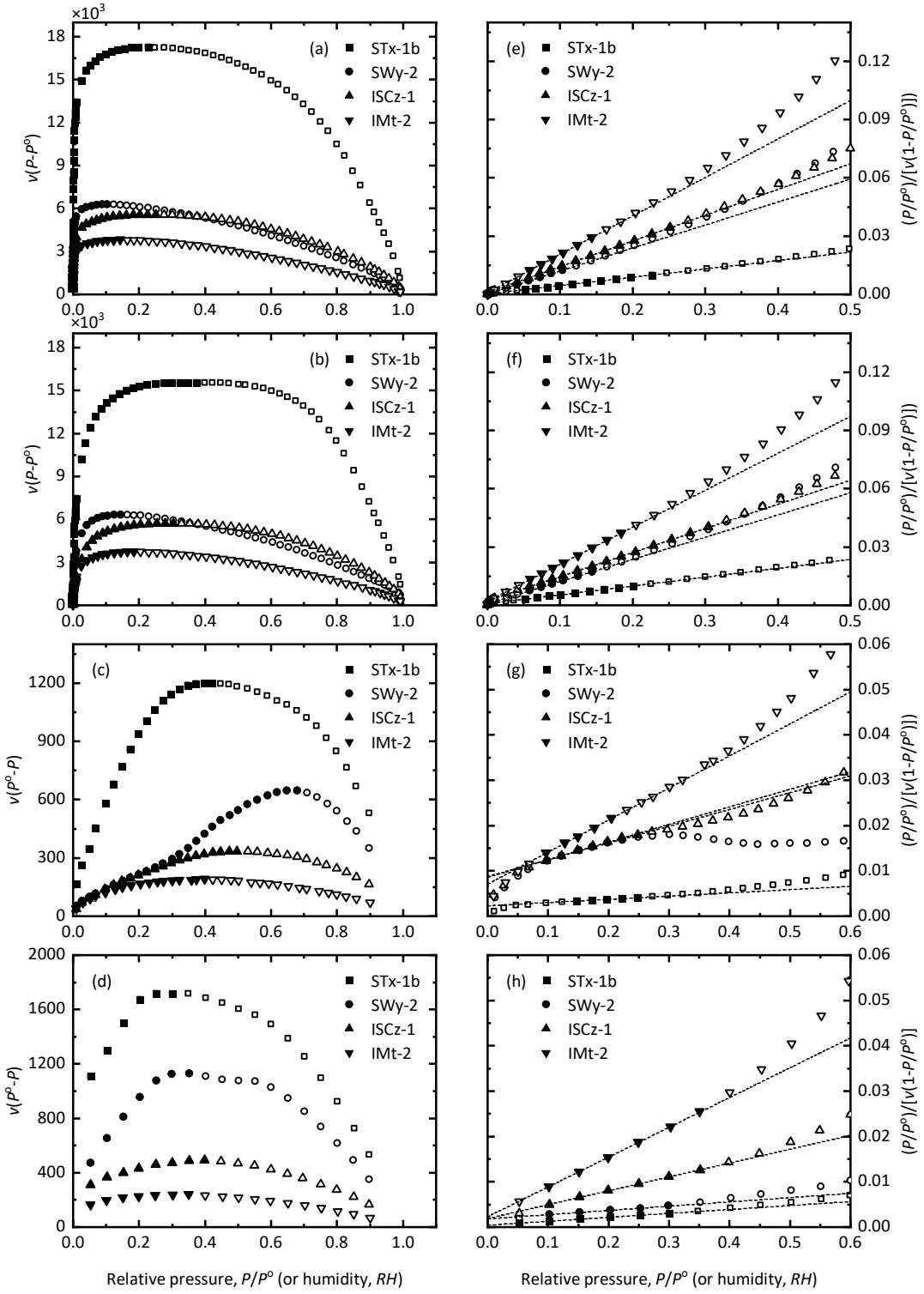



Figure A.1: $v(P^{\circ} - P)$ plotted against $P/P^{\circ}$ for (a) $N_2$, (b) Ar, (c) water adsorption, and (d) water desorption on STx-1b (squares), SWy-2 (circles), ISCz-1 (upward triangles), and IMt-2 (downward triangles). The closed symbols are the data points for which $v(P^{\circ} - P)$ increases monotonically as a function of $P/P^{\circ}$. The linearized form of the BET equation is plotted for (e) $N_2$, (f) Ar, (g) water adsorption, and (h) water desorption on the four clay minerals where the points within the linear range (closed symbols) are used to estimate $S_{\mathrm{BET}}$. The dashed lines are linear regression fits.

# Appendix B

# Error analysis

## B.1 Error propagation

The values of uncertainty associated with the quantities calculated from any experimental measurements reported in this study have been estimated using the general formula for error propagation (Taylor, 1997):

$$\delta q = \sqrt{\left(\frac{\partial q}{\partial x}\delta x\right)^2 + \cdots + \left(\frac{\partial q}{\partial z}\delta z\right)^2} \tag{B.1}$$

where $\delta q$ is the uncertainty of the function $q(x, \ldots, z)$ with multiple variables. The following section demonstrates the application of Equation B.1 by showing the steps taken to calculate the uncertainty value of the specific molar amount of excess adsorption as an example.

According to Equation 3.4, the specific molar amount of excess adsorption, $n_{\mathrm{ex}}$, is expressed as follows:

$$n^{\mathrm{ex}}(\rho, T) = \frac{\mathrm{MP}_1(\rho, T) - \mathrm{MP}_{1,0} + \rho_{\mathrm{b}} V_0}{M m_{\mathrm{s}}} \tag{B.2}$$

Assuming the uncertainty of the adsorbate molar mass, $M$, is negligible, the uncertainty associated with the measured excess adsorbed amount can be estimated from the following equation:

$$\begin{aligned}\delta n_{\mathrm{ex}} = \sqrt{\left[\left(\frac{1}{M m_{\mathrm{s}}}\right)\delta \mathrm{MP}_1(\rho, T)\right]^2 + \left[\left(-\frac{1}{M m_{\mathrm{s}}}\right)\delta \mathrm{MP}_{1,0}\right]^2 + \left[\left(\frac{V_0}{M m_{\mathrm{s}}}\right)\delta \rho_{\mathrm{b}}\right]^2} \\ + \left[\left(\frac{\rho_{\mathrm{b}}}{M m_{\mathrm{s}}}\right)\delta V_0\right]^2 + \left[\left(-\frac{\mathrm{MP}_1(\rho, T) - \mathrm{MP}_{1,0} + \rho_{\mathrm{b}} V_0}{M m_{\mathrm{s}}^2}\right)\delta m_{\mathrm{s}}\right]^2\end{aligned} \tag{B.3}$$

The uncertainty values of $\mathrm{MP}_1(\rho, T)$ and $\mathrm{MP}_{1,0}$ are assumed to be nearly equal; therefore,

$\delta\mathrm{MP}_1(\rho, T)$ and $\delta\mathrm{MP}_{1,0}$ are defined collectively as $\delta\mathrm{MP}_1$. Rearranging Equation B.3 yields,

$$\delta n_{\mathrm{ex}} = \sqrt{\frac{2\delta{\mathrm{MP}_1}^2 + V_0^2\delta\rho_{\mathrm{b}}^2 + \rho_{\mathrm{b}}^2\delta V_0^2 + n_{\mathrm{ex}}^2 M^2 \delta m_{\mathrm{s}}^2}{(M m_{\mathrm{s}})^2}} \tag{B.4}$$

The value of $\mathrm{MP}_1(\rho, T)$ is obtained as an average of the measured values of $\mathrm{MP}_1(\rho, T)$ after the adsorption system has reached equilibrium. Therefore, the standard deviation of this average is taken as $\delta\mathrm{MP}_1$ (approximately between $1 \times 10^{-5}$ g and $2 \times 10^{-4}$ g). Equation B.1 is again used to calculate the value of $\delta\rho_{\mathrm{b}}$ and $\delta m_{\mathrm{sk}}$:

$$\delta\rho_{\mathrm{b}} = \sqrt{2\delta m_{\mathrm{sk}}^2\left(\frac{1}{V_{\mathrm{sk}}}\right)^2 + \delta V_{\mathrm{sk}}^2\left(\frac{m_{\mathrm{sk},0} - m_{\mathrm{sk}}}{V_{\mathrm{sk}}^2}\right)^2} \tag{B.5}$$

$$\delta m_{\mathrm{sk}} = \sqrt{\delta{\mathrm{MP}_2}^2 + \delta{\mathrm{MP}_1}^2} \tag{B.6}$$

The value of $\delta V_0$ is estimated by calculating the value of uncertainty involved in the method of weighted linear regression applied to the helium gravimetry experiments (see Section B.2). The value of $\delta m_{\mathrm{s}}$ can be estimated from the uncertainty of the intercept obtained from the weighted linear fit; however, a more conservative estimate provided by the supplier was taken ($\delta m_{\mathrm{s}} = 0.001\,\mathrm{g}$). The value of $\delta V_{\mathrm{sk}}$ was also provided by the supplier ($\delta V_{\mathrm{sk}} = 0.002\,\mathrm{cm}^3$).

## B.2 Error from linear regression

In this thesis, two methods of linear regression were used to estimate the values of the intercept $A$ and the slope $B$ that describe linear regions found in the experimental data as well as the uncertainty values thereof: simple linear regression and weighted linear regression. The method of simple linear regression was used to calculate the values and uncertainty of $A$ and $B$ of the linear region exhibited by the experimental data for which the level of uncertainty in the measurements is not known explicitly (e.g. the BET plot). In contrast, the method of weighted linear regression was applied to the measurements each with a known value of uncertainty (e.g. helium gravimetry experiment) to give different weights to each measurements to obtain a linear fit.

### B.2.1 Simple linear regression

The method of simple linear regression uses the *normal equations* to find the least-squares estimates of $A$ and $B$ that describe the linear relationship between $x$ and $y$ (Taylor, 1997):

$$A = \frac{\sum x^2 \sum y - \sum x \sum xy}{\Delta} \tag{B.7}$$

$$B = \frac{N \sum xy - \sum x \sum y}{\Delta} \tag{B.8}$$

where $N$ is the number of measurements used to estimate the values of $A$ and $B$, and the denominator $\Delta$ is given by the following equation:

$$\Delta = N \sum x^2 - \left( \sum x \right)^2 \tag{B.9}$$

The uncertainty in the measurements $y$ was estimated using the following equation:

$$\delta y = \sqrt{\frac{1}{N-2} \sum_{i=1}^{N} (y_i - A - Bx_i)^2} \tag{B.10}$$

The uncertainty of $A$ and $B$ can then be estimated using the following equation:

$$\delta A = \delta y \sqrt{\frac{\sum x^2}{\Delta}} \tag{B.11}$$

$$\delta B = \delta y \sqrt{\frac{N}{\Delta}} \tag{B.12}$$

where $\Delta$ is again given by Equation B.9. In this thesis, the simple linear regression method was used to estimate the uncertainty values of the slope and the intercept of the linear relationship between $(P/P^{\circ})/[v(1 - P/P^{\circ})]$ and $P/P^{\circ}$ in the BET plot (see Appendix A). Consequently, the uncertainty value of the surface area calculated from the slope and the intercept of the linear region of the BET plot was estimated using the formula of error propagation (Equation B.1).

### B.2.2 Weighted linear regression

With known values of uncertainties associated with each data point $\delta i$ and the weight of each measurement $w_i = 1/\delta i^2$, the values of $A$ and $B$ of a straight line that describes the linear relationship

between $x$ and $y$ can be found from the following equations (Taylor, 1997):

$$A = \frac{\sum wx^2 \sum wy - \sum wx \sum wxy}{\Delta} \tag{B.13}$$

$$B = \frac{\sum w \sum wxy - \sum wx \sum wy}{\Delta} \tag{B.14}$$

where $\Delta$ is defined as:

$$\Delta = \sum w \sum wx^2 - \left( \sum wx \right)^2 \tag{B.15}$$

The uncertainty of $A$ and $B$ can then be calculated as:

$$\delta A = \sqrt{\frac{\sum wx^2}{\Delta}} \tag{B.16}$$

$$\delta B = \sqrt{\frac{\sum w}{\Delta}} \tag{B.17}$$

The method of weighted linear regression was used to estimate the uncertainty values of $V_0$, $V_{\mathrm{met}}$, and $m_{\mathrm{s}}$, all of which are quantities required to calculate the amount of excess or net adsorption and the uncertainty values thereof.

# Appendix C

# Pore discretization

## C.1 Pore-size distribution

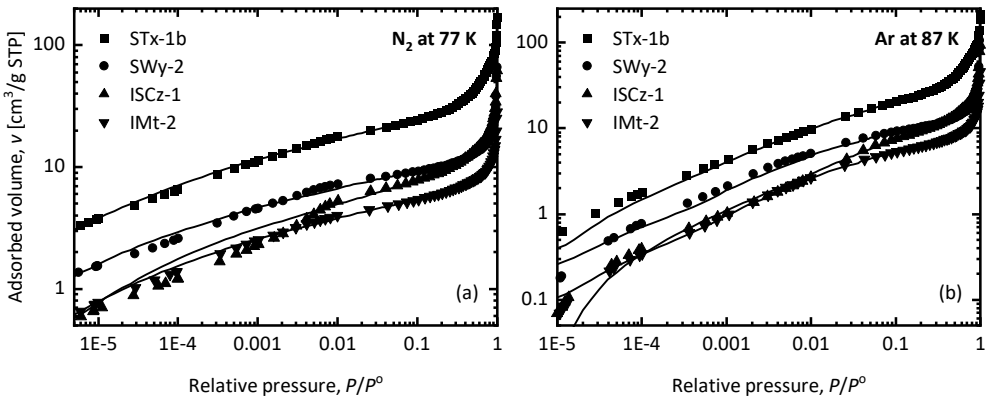



Figure C.1: (a) $N_2$ and (b) Ar adsorption isotherms (symbols) with NLDFT fits (solid lines) for four source clay minerals in this thesis.

The pore-size distributions of the four source clay minerals studied in this thesis were obtained from $N_2$ and Ar adsorption isotherms using the non-local density functional theory (NLDFT) on zeolite cylindrical model and from $CO_2$ adsorption isotherms using the grand canonical Monte Carlo (GCMC) on carbon model. Both the NLDFT and GCMC models were available on Quantachrome Instrument's proprietary software used for data logging and analysis. Although clay minerals are mostly characterized by their slit-shaped pores, the cylindrical model of the NLDFT was chosen due to the lowest fitting error (0.41 % to 0.77 % for $N_2$ and 0.41 % to 0.65 % for Ar) compared to other available slit models. The comparisons between the NLDFT fits and experimental $N_2$ and Ar

isotherms are shown in Figure C.1. Figure C.2 shows the pore-size distributions obtained from the

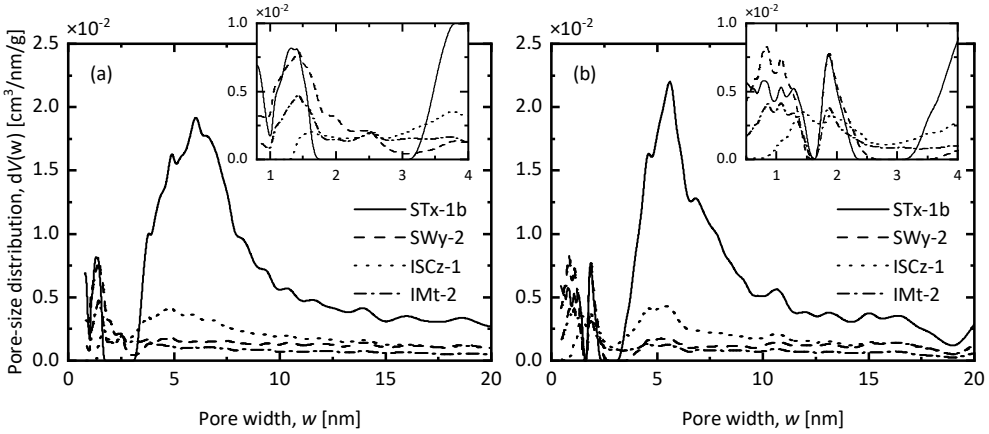



Figure C.2: Pore-size distributions of the four source clay minerals studied in this thesis up to 20 nm obtained from (a) $N_2$ and (b) Ar adsorption isotherms. The inset plots show the same distribution curves below 4 nm.

$N_2$ and Ar adsorption isotherms using the NLDFT model. The pore-size distributions obtained from the Ar isotherms were combined with those obtained from the $CO_2$ adsorption isotherms using the GCMC model (fitting comparison is shown in Figure C.3, fitting error of 1.07 % to 3.81 %), representing comprehensive distributions of micro-, meso-, and macropores.

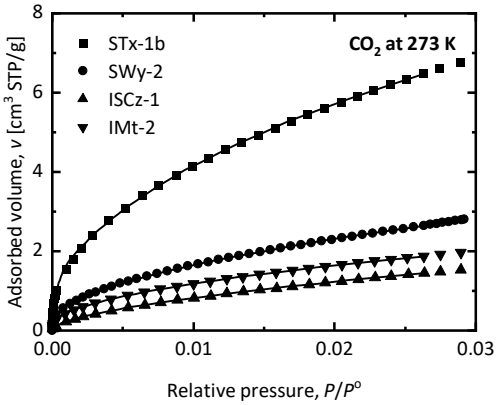



Figure C.3: $CO_2$ adsorption isotherms (symbols) with GCMC fits (solid lines) of the four source clay minerals in this thesis.

## C.2 Lattice pore discretization

The combined pore-size distributions were discretized into a finite number of lattice pores as shown in Figure C.4. First, the mesopores larger than 20 nm (not shown in Figure C.2 and C.4) showed

little impact on the isotherm shape or the total adsorbed amount; therefore, these mesopores ($\geq$20 nm) were grouped into a single lattice pore, which accounted for approximately 50 % to 70 % of the total pore volume. The pores smaller than 20 nm were then grouped in 5 nm increments (e.g. pore that are between the size of 5 nm to 10 nm were grouped into a single lattice pore that represents small mesopores). The pore volumes of each lattice pore were determined as the sum of the pore volumes corresponding to every pore widths within the discretized lattice pore group. The number of lattice layers was then determined to be rounded value of the average lattice pore width divided by the molecule diamter ($\sigma_{CO_2} \approx \sigma_{CH_4} \approx 4$ Å).

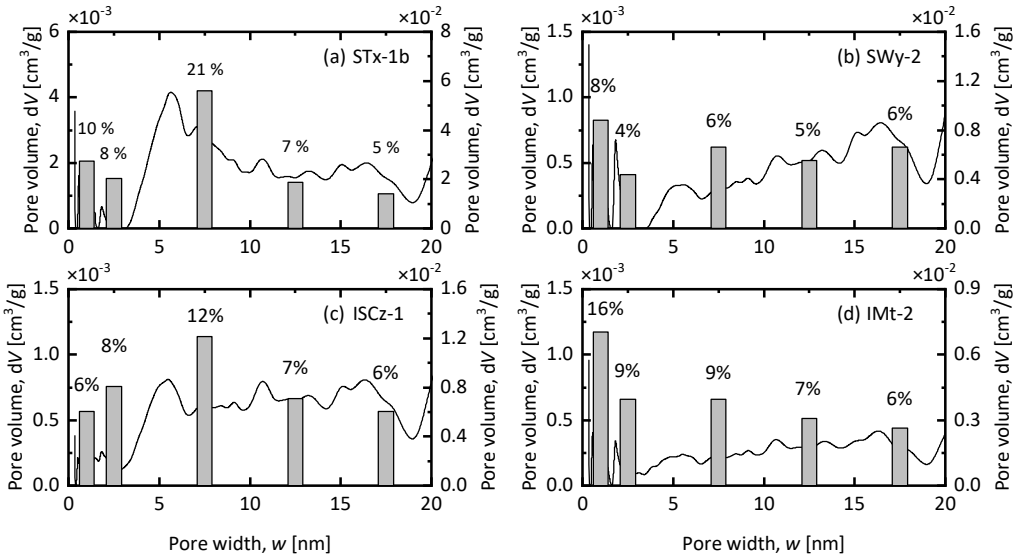



Figure C.4: Pore volume distributions (solid lines, left $y$-axis) obtained from the Ar and $CO_2$ adsorption isotherms shown up to 20 nm. The volumes of the discretized pores (in 5 nm increments) are shown in bars (right $y$-axis) and their respective volume percentages are labeled. The number of layers for the chosen lattice pores are as follows: 3 (1.2 nm), 4 (1.6 nm), 6 (2.4 nm), 19 (7.6 nm), 31 (12.4 nm), 44 (17.6 nm), and 60 (24 nm).